

Acoustofluidics
2023

Table of Contents

Welcome Letter	3
General Information	4
Conference Officials	5
Acoustofluidics Society	6
Benefactors	7
Keynote Speakers	8
Invited Speakers	8
Program Schedule	9

Welcome Letter

WELCOME BY THE CONFERENCE CHAIRS

It is with great pleasure that we welcome you to the annual Acoustofluidics conference 2023. After a late change in venue, we are excited to host the conference in St. Louis. This marks only the second time in its history that Acoustofluidics will be held outside of Europe. We recognize that international travel remains challenging and appreciate those who are able to attend in person, while also offering a hybrid participation option for those who cannot.

Abstract submissions were of a typically high standard, enabling assembly of a strong slate of talks spanning advancements in device physics, new phenomena, and applications. There is a particular emphasis on biological and biomedical applications, evidencing the ever-increasing impact of acoustofluidic approaches in these areas. The broad coverage of the contributed talks is also reflected in the series of excellent keynote and invited speakers, which point to connections of acoustofluidics to emerging research in functional materials, tissue biomechanics, and novel therapeutics. Furthermore, the program includes multiple talks describing the translation of acoustofluidic technologies from the research lab to the clinic, representing the maturation of the field.

In addition to numerous opportunities for networking, this year we are increasing engagement with our thriving young researcher community by holding a career-development panel comprising industry and academic representatives. We will once again highlight the winner of the previous year's W. Terence Coakley Award, which distinguishes a promising student or postdoctoral researcher in acoustofluidics, with an invited talk on the first day of the conference. This year's award will be sponsored by Frontiers in Acoustics as part of the launch of a new journal that includes a dedicated Acoustofluidics Section. Additionally, the Royal Society of Chemistry will sponsor an award for Best Research Image in Acoustofluidics. The image will be featured on the cover of an upcoming issue of the Royal Society's prestigious journal *Lab on a Chip*.

We would like to acknowledge the support and feedback provided by members of the Acoustofluidics Society and community, which allow us to maintain the Acoustofluidics conference as an essential venue for dissemination of important results in the field. We greatly appreciate the work of the Scientific Committee to evaluate submitted abstracts under an abnormally compressed timeline. This conference also would not have been possible without the incredible efforts of the event planning team from the Washington University's McKelvey School of Engineering, alongside the invaluable contribution of PMMI Global. Finally, we are grateful for the support of our long-standing sponsors the Acoustofluidics Society and CBMS, the Chemical and Biological Microsystems Society.

We are fortunate to host Acoustofluidics 2023 in the McKelvey School of Engineering, part of the recently completed East End Transformation of Washington University's Danforth Campus. It will be great to see you all again in person and share a truly exciting, stimulating, and productive conference on the 16th – 18th August 2023.

J. Mark Meacham
Washington University in St. Louis, USA
Chair Acoustofluidics 2023



Glauber T. Silva
Universidade Federal de Alagoas, BRAZIL
Chair Acoustofluidics 2023



General Information

Wireless Internet Service

Wireless Internet will be available in the meeting space. A password is not needed.

- Staff or Students of the University may use: **Eduroam**
- All others should select: **wustl-guest**

Additional information may be found on the [website](#).

Chimes

The chimes will ring five minutes before the end of each scheduled break. The sessions will begin on time, so please return to the sessions when you hear the chimes.

Cellular Phones and Alarms

As a courtesy to our speakers and other attendees, please turn off any cellular phones and alarms during sessions.

Video Recording

Video recordings are strictly prohibited in the sessions and poster presentations.

WHERE CAN I GO FROM HERE? Panel For Junior Researchers

Wednesday, 16 August

15:40 - 17:00

Join us for a discussion of academic, research, and industrial opportunities for junior researchers in acoustofluidics and related disciplines.

Banquet

Thursday, 17 August

18:30 - 20:30

Holmes Lounge

No conference is complete without a banquet. Join us on Thursday evening at the Holmes Lounge for a delicious meal and a chance to network with colleagues. The Holmes Lounge is a brief walk across campus.



Conference Officials

Conference Chairs

J. Mark Meacham Washington University, St. Louis, USA
Glauber T. Silva Universidade Federal de Alagoas, BRAZIL

Advisory Committee

Per Augustsson Lund University, SWEDEN
Rune Barnkob Technische Universität München, GERMANY
Bruce Drinkwater University of Bristol, UK
Xuexin Duan Tianjin University, CHINA
Thomas Franke University of Glasgow, SCOTLAND
Richard Fu Northumbria University, UK
Peter Glynne-Jones University of Southampton, UK
J. Mark Meacham Washington University, St. Louis, USA
Tim Segers University of Twente, NETHERLANDS
Ashis Kumar Sen Indian Institute of Technology, Madras, INDIA
Glauber T. Silva Universidade Federal de Alagoas, BRAZIL
Maria Tenje Uppsala University, SWEDEN

Scientific Committee

Per Augustsson Lund University, SWEDEN
Rune Barnkob Technische Universität München, GERMANY
Michaël Baudoin Université de Lille, France
Philippe Brunet Université Paris Diderot, FRANCE
Henrik Bruus Technical University of Denmark, DENMARK
Feiyan Cai Shenzhen Institute of Advanced Technology, CHINA
Bruce Drinkwater University of Bristol, UK
Jürg Dual ETH Zürich, SWITZERLAND
Xuexin Duan Tianjin University, CHINA
Mohamed El Malki Mohammed First University, MOROCCO
James Friend University of California, San Diego, USA
Glynne-Jones University of Southampton, UK
Xiasheng Guo Nanjing University, CHINA
Thomas Laurell Lund University, SWEDEN
Andreas Lenshof Lund University, SWEDEN
Kian-Meng Lim National University of Singapore, SINGAPORE
Philippe Marmottant Université Grenoble Alps, FRANCE
J. Mark Meacham Washington University, St. Louis, USA
Adrian Neild Monash University, AUSTRALIA
Hagen Schmidt IFW Dresden, GERMANY
Ashis Kumar Sen Indian Institute of Technology, Madras, INDIA
Glauber T. Silva Universidade Federal de Alagoas, BRAZIL
Karthick Subramani Indian Institute of Information Technology, Design and
..... Manufacturing Kancheepuram, INDIA
Maria Tenje Uppsala University, SWEDEN
Michel Versluis University of Twente, NETHERLANDS
Martin Wiklund KTH Stockholm, SWEDEN

Acoustofluidics Society

The Acoustofluidics Society is an international body that represents and facilitates the interests of researchers and industries in the fields of acoustic particle manipulation, acoustic fluid control, and associated technologies, with particular applications in the Life sciences.



Executive Committee

Peter Glynne-Jones, University of Southampton, UK President
Per Augustsson, Lund University, SWEDEN Vice-President
Maria Tenje, Uppsala University, SWEDEN Secretary
James Friend, University of California, San Diego, USA Treasurer

Board Members

J. Mark Meacham Washington University, St. Louis, USA
Glauber T. Silva Universidade Federal de Alagoas, BRAZIL
Richard Fu Northumbria University, UK
Xuexin Duan Tianjin University, CHINA
Rune Barnkob Technische Universität München, GERMANY
Maria Tenje Uppsala University, SWEDEN
Ashis Kumar Sen Indian Institute of Technology, Madras, INDIA
Tim Segers University of Twente, NETHERLANDS

Benefactors

Conference Sponsor

[Chemical and Biological Microsystems Society \(CBMS\)](#)



[Acoustofluidics Society](#)



W. Terence Coakley Poster Award Sponsors

[Acoustofluidics Society](#)



[Frontiers](#)



Best Acoustofluidics Research Image Award Sponsor

[Royal Society of Chemistry](#)



LabonaChip

Media Benefactor

[Microtech Ventures](#)



Keynote Speakers



ACOUSTIC PATTERNING AND PRINTING OF FUNCTIONAL MATERIALS

[Matt Begley](#)

University of California, Santa Barbara, USA



SIMULATING BUBBLES AND THEIR ROLE IN SHOCKWAVE AND ULTRASOUND THERAPIES

[Tim Colonius](#)

California Institute of Technology, USA



ULTRASONIC ELASTICITY IMAGING WITH ACOUSTIC RADIATION FORCE

[Kathy Nightingale](#)

Duke University, USA

Invited Speakers



RAPID IN-FLOW MEASUREMENT OF WHOLE CHANNEL ACOUSTIC ENERGY, QUALITY FACTOR, AND CELL PROPERTIES

[Thierry Baasch](#)

Lund University, SWEDEN



ULTRASOUND WITH MICROBUBBLE-MEDIATED AGENT TRANSPORT IN AND OUT OF THE BRAIN

[Hong Chen](#)

Washington University in St. Louis, USA



ACOUSTOFLUIDICS – FROM RESEARCH TOWARDS HEALTHCARE

[Mikael Evander](#)

AcouSort AB, SWEDEN

Wednesday 16 August

All Times are Central Daylight Time (CDT).

- 08:50 Welcome and Opening Remarks**
J. Mark Meacham, *Washington University in St. Louis, USA*
Glauber T. Silva, *Universidade Federal de Alagoas, BRAZIL*

Session 1 - Devices 1

Session Chair: Glauber T. Silva, *Universidade Federal de Alagoas, BRAZIL*

Keynote Speaker 1

- 09:00 ACOUSTIC PATTERNING AND PRINTING OF FUNCTIONAL MATERIALS**
Matt Begley
University of California, Santa Barbara, USA

Contributed Talks

- 09:50 HIGH-POWER BULK WAVE ACOUSTOFLUIDICS**
Enrico Corato¹, Ola Jakobsson¹, Wei Qiu¹, Takeshi Morita², and Per Augustsson¹
¹*Lund University, SWEDEN* and ²*University of Tokyo, JAPAN*
- 10:05 ACOUSTIC MANIPULATION OF PARTICLES IN MICROFLUIDIC CHIPS WITH AN ADAPTIVE CONTROLLER THAT MODELS ACOUSTIC FIELDS**
Kyriacos Yiannacou and Veikko Sariola
Tampere University, FINLAND
- 10:20 FULLY MICROFABRICATED SURFACE ACOUSTIC WAVE TWEEZER FOR (SUB-) MICRON PARTICLE FOCUSING**
Armaghan Fakhfour¹, Melanie Colditz¹, Citsabehsan Devendran², Stefan Jacob³, Kateryna Ivanova¹, Adrian Neild², and Andreas Winkler¹
¹*Leibniz IFW Dresden, GERMANY*, ²*Monash University, AUSTRALIA*, and ³*Physikalisch-Technische Bundesanstalt, GERMANY*
- 10:35 Coffee Break**

Session 2 - Biological and Biomedical Applications 1

Session Chair: Yuan Gao, *University of Memphis, USA*

Invited Speaker 1

11:00 ACOUSTOFLUIDICS – FROM RESEARCH TOWARDS HEALTHCARE

Mikael Evander

AcouSort AB, SWEDEN

Contributed Talks

11:30 ACOUSTIC STREAMING-DRIVEN ADVECTION ENHANCEMENT OF ELISA SPEED AND SENSITIVITY

Lei Zhang¹, Shuai Zhang¹, Cecile Floer², and James Friend¹

¹*University of California, San Diego, USA and*

²*Universite de Lorraine-CNRS, FRANCE*

11:45 INTEGRATION OF A SILICON CHAMBER IN HYBRID ACOUSTIC WAVE DEVICES FOR PRECISE CELL PATTERNING AND CILIARY WAVEFORM ANALYSIS

Mingyang Cui^{1,2}, Li Shan³, and J. Mark Meacham¹

¹*Washington University, St. Louis, USA,* ²*Massachusetts Institute of Technology, USA, and* ³*University of Texas, Dallas, USA*

12:00 RAMAN-ACOUSTOFLUIDICS SPECTROSCOPY FOR RED BLOOD CELL ANALYSIS

Ueslen Rocha and Glauber Tomaz da Silva

Federal University of Alagoas, BRAZIL

12:15 Lunch

Session 3 - Physics: New Phenomena

Session Chair: Alen Pavlič, *Caltech, USA*

Invited Speaker 2

13:45 RAPID IN-FLOW MEASUREMENT OF WHOLE CHANNEL ACOUSTIC ENERGY, QUALITY FACTOR, AND CELL PROPERTIES

Thierry Baasch

Lund University, SWEDEN

Contributed Talks

14:15 TRANSIENT BEHAVIOR AND ACOUSTIC STREAMING EFFECTS IN ACOUSTICALLY PACKED BLOOD

Richard Soller, Ola Jakobsson, Wei Qiu, and Per Augustsson

Lund University, SWEDEN

14:30 ACOUSTOFLUIDIC SHAPE-BASED SEPARATION OF MICROPARTICLES AND CELLS BY ACOUSTIC RADIATION FORCE AND TORQUE

Muhammad S. Khan, Mushtaq Ali, and Jinsoo Park
Chonnam National University, KOREA

14:45 ULTRASONIC SINGLE-BEAM MANIPULATION OF PARTICLES AND ORGANIDS THROUGH A PETRI-DISH AND A PLASTIC TUBE USING AN ACOUSTIC FIELD LIVE-VISUALISATION METHOD

Mario Ortega Sandoval, Krishna Coimbatore Balram, Luke Cox, Martha Lavelle, James Armstrong, and Bruce Drinkwater
University of Bristol, UK

15:00 ELECTROMECHANICAL RESONANCE IN ELECTRICAL DOUBLE LAYERS DRIVEN BY MHZ-FREQUENCY SURFACE ACOUSTIC WAVE

Sudeepthi Aremanda and Ofer Manor
Technion-Israel Institute of Technology, ISRAEL

15:15 Coffee Break

PANEL FOR JUNIOR RESEARCHERS

Moderators: Alen Pavlić, *Caltech, USA* (in-person) and
Dhananjay V. Deshmukh, *ETH Zürich, SWITZERLAND* (remote)

15:40 WHERE CAN I GO FROM HERE?

Mikael Evander, *AcouSort AB, SWEDEN*
James Friend, *University of California, San Diego*
Thomas Laurell, *Lund University, SWEDEN*
Maria Tenje, *Uppsala University, SWEDEN*

17:00 Transition

Reception

17:05 - 18:30 Join us for an informal reception in the Jubel Hall Gallery.

Thursday, 17 August

All Times are Central Daylight Time (CDT).

08:50 Announcements

Session 4 - Biological and Biomedical Applications 2

Session Chair: Maria Tenje, *Uppsala University, SWEDEN*

Keynote Speaker 2

09:00 **ULTRASONIC ELASTICITY IMAGING WITH ACOUSTIC RADIATION FORCE**

Kathryn Nightingale
Duke University, USA

Contributed Talks

09:50 **ACOUSTOPHORESIS ENRICHES TUMOR CELL CLUSTERS IN BLOOD OF PATIENTS WITH PROSTATE CANCER**

Cecilia Magnusson¹, Per Augustsson¹, Eva Undvall Anand¹, Andreas Lenshof¹, Andreas Josefsson^{2,3}, Karin Welén², Anders Bjartell¹, Yvonne Ceder¹, Hans Lilja^{1,4}, and Thomas Laurell¹
¹*Lund University, SWEDEN*, ²*Göteborg University, SWEDEN*, ³*Umeå University, SWEDEN*, and ⁴*Memorial Sloan-Kettering Cancer Center, USA*

10:05 **POROS GIGA: ACOUSTOFLUIDIC PLATFORM FOR CLINICAL-SCALE CELL ENGINEERING**

Mugdha Sinha^{1,2}, Mohammad Albuhsin^{1,2}, Jahir Islam¹, J. Mark Meacham^{1,2}, and Michael M. Binkley¹
¹*OpenCell Technologies, Inc., USA* and
²*Washington University, Saint Louis, USA*

10:20 **IMPROVING MICROTISSUE HISTOLOGY USING ACOUSTOFLUIDICS**

Dhananjay V. Deshmukh¹, Emilie Vuille-dit-Bille², Nicola Gerber¹, Christine Fux¹, Annina Eichenberger¹, Sarah Heub², Gilles Weder², Jurg Dual¹, and Mark W. Tibbitt¹
¹*ETH Zürich, SWITZERLAND*, ²*CSEM SA, and SWITZERLAND*

10:35 Coffee Break

Session 5 - Physics: Acoustic Fields and Streaming

Session Chair: Zhenhua Tian, *Virginia Polytechnic Institute and State University, USA*

Contributed Talks

- 11:00 DROPLET UPON A SUPERHYDROPHOBIC SURFACE FOR STUDYING FLUID INTERACTIONS WITH ACOUSTIC WAVES**
Kha Nguyen¹, Jeremy Orosco¹, Shuai Zhang¹, Antoine Pallois²,
Stefan Llewellyn Smith¹, and James Friend¹
¹*University of California, San Diego, USA* and ²*Ecole Polytechnique, FRANCE*
- 11:15 MICROSTREAMING INDUCED BY THE COMPLEX MOTION OF A MICRO-PILLAR**
Jules Ghesquiere, Michaël Baudoin, Olivier Bou Matar, and Sarah Cleve
Université de Lille, FRANCE
- 11:30 ABOUT ALTERING EQUILIBRIUM POSITIONS OF PARTICLES TRAPPED IN AN ACOUSTIC TWEezer BASED ON A 2DSSAW**
Jörg König¹, Zhichao Deng¹, Sebastian Sachs¹, Hagen Schmidt²,
and Christian Cierpka^{1,3}
¹*TU Ilmenau, GERMANY*, ²*IFW Dresden, GERMANY*, and
³*Lund University, SWEDEN*
- 11:45 ACOUSTIC STREAMING IN THE FLUID OF THE INNER EAR**
Charles Thompson, Kavitha Chandra, and Adian Keefe
University of Massachusetts, USA
- 12:00 UNIVERSAL INTERDIGITAL TRANSDUCER (IDT) FOR STABLE MULTI-PATTERNS AGGREGATION OF MICROPARTICLES IN A DROPLET**
Etien Martinez Roman, Bjørn M. Qvenild-Svenningsen,
and Diego Sanchez Saldaña
Norwegian University of Science and Technology (NTNU), NORWAY
- 12:15 Lunch**

Session 6 - Physics: Theory and Simulation

Session Chair: Nitesh Nama, *University of Nebraska, Lincoln, USA*

Keynote Speaker 3

- 13:30 SIMULATING BUBBLES AND THEIR ROLE IN SHOCKWAVE AND ULTRASOUND THERAPIES**
Tim Colonius
California Institute of Technology, USA

Contributed Talks

- 14:20** **THEORY AND NUMERICAL STUDIES OF SHALLOW TRAVELLING-WAVE MICROPUMPS**
Søren A.S. Kuhberg and Henrik Bruus
Technical University of Denmark, DENMARK
- 14:35** **IMPACT OF ACOUSTIC SCATTERER ELASTICITY AND FREQUENCY ON ACOUSTOPHORESIS IN A STANDING WAVE FIELD**
Khemraj Gautam Kshetri, and Nitesh Nama
University of Nebraska, Lincoln, USA
- 14:50** **ACOUSTOKES: FRAMEWORK FOR MULTIBODY ACOUSTOPHORESIS SIMULATIONS INCLUDING ACOUSTICS, HYDRODYNAMICS AND CONTACTS**
Alen Pavlič^{1,2}, Wei Qiu³, Jürg Dual¹, and Thierry Baasch³
¹ETH Zürich, SWITZERLAND, ²Caltech, USA, and ³Lund University, SWEDEN
- 15:05** **Coffee Break**

Session 7 - Devices 2

Session Chair: Mingyang Cui, *Massachusetts Institute of Technology, USA*

Contributed Talks

- 15:30** **DESIGN OF BIMORPH TRANSDUCER FOR HIGH-THROUGHPUT GENE EDITING**
Mohammad M. Albuhsin^{1,2}, Mugdha Sinha^{1,2}, Jahir Islam², J. Mark Meacham¹, and Michael M. Binkley¹
¹OpenCell Technologies, Inc., USA and ²Washington University, Saint Louis, USA
- 15:45** **MICROSCALE CHARACTERIZATION OF A VERSATILE ULTRASONIC DROPLET GENERATOR**
Hongyu Bai¹, Li Shan^{1,2}, and J. Mark Meacham¹
¹Washington University, St. Louis, USA and ²University of Texas, Dallas, USA
- 16:00** **INTEGRATED TRANSPARENT SURFACE ACOUSTIC WAVE TECHNOLOGY FOR ACTIVE DE-FOGGING AND ICING PROTECTION ON GLASS**
Hui Ling Ong, Luke Haworth, Jikai Zhang, Prashant Agrawal, Hamdi Torun, Qiang Wu, and Yong-Qing Fu
Northumbria University, UK
- 16:15** **DYNAMIC DROPLET IMPACT UNDER ACOUSTIC WAVES: SURFACE INCLINATION, HYDROPHOBIC COATINGS AND NON-NEWTONIAN LIQUIDS**
Luke Haworth¹, Mehdi Biroun², Prashant Agrawal¹, Hamdi Torun¹, Glen McHale³, and Richard Fu¹
¹Northumbria University, UK, ²University College London, UK, and ³University of Edinburgh, UK

W. Terence Coakley Poster Session
Holmes Lounge

17:00 – 18:30

- P01 STRUCTURAL REORGANIZATION OF ACTIN FILAMENTS IN A CIRCULAR FLOW USING SURFACE ACOUSTIC WAVES**
Donyoung Kang, Minseo Kim, and Hyungsuk Lee
Yonsei University, KOREA
- P02 MICROSCALE CHARACTERIZATION OF A VERSATILE ULTRASONIC DROPLET GENERATOR**
Hongyu Bai¹, Li Shan^{1,2}, and J. Mark Meacham¹
¹*Washington University, St. Louis, USA* and ²*University of Texas, Dallas, USA*
(Presented in Session 7 - Devices 2)
- P03 HIGH-POWER BULK WAVE ACOUSTOFLUIDICS**
Enrico Corato¹, Ola Jakobsson¹, Wei Qiu¹, Takeshi Morita², and Per Augustsson¹
¹*Lund University, SWEDEN* and ²*University of Tokyo, JAPAN*
(Presented in Session 1 - Devices 1)
- P04 ACOUSTIC STREAMING-DRIVEN ADVECTION ENHANCEMENT OF ELISA SPEED AND SENSITIVITY**
Lei Zhang¹, Shuai Zhang¹, Cecile Floer², and James Friend¹
¹*University of California, San Diego, USA* and
²*Universite de Lorraine-CNRS, FRANCE*
(Presented in Session 2 - Biological and Biomedical Applications 1)
- P05 INTEGRATION OF A SILICON CHAMBER IN HYBRID ACOUSTIC WAVE DEVICES FOR PRECISE CELL PATTERNING AND CILIARY WAVEFORM ANALYSIS**
Mingyang Cui^{1,2}, Li Shan³, and J. Mark Meacham¹
¹*Washington University, St. Louis, USA*, ²*Massachusetts Institute of Technology, USA*, and ³*University of Texas, Dallas, USA*
(Presented in Session 2 - Biological and Biomedical Applications 1)
- P06 TRANSIENT BEHAVIOR AND ACOUSTIC STREAMING EFFECTS IN ACOUSTICALLY PACKED BLOOD**
Richard Soller, Ola Jakobsson, Wei Qiu, and Per Augustsson
Lund University, SWEDEN
(Presented in Session 3 - Physics: New Phenomena)
- P07 ULTRASONIC SINGLE-BEAM MANIPULATION OF PARTICLES AND ORGANIDS THROUGH A PETRI-DISH AND A PLASTIC TUBE USING AN ACOUSTIC FIELD LIVE-VISUALISATION METHOD**
Mario Ortega Sandoval, Krishna Coimbatore Balram, Luke Cox, Martha Lavelle, James Armstrong, and Bruce Drinkwater
University of Bristol, UK
(Presented in Session 3 - Physics: New Phenomena)

- P08** **POROS GIGA: ACOUSTOFLUIDIC PLATFORM FOR CLINICAL -
SCALE CELL ENGINEERING**
Mugdha Sinha^{1,2}, Mohammad Albuhsin^{1,2}, Jahir Islam¹, J. Mark Meacham^{1,2},
and Michael M. Binkley¹
¹*OpenCell Technologies, Inc., USA and*
²*Washington University, Saint Louis, USA*
(Presented in Session 4 - Biological and Biomedical Applications 2)
- P09** **ABOUT ALTERING EQUILIBRIUM POSITIONS OF PARTICLES TRAPPED
IN AN ACOUSTIC TWEEZER BASED ON A 2DSSAW**
Jörg König¹, Zhichao Deng¹, Sebastian Sachs¹, Hagen Schmidt²,
and Christian Cierpka^{1,3}
¹*TU Ilmenau, GERMANY, ²IFW Dresden, GERMANY, and*
³*Lund University, SWEDEN*
(Presented in Session 5 - Physics: Acoustic Fields and Streaming)
- P10** **ACOUSTOFLUIDIC TRAPPING AND ANALYSIS OF MICROSWIMMERS**
Advaith Narayan¹, Mingyang Cui², and J. Mark Meacham¹
¹*Washington University, St. Louis, USA and*
²*Massachusetts Institute of Technology, USA*
(Presented in Session 8 - Manipulation and Control)

Banquet

18:30 - 20:30 **Holmes Lounge**

Friday, 18 August

All Times are Central Daylight Time (CDT).

08:50 Announcements

Session 8 - Manipulation and Control

Session Chair: Per Augustsson, *Lund University, SWEDEN*

Contributed Talks

09:00 **PIEZOELECTRIC PHONONIC CRYSTAL-BASED ACOUSTIC TWEEZERS**

Feiyan Cai¹, Jun Wang^{1,2}, Yongchuan Li¹, Ke Deng², Hairong Zheng¹

¹*Shenzhen Institutes of Advanced Technology, CHINA and*

²*Jishou University, CHINA*

09:15 **ACOUSTOFLUIDIC TRAPPING AND ANALYSIS OF MICROSWIMMERS**

Advaith Narayan¹, Mingyang Cui², and J. Mark Meacham¹

¹*Washington University, St. Louis, USA and*

²*Massachusetts Institute of Technology, USA*

09:30 **SELF-ASSEMBLY AND SELF-ORGANISATION IN ACOUSTIC LEVITATION**

Mauricio A. Hoyos, Jean-Luc Aider, and Jean-Michel Peyrin

National Center for Scientific Research (CNRS), FRANCE

09:45 **MAPPING THE ACOUSTIC PROPERTIES OF TWO-PHASE SYSTEMS FOR USE IN DROPLET ACOUSTOFLUIDICS**

Qian Shi, Zhenhua Liu, Anna Fornell, Gabriel Werr, Laurent Barbe, and Maria Tenje

Uppsala University, SWEDEN

10:00 **ACOUSTOFLUIDIC DROPLET SEPARATION USING TRAVELING SURFACE ACOUSTIC WAVE-INDUCED ACOUSTIC RADIATION FORCE**

Mushtaq Ali and Jinsoo Park

Chonnam National University, KOREA

10:15 Coffee Break

Session 9 - Biological and Biomedical Applications 3

Session Chair: J. Mark Meacham, *Washington University in St. Louis, USA*

Invited Speaker 3

10:40 **ULTRASOUND WITH MICROBUBBLE-MEDIATED AGENT TRANSPORT IN AND OUT OF THE BRAIN**

Hong Chen

Washington University, St. Louis, USA

Contributed Talks

11:10 MEASUREMENT OF ACOUSTIC CONTRAST OF HEMATOPOIETIC STEM CELLS BY TRAJECTORY ANALYSIS

Ryan Dubay¹, Jennifer L. Walker¹, Jayanth Dabbi¹, John Manis²,
and Jason Fiering¹

¹Draper, USA and ²Harvard Medical School and Boston Children's Hospital, USA

11:25 CAPILLARITY-VISCOSITY-DRIVEN TRAVELLING WAVES IN SUPERHYDROPHOBICITY-SUPPORTED SHALLOW GAS

Maxime Fauconnier, Bhuvaneshwari Karunakaran, Alex Drago Gonzalez,
William Wong, Robin Ras, and Heikki Nieminen
Aalto University, FINLAND

11:40 Award Announcements

12:05 Announcement of Acoustofluidics 2024

12:10 Conference Adjourns

High-power bulk wave acoustofluidics

Enrico Corato¹, Ola Jakobsson¹, Wei Qiu¹, Takeshi Morita², and Per Augustsson¹

¹Department of Biomedical Engineering, Lund University, Lund, Sweden

E-mail: enrico.corato@bme.lth.se

²Department of Precision Engineering, The University of Tokyo, Tokyo, Japan

Introduction

Acoustofluidics needs high-energy devices to meet clinical applications requirements. This is particularly true when manipulating sub-micron particles [1], as the acoustic radiation force scales with the particle's volume, or to meet demands for sample throughput. Recently, focusing of 5- μm -polystyrene particles was demonstrated at 2 ml/min thanks to careful transducer positioning and dimensioning [2]. Such bulk-wave acoustofluidic devices have been classically driven simply by piezoelectric elements, without much consideration of the transducer design. In this experimental work we show how a double-parabolic-reflectors wave-guided high-power ultrasonic transducer (DPLUS) can be adapted to achieve high-intensity acoustic resonance inside a microchannel. The classic axisymmetric design of the DPLUS has been demonstrated to achieve high amplification of sound in a point [3]. From the original design, we present here for the first time a line DPLUS (L-DPLUS, Fig.1) acting along the length of a microfluidic channel. Doing so, we could focus plane waves onto the chip from two piezoelectric elements much bigger than the chip itself. Furthermore, the metal structure decouples thermally the piezoelectric elements from the microfluidic channel, thus avoiding temperature increase inside the fluid.

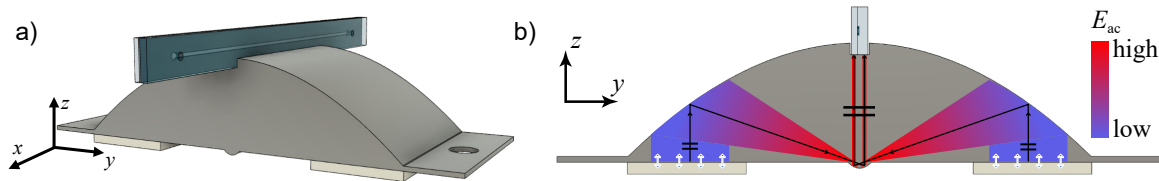


Figure 1: a) L-DPLUS rendering, with the two piezoelectric elements at the bottom (white) and the glass-silicon-glass microfluidic chip on top. b) L-DPLUS cross-section, with schematic representation of the working principle: the piezoelectric elements generate plane waves (blue arrows with white contours), which are focused by the first reflector into its focal point. Conversely, the second reflector converts the focused sound back into plane waves, which are eventually guided to the slot where the chip sits. Ideally, the sound magnification is proportional to the ratio between the second and the first parabola focal lengths.

Materials and methods

Starting from the original DPLUS design [3], we extruded the parabolic cross-section 20 mm in the x -direction (Fig.1). We then milled a slot on the top of the structure to accommodate a glass-silicon-glass chip with a 375- μm -wide and 150- μm -deep microchannel, etched through the silicon layer and 40 mm long. The chip was glued in the slot on top and, conversely, two piezoelectric elements ($10 \times 20 \text{ mm}^2$) were glued on the L-DPLUS backside. They were driven by a common sinusoidal electrical signal, amplified by a power amplifier to reach constant high voltage (50 V_{pp}) during experiments. For stop-flow experiments, the 5- μm -polystyrene particles focusing was tracked using defocusing-based particle tracking [4] along the whole L-DPLUS length.

Results and discussion

The system was initially tested at a flow rate of 6 ml/min, corresponding to 11.25 ms average particle residence time in the acoustic field. Fig.2 shows the achieved focusing (in terms of full width at half-maximum of the focused particles intensity profiles) by scanning the frequency between 1.8 and 2.0 MHz, together with the corresponding electrical power applied to both transducers. This latter parameter varies greatly (min 2.915 W, max 14.34 W) due to the piezoelectric elements changing impedance depending on the frequency. Due to the high electrical power applied, we encountered fast

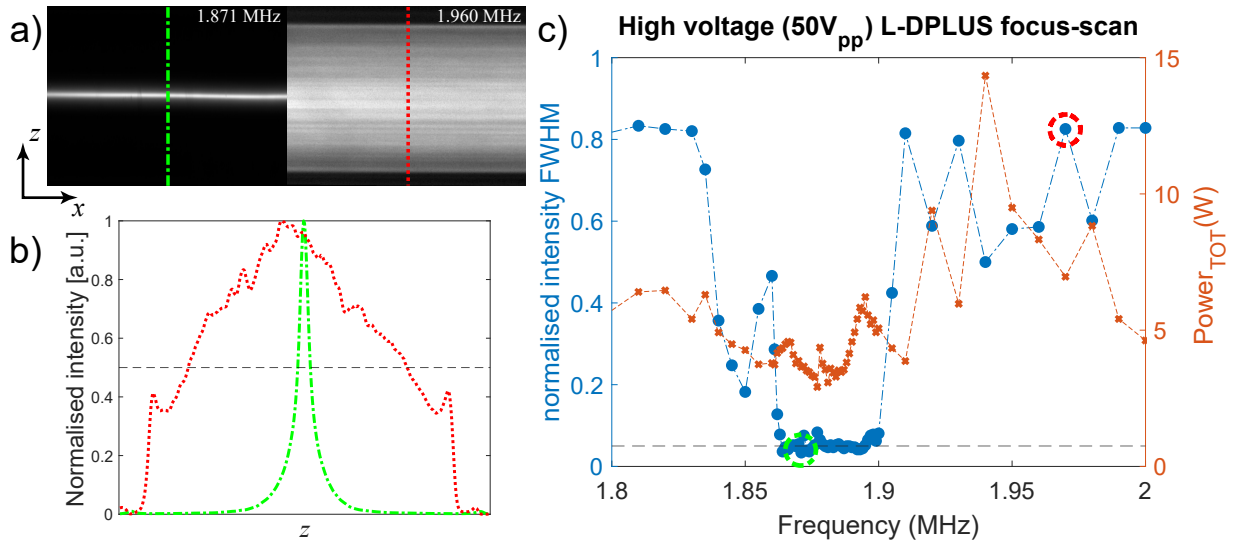


Figure 2: a) With a constant voltage of 50 V_{pp} and a flow of 6 ml/min, the particle focusing can be narrow (1.871 MHz) or very broad (1.960 MHz). b) Corresponding intensity profiles for good (1.871 MHz, green) and poor (1.960 MHz, red) focusing. The black dashed line shows the full width at half-maximum (FWHM) level. c) FWHM (blue circles) was measured for frequencies between 1.8 and 2.0 MHz. The corresponding total power consumption by the piezoelectric elements is plotted with orange crosses. The best focusing is at 1.871 MHz (green), with an electrical power of 3.649 W. However, a more efficient actuation frequency could be 1.881 MHz, which has a lower power consumption (3.08 W), while still achieving focusing below 5% (dashed black line).

heating of the piezoelectric elements, which in turn quickly decreased the device performance. Hence, images were only acquired within few seconds after the actuation commencement. Also in Fig.2, it is worth noting the broad frequency range (1.864-1.895 MHz) at which the focusing bandwidth remains around 5% of the channel width, with the lowest value (3.39%) at 1.871 MHz. At this frequency, we performed a stop-flow focusing experiment so to characterise the acoustic field along the whole L-DPLUS length. The particle velocity is plotted in Fig.3a. In Fig.3b, the estimated E_{ac} is shown varying along x , with an average value of 1020 J/m³.

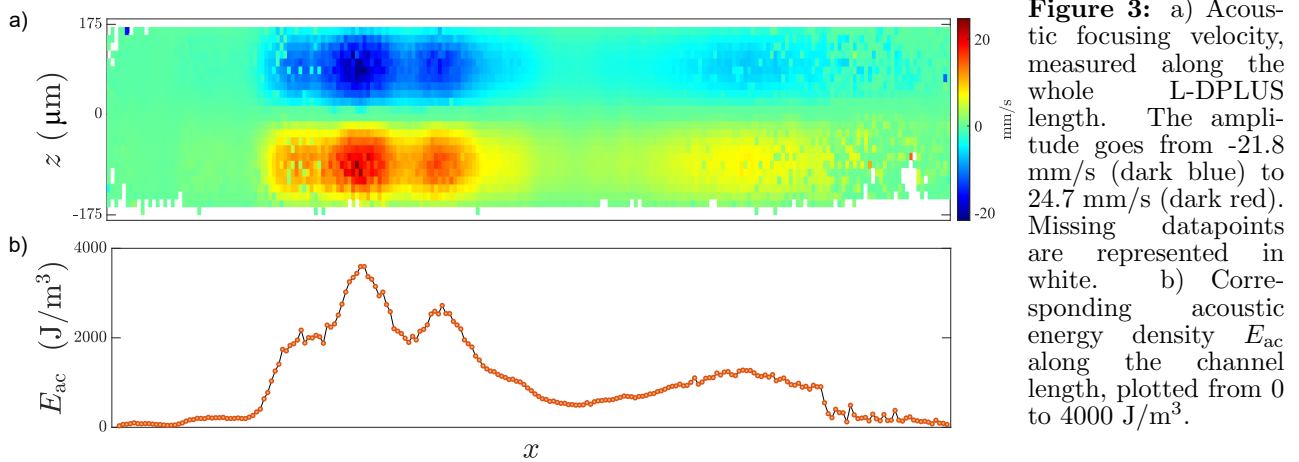


Figure 3: a) Acoustic focusing velocity, measured along the whole L-DPLUS length. The amplitude goes from -21.8 mm/s (dark blue) to 24.7 mm/s (dark red). Missing datapoints are represented in white. b) Corresponding acoustic energy density E_{ac} along the channel length, plotted from 0 to 4000 J/m³.

Conclusion

We showed a first application of L-DPLUS, resulting in a maximum acoustic energy density was 3592 J/m³, which is, to the best of our knowledge, the highest ever reported for a bulk acoustic wave device. We now aim to improve the efficiency of the system, so to reach high enough flow rates without significant performance degradation. The next step will be to evaluate this method for biological micro- and nano-particle separation. Furthermore, we would like to investigate the energy level for which the acoustic field starts damaging biological particles.

References

- [1] Van Assche, D., Reithuber, E., Qiu, W., Laurell, T., et al., Sci Rep **10**, 3670 (2020).
- [2] Qiu, W., Baasch, T., and Laurell, T., Phys. Rev. Appl. **17**, 044043 (2022).
- [3] Chen, K., Irie, T., Iijima, T., and Morita, T., Appl. Phys. Lett. **114**(7), 072902 (2019).
- [4] Barnkob, R., and Rossi, M., J. Open Res. Softw. **9**(1), 22 (2021).



Acoustic Manipulation of Particles in Microfluidic Chips with an Adaptive Controller that Models Acoustic Fields

Kyriacos Yiannacou¹ and Veikko Sariola¹

¹ Faculty of Medicine and Health Technology, Tampere University, URL: <https://research.tuni.fi/bmr-group/>
 Korkeakoulunkatu 3, PL 692, 33014 Tampereen yliopisto, Finland, E-mails: kyriacos.yiannacou@tuni.fi,
veikko.sariola@tuni.fi

Introduction Acoustic manipulation using closed-loop control methods, which rely on complex and time-varying acoustic fields, typically necessitates precise models of these fields. These models can be obtained through first principles or data-driven approaches involving numerous training experiments. However, acquiring such accurate models can pose a considerable challenge. In our previous research, we introduced a method for actively controlling the position of particles and droplets, based on the ϵ -greedy machine learning algorithm.^[1,2] This method was used to manipulate and sort particles, as well as manipulate and merge droplets, all within the same chip. The algorithm learns online how to manipulate the particles/droplets. However, a notable drawback of that method was its limited long-term memory: the algorithm did not have any internal model of the acoustic fields. Consequently, the algorithm only learned the local movement patterns of the particles/droplets and quickly forgot them as the particles traveled a sufficient distance from their initial positions. As a result, in each manipulation experiment, the controller resorted to trial and error to determine the appropriate frequencies that would guide the particles towards their intended waypoints. This approach led to long manipulation times and poor path following accuracy.

Here, we develop the ideas of our previous algorithms further, by incorporating a long-term memory to them. The long-term memory is based on a regression model of the acoustic field shapes, but instead of using black box models like neural networks, we develop our models based on physical insights of the acoustic waves inside the chamber. The method uses machine learning to model the acoustic fields online: starting with no knowledge of the fields, the controller successfully manipulates particles even on the first attempt, and its performance improves in subsequent attempts, yet can still readapt if the models are invalidated by a sudden change in system parameters. We call the proposed new controller the *acoustic-model-based adaptive controller*, or AMA controller for short. The controller can use information learned from one task to improve its performance in other tasks. The proposed controller addresses and significantly improves the performance of the controllers proposed in our earlier work: both the manipulation speed and the path-following accuracy are improved. The online adaptiveness of the controller makes it suitable for practical applications such as particle and cell sorting, micro assembly, labs-on-chips, and diagnostic devices, as it does not require extensive training or prior models.

Methods A diagram of our experimental setup is shown in Figure 1a. Our system consists of a glass microfluidic chip, a piezoelectric transducer (CTS-Noliac, NCE 46, 15mm × 15mm × 2mm) mounted on the backside of the chip, a camera (Basler acA2040-120uc) to image the particles/droplets inside the chip, a computer running the machine vision and control algorithms, an arbitrary waveform generator (PCI-5412, National Instruments), an amplifier (1040L, Electronics and Innovation), and a syringe pump (Aladdin, World Precision Instruments).

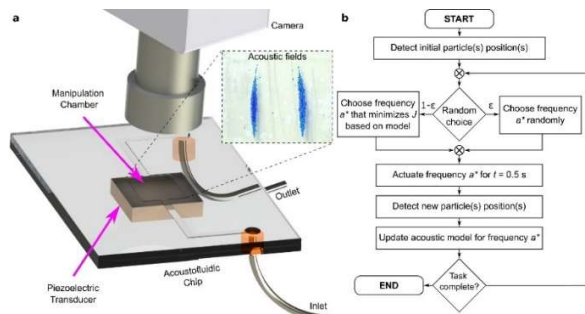


Figure 1. a) Schematic diagram of the experimental setup. b) Flowchart of the control algorithm.

Inside the chip, there is a rectangular chamber with dimensions of 7 mm × 6 mm × 0.15 mm. For the manipulation experiments, we used polystyrene microparticles (DBP70K, LAB261, Palo Alto, CA, USA,

density: 1.05 g cm^{-3} , diameter: $70 \text{ }\mu\text{m}$). The control algorithm flowchart is shown in Figure 1b. Briefly, at the start of each control cycle, the machine vision detects the particle positions of the particles and must decide which frequency to actuate next. The frequency is chosen from a discrete set A of 100 linearly spaced frequencies in the range of $65 \text{ kHz} - 700 \text{ kHz}$. The choice between exploration and exploitation is made randomly: with the probability of ϵ , the frequency is chosen completely randomly, while otherwise, the controller chooses the frequency that takes the particles closest to their current targets, according to its internal acoustic model. The model tries to capture the shape of the Gor'kov potential; the particle being assumed to be driven by the gradient of the Gor'kov potential. The potential is modeled by determining the coefficients of the Fourier decomposition that best fit the potential shape.

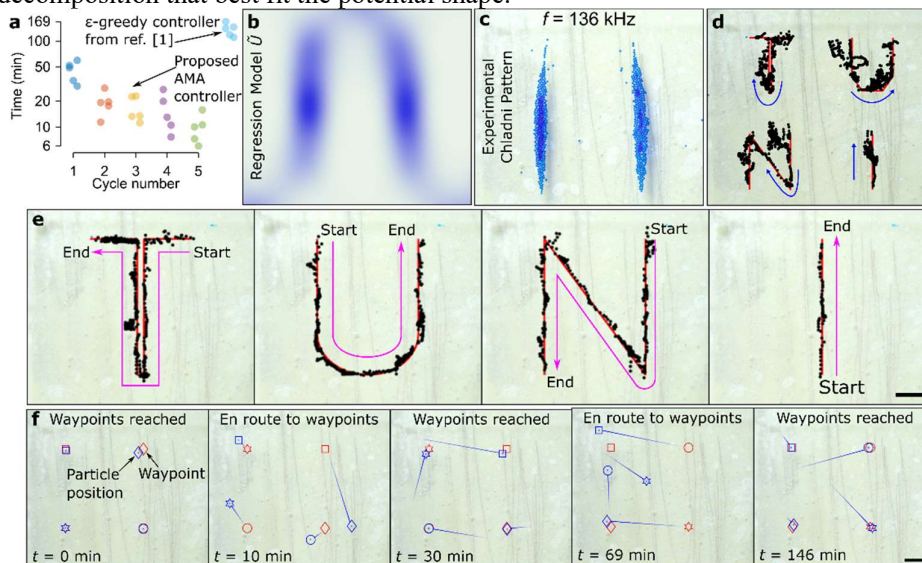


Figure 2. **a)** Manipulation times for the proposed AMA controller, compared to the ϵ -greedy controller from our previous work.^[1] **b)** Regression based Gor'kov potential model for the frequency in (c). **c)** Experimentally observed acoustic pattern, **d)** Trained AMA controller completing simultaneous manipulation of four particles through four independent paths. **e)** Trained AMA controller completing a manipulation task it has never done earlier. **f)** Trained AMA controller manipulates and positions four particles in the chamber.

Results We compared the new AMA controller to the ϵ -greedy controller from our previous work,^[1] Both controllers were tested in a manipulation experiment where they guided a $70 \text{ }\mu\text{m}$ polystyrene particle through a rectangular path. The AMA controller repeated the path five times, and all experiments were repeated five times from the beginning. Results in Figure 2a indicate that the AMA controller improved its manipulation times with each cycle, suggesting it retains information from previous experiments.

To demonstrate the controller's ability to generalize knowledge, we trained it on a generic manipulation task and then tested it on a completely new task. The training task involved the particle visiting various points in the chamber. The trained controller successfully manipulated multiple particles (Figure 2d&f) and a single particle along a rectangular path. This shows that it can apply its learned knowledge to unfamiliar tasks (Figure 2d&f). We further established the relationship between the controller's knowledge and the acoustic field shapes in the chamber. We compared the regression models learned during training with experimentally obtained acoustic patterns using space-filling curves. By visualizing the acoustic patterns created by multiple particles, we observed a clear correspondence between the modeled and observed patterns (Figure 2b&c). This indicates that the internal regression model of our AMA controller has a physical interpretation—it approximates the Gor'kov potential for that frequency. Remarkably, this model was obtained solely from experiments involving the manipulation of a single particle.

Conclusion The proposed AMA controller can learn and utilize the acoustic field shapes within the chip, leading to improved performance in subsequent repetitions of a task. Additionally, even in tasks it has never encountered before, the controller demonstrates enhanced performance since the controller has information of the acoustic field shapes within the chamber, rather than relying solely on task-specific actions. The internal acoustic model of the controller effectively captures the shape of the Gor'kov potential for each frequency. This interpretability of the model provides a notable advantage over purely black-box methods, as it enables direct comparison with experimentally observed acoustic field shapes, as demonstrated in our study.

References

- [1] K. Yiannacou, V. Sariola, *Langmuir* **2021**, *37*, 4192.
- [2] K. Yiannacou, V. Sharma, V. Sariola, *Langmuir* **2022**, *38*, 11557.



Fully Microfabricated Surface Acoustic Wave Tweezer for (sub-)micron Particle Focusing

Armaghan Fakhfouri¹, Melanie Colditz¹, Citsabehsan Devendran², Stefan Jacob³, Kateryna Ivanova¹, Adrian Neild² and Andreas Winkler¹

¹Leibniz-IFW Dresden, Helmholtzstr. 20, 01069 Dresden, Germany

E-mail: a.fakhfouri@ifw-dresden.de

²Department of Mechanical and Aerospace Engineering Monash University, Clayton, Victoria 3800, Australia

³Physikalisch-Technische Bundesanstalt, Brunswick, Germany

Introduction

Surface acoustic wave (SAW) tweezers are increasingly emerging as enabling technologies for focusing and sorting of nano-and-micro-scale particles. Coupling of SAWs into a liquid for manipulation of immersed cells is typically achieved by employing a microfluidic channel material capable of absorbing most of the acoustic energy (e.g. Polydimethylsiloxane (PDMS)). This widely used technique, however, lacks reproducibility, biological compatibility and suitability for cost-efficient large-scale production. The use of channels consisting of acoustically reflective materials, require a different actuation technique which includes resonance of the entire channel as shown, so far only in glass microchannels manually aligned on piezoelectric substrates [1]. Channel-resonance-based cell manipulation has a much higher sensitivity to the channel architecture and material. It is, therefore, essential to employ a technique capable of highly precise translation of a designed channel architecture into real-life systems. An approach capable of promoting such consistency to the SAW-driven technology has so far remained elusive, but will be demonstrated in this work.

Theory and Results

This work demonstrates a new manufacturing approach for SAW tweezers and their validation in particle and cell focusing. Central to this approach is the wafer-scale lithographic integration of microchannels in laminated dry-film-resist (DFR) bilayers enabling realization of the precise dimensions and detailed architecture required for a resonating system. Whilst a popular approach in MEMS, circuit board fabrication and, only recently, for passive microfluidics, to the best of our knowledge, the application of DFR for acoustic particle manipulation has not been proposed so far. The defined and reproducible manufacture of SAW acoustofluidic chips on the wafer scale using DFR lamination technique obviates the fundamental limits of soft-lithography including bonding inconsistencies, alignment issues and microchannel deformation, as such permits a predictable acoustofluidic interaction with cells and particles by FEM simulation. Furthermore, excitation of the channel resonance driven by SAW provide us with the unique opportunity to design an acoustic field wherein the otherwise competing acoustic forces, including acoustic radiation force and acoustic streaming induced drag force, complement each other. This is possible by carefully designing the channel dynamics to align the equilibrium position of both forces providing a consistent location for collection of particles and cells, thus markedly reducing the size of collectable particles, (down to 200 nm, even at relatively low frequency of 12.8 MHz) [2]

Conclusion

Our unique SAW tweezer exhibits collection and focusing of spherical particles ranging from 0.2 to 3 μm and biological cells existing in human blood including erythrocytes (7–8 μm), leukocytes (7–20 μm), and thrombocytes (1–4 μm). The excellent ability in collection of particles and cells independent of their dimension and shape, along with reproducibility, cost efficiency, and mass producibility make the integration of DFR onto SAW tweezers promising for translation of SAW microfluidics to real-world medtech implementations.

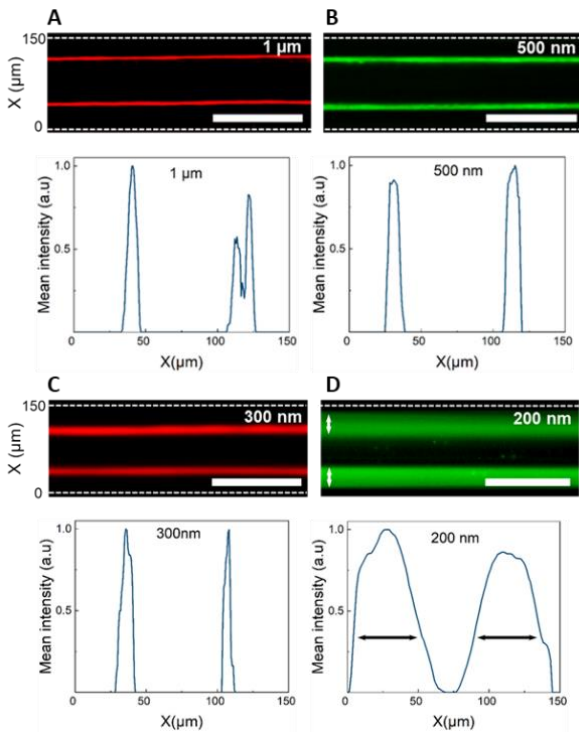


Figure 1: Experimental proof of submicron particle focusing immersed in liquid bound by DFR channel excited by opposing identical straight IDTs ($\lambda_{SAW}=300 \mu\text{m}$, 12.8 MHz) and a channel width of $150 \mu\text{m}$ ($W = \lambda_{SAW}/2$) flowing at $0.3 \mu\text{l}/\text{min}$: (A) $1 \mu\text{m}$ at 20 mW, (B) 500 nm at 50 mW, (C) 300 nm at 80 mW, and (D) 200 nm at 600 mW. Scale bars are $200 \mu\text{m}$.

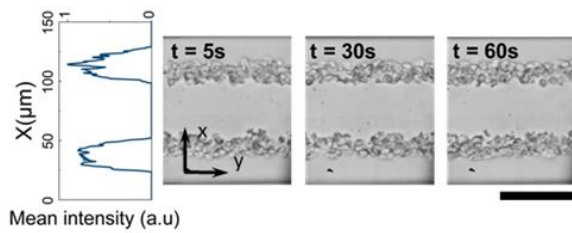


Figure 2: Focusing of human-blood components into two streams occurring immediately and retaining a temporal stable stream pattern upon continuous application of SAW at 400 mW and 12.8 MHz flowing at $25 \mu\text{l}/\text{min}$.

References

- [1] Z. Mao, P. Li, M. Wu, H. Bachman, N. Mesyngier, X. Guo, S. Liu, F. Costanzo, and T.J. Huang, ACS Nano **11**, 603-612 (2017).
 [2] A. Fakhouri, M. Colditz, C. Devendran, K. Ivanova, S. Jacob, A. Neild, and A. Winkler. ACS Appl. Mater. Interfaces **15**, 20, 24023–24033 (2023).

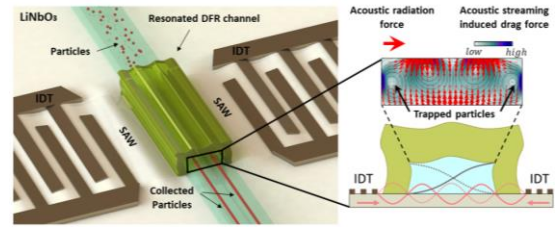


Figure 3: Principle of DFR channel excitation driven by SAW leading to collection of (sub-)micron particles.

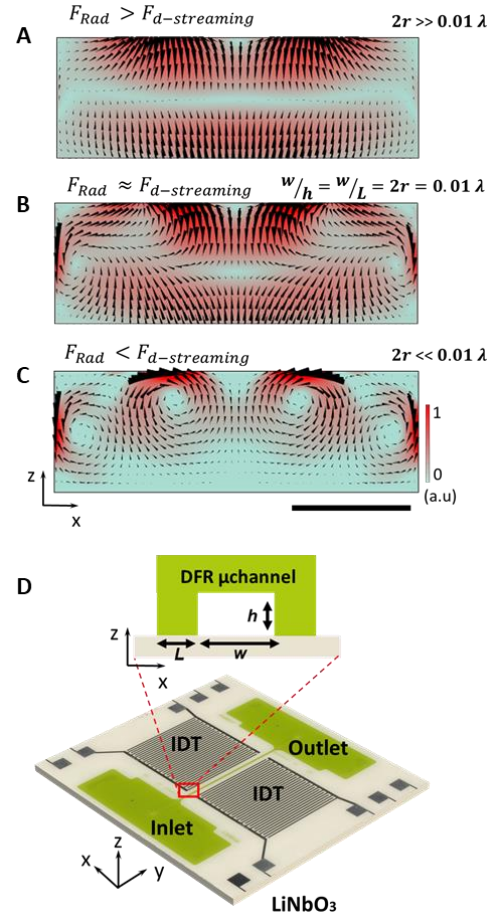


Figure 4: Numerical simulation of combined effect of acoustic forces, acoustic radiation force (F_{Rad}) and acoustic streaming drag force ($F_{d-streaming}$) where particles diameter ($2r$) is (A) greater than $0.01 \lambda_{SAW}$ (B) equal to $0.01 \lambda_{SAW}$ and, (C) smaller than $0.01 \lambda_{SAW}$. Regardless of dominant initial effect, both forces act together to displace particles and eventually trap them in the locations where both forces are minimum.



Acoustofluidics - From Research towards Healthcare

Mikael Evander¹

¹AcouSort AB, Lund, Sweden

E-mail: Mikael.Evander@acousort.com, URL: <https://www.acousort.com>

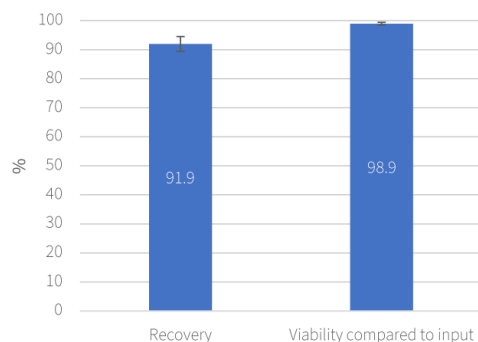
Introduction

In the last decades, acoustofluidics has evolved from mainly being used in university research labs to becoming a sought-after tool within the healthcare sector. This transition requires both evolution of the technology platform as well as dedicated application development to show both relevant data as well as high reproducibility and stability of the systems used. This presentation will highlight some of the work carried out within our company that allows acoustofluidics to move into the healthcare sector within blood diagnostics and new fields such as personalized cell therapy.

Acoustic trapping for cell enrichment and washing

Acoustic trapping has been used as a tool for capturing particles, cells, bacteria and extracellular vesicles for many years. The AcouTrap platform, where an acoustic trap is mounted as the tip of a pipetting robot, has been used in several publications targeting different applications with precious samples in smaller volumes. For cell applications, our standard trapping unit has typically been used for up to 60 000 cells where it is difficult to find competing technologies that will not lose cells during the sample processing. Although the trapping unit has recently been updated to handle up to 100 000 cells, an even higher cell capacity would open up the technology for more applications.

A trapping unit with increased capacity and throughput has now been developed. A piezoceramic element, resonant at 4 MHz, is used to create a standing wave with 5 pressure nodes in an extruded glass channel. Using cultured Jurkat cells, the trapping unit was tested for total cell capacity, recovery and whether the viability compared to the input sample was maintained. Figure 1 shows the results from the recovery and viability measurements using 400 000 cells. The viability was maintained compared to the input sample and a recovery of >90% was seen for the samples. The maximum capacity was measured to 500 000 cells and processing flow rates of 50 – 300 μ l/min has been successfully tested.



(A)



(B)

Figure 1: (A) The recovery and viability of cultured Jurkat cells in a 5-node trapping unit after processing in the AcouTrap instrument. A total number of 400 000 cells were used with $n = 14$ and $n = 8$ for the respective measurements. The cells were aspirated and trapped while a 2 min wash was performed to remove any cells that were not trapped. The ultrasound was deactivated, and the cells released for flow cytometry analysis. (B) A photo of the AcouTrap instrument used for the experiments.

With the increased capacity trapping unit, it was possible to start working with an application aimed towards personalized cell therapy. Stem cells are usually kept frozen and to maintain viability after thawing, 5 – 10% dimethyl sulfoxide (DMSO) is typically added to the cell sample. DMSO, however, is known to have several side-effects on humans and should preferably be removed from the cell suspension before being administered to the patient. Cell medium with 10% DMSO has both higher viscosity and density compared to plain phosphate-buffered saline (PBS) solution which makes it difficult to perform a stable cell wash on the sample. By diluting the thawed cell suspension 1:1 with PBS + 0.4 % bovine serum albumin (BSA), it was possible to trap the cells and wash away the DMSO. A recovery of 89% was achieved while maintaining the cell viability, see figure 2. The removal of DMSO was measured indirectly by spiking the sample with 1 µg/ml fluorescein and a 1000x reduction of the fluorescence was seen after a 2-minute wash.

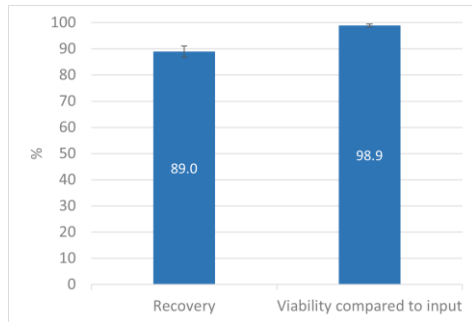
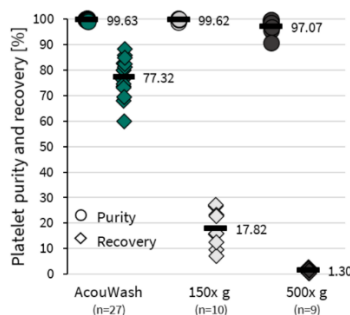


Figure 2: The recovery and viability of a sample containing 400 000 Jurkat cells in 10% DMSO after trapping and washing (n = 4). The cell sample was diluted 1:1 with PBS with 0.4% BSA added. The cells were trapped and washed for 2 minutes using PBS + 0.4% BSA and then released for flow cytometry analysis.

Acoustic separation of cells, blood plasma and platelets

Platelets play a key role in the human body and are routinely used in a variety of clinical applications. Recent research has also shown that platelets may be used to detect cancer due to their role in tumorigenesis. The isolation of platelets is, however, a sensitive process where care must be taken not to activate the platelets but also to maintain their ability to activate upon stimulation. The standard method for platelet isolation is still centrifugation which can yield large variation in cell concentration and purity depending on the specific centrifuge used and the operator.

Using whole blood as input sample, an acoustofluidic separation instrument, AcouWash, was compared to two different centrifugation protocols, see figure 3. The results show that the acoustic isolation method could produce >99% platelet purity with < 0.1% WBC contamination and > 99% RBC removal. No induced platelet activation was measured, and the activation capacity of the isolated platelets were better preserved in the acoustically isolated platelets than in the centrifuged platelets.



(A)

(B)

Figure 3: (A) A comparison of the recovery and purity of platelets isolated using either Acoustofluidic separation or two different centrifugation protocols performed in a swing bucket rotor for 20 min either at 150x g or 500x g. Input and output samples were stained for CD45, CD61, and CD235a and analyzed by flow cytometry using a BD FACS Canto II. (B) A photo of the AcouWash instrument used for the experiments.

Conclusion

Moving acoustofluidics into healthcare as a tool in advanced medicine such as blood diagnostics and cell therapy requires continuous work on improved capacity, throughput and optimization of relevant clinical applications. AcouSort has been able to focus on this continued development of our benchtop instruments and OEM-components to be used in diagnostic and therapeutic instruments through publicly funded projects and collaboration with large global companies within the cell therapy field. The examples highlighted in this abstract show some of our work towards acoustic trapping of stem cells for personalized cell therapy and platelet isolation for use in e.g. cancer detection.

Acknowledgements

Part of this work has been funded by the European Union through the European Innovation Council (EIC) project AcouSome (www.AcouSome.com).

Acoustic Streaming-Driven Advection Enhancement of ELISA Speed and Sensitivity

Lei Zhang¹, Shuai Zhang¹, Cécile Floer², and James Friend¹

¹Medically Advanced Devices Laboratory, Department of Mechanical and Aerospace Engineering, University of California, San Diego, CA 92093, United States
E-mail: jfriend@ucsd.edu

²Institute Jean Lamour UMR 7198, Université de Lorraine-CNRS, 54000 Nancy, France

Introduction

Enzyme-linked immunosorbent assays (ELISA) are widely used in biology and clinical diagnosis. However, the standard ELISA protocol can be time-consuming [1]. Relying on antigen-antibody interaction through diffusion, it can take up to 20 hours, preventing its use in rapid diagnostics. Acoustofluidics has its advantages in significantly speeding up phenomena that rely on diffusion [2,3]. We hypothesize that enhancing this antigen-antibody interaction through acoustic streaming-driven advection could decrease the binding time and potentially improve the ELISA's sensitivity. Experiments have been done by using surface acoustic wave (SAW) devices to drive advection. The binding process is increased by 294% to reduce the time needed for ELISA from 1 hour at 37°C to 10 minutes with SAW. The sensitivity is also enhanced by the total antigen-antibody binding increased by 83% under 20 mins SAW stimulation.

Materials and method

Single crystal lithium niobate (128° Y-rotated cut) was used as a substrate to fabricate 5 nm Cr/400 nm Au interdigital transducers (IDT) to produce 60 MHz Rayleigh SAW for 4W transmitted as an acoustic wave into an attached well laid upon it (Fig. 1a); ELISA was conducted in the well. Anti-protein A antibody and goat anti-chicken IgY (HRP) were used to simulate the antigen-antibody binding process in a standard ELISA protocol; 3,3',5,5'-tetramethylbenzidine (TMB) was added to produce an enzymatic degradation of hydrogen peroxide by horseradish peroxidase (HRP) as a visualizing reagent.

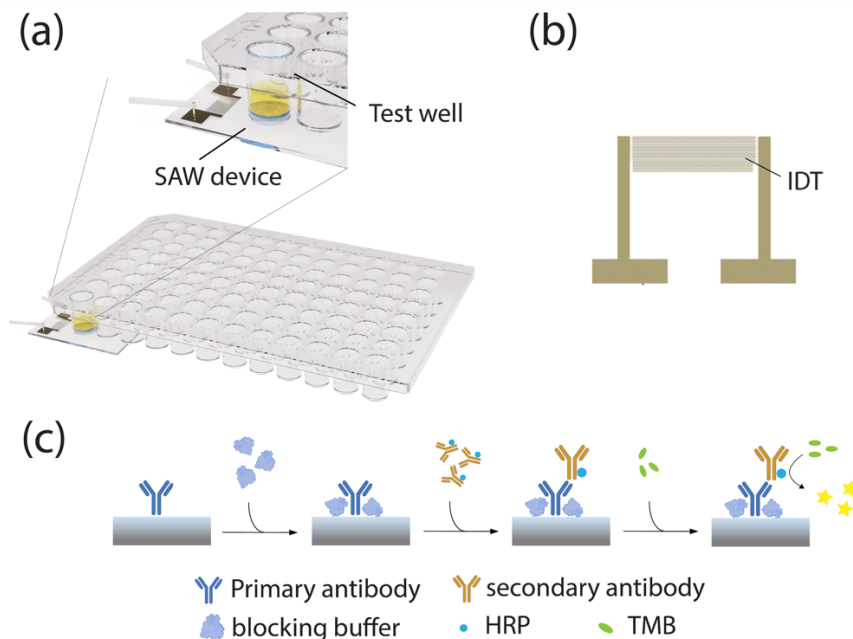


Figure 1: SAW-driven ELISA schematic. (a) Overview of the experimental set-up. Test well is 7mm in diameter containing 200 μL reagent solution. (b) Top view of the IDTs structure, producing 60 MHz Rayleigh SAW for 4W. (c) Illustration of a complete ELISA protocol with the acoustic streaming device.

Effect of SAW on antibody-antigen binding in traditional ELISA

To test the effect of the Rayleigh-SAW on the antigen-antibody binding, we immobilized the anti-protein A antibody on the bottom of the 96-wells plate, followed with blocking buffer and added goat anti-chicken IgY-HRP. The SAW was applied at this step to mix the solution from 1 to 15 minutes. The binding efficiency was measured by the absorbance. Figure 2(a) compares the normalized signal intensity of the TMB-HRP reaction after antibody binding with and without SAW-driven acoustic advection. SAW-driven advection greatly increases the binding rate: only 10 minutes are required with SAW ELISA to achieve the same result as 1 h of no-SAW ELISA at 37°C (Fig. 2a, red line). Using SAW increases the signal intensity by 64% for 1 min ELISA to 294% for 15 min ELISA.

Effect of SAW on ELISA sensitivity

We investigated the feasibility of utilizing SAW to increase the sensitivity of ELISA under varying concentrations of antigen. The goat anti-chicken IgY-HRP was diluted with PBS to create a concentration range spanning from 0.1 ng/ml to 10 ng/ml, and SAW was stimulated for a duration of 20 minutes to ensure sufficient antigen-antibody binding. Comparing the sensitivity with 20 min SAW-driven ELISA to standard 1 h no-SAW ELISA at 37°C indicates that the binding linearly increases with concentration, with slopes of 0.0529 and 0.0289, respectively (Fig. 2b), demonstrating the improvement in quantification using ELISA with SAW stimulation. The total antigen-antibody binding is found to increase by 83% under SAW stimulation.

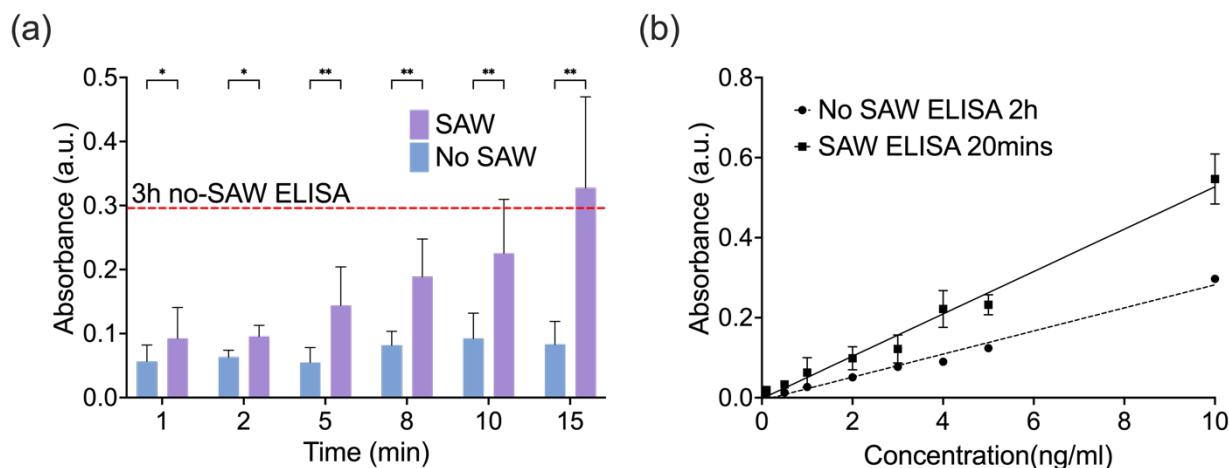


Figure 2: (a) Time course of antibody-antigen binding under SAW mixing and control. (N=6) (b) Sensitivity of antibody-antigen binding under SAW mixing and control. (N=3). Error bars represent standard deviation in all plots.

Conclusion

We proved the feasibility of using SAW to improve the speed and sensitivity of standard ELISA, potentially offering a promising means to improve ELISA's utility in point-of-care diagnostics.

References

- [1] M. M. Serrano, D. N. Rodríguez, N. T. Palop, R. O. Arenas, M. M. Córdoba, M. D. O. Mochón and C. G. Cardona, *Journal of Clinical Virology*, 2020, 129, 104529.
- [2] J. R. Friend and L. Y. Yeo, *Reviews of Modern Physics*, 2011, 83, 647–704.
- [3] K. Sritharan, C. Strobl, M. Schneider, A. Wixforth and Z. v. Guttenberg, *Applied Physics Letters*, 2006, 88, 054102.



Integration of a silicon chamber in hybrid acoustic wave devices for precise cell patterning and ciliary waveform analysis

Mingyang Cui^{1,2}, Li Shan^{1,3}, and J. Mark Meacham¹

¹Department of Mechanical Engineering and Materials Science, Washington University in St. Louis, St. Louis, MO 63130, USA

E-mail: mycui@mit.edu, meachamjm@wustl.edu; Web: <https://meachamlab.wustl.edu>

²Research Laboratory of Electronics, Massachusetts Institute of Technology, Cambridge, MA 02139, USA

³Department of Mechanical Engineering, University of Texas at Dallas, Richardson, TX 75080, USA

Introduction

Precise cell and particle manipulation is critical to various biological and biomedical applications. Acoustofluidics, which incorporates ultrasound acoustics into microfluidic platforms, has emerged as a compelling active particle manipulation technology for its non-contact, label-free, and gentle characteristics. However, trapping robust microswimmers like the single-cell alga *Chlamydomonas reinhardtii* (CR) remains a challenge due to a high required input power that can lead to device heating [1]. Recently, our group has integrated a surface acoustic wave (SAW) actuator and bulk acoustic wave (BAW) trapping array to achieve sufficient trapping forces to hold CR in place [1,2]. The hybrid BAW/SAW acoustic tweezers generated high trapping forces at low input power, providing the high temporal and spatial resolution needed to characterize the cilia dynamics of swimming CR. While hybrid devices enabled prolonged observation of individual cells, multiplexing was limited by nonuniform field shapes. The rounded edges of the isotropically etched glass chamber produced trapping arrays with missing nodes. In addition, high-frequency operation suffered from low energy conversion as the isotropic etching effect became exaggerated for smaller chamber sizes. To address these issues, herein we introduce a BAW/SAW device with a silicon/glass fluidic structure created using a novel fabrication process. Silicon processing precisely defines the chamber geometry to achieve better-defined trapping arrays, while the glass/silicon assembly allows for high resolution oil-immersion microscopy of ciliary movement at significantly reduced input power.

Experimental

Square silicon chambers were etched in a 500- μm thick wafer to a depth of 25 μm (side length = 545 μm) using deep reactive ion etching (DRIE). Chambers were enclosed by anodic bonding to a 175- μm thin glass wafer. The opposite side of the silicon wafer was then wet etched in a potassium hydroxide solution to remove ~ 400 μm , before completing the etch to the chamber depth using DRIE. Thin glass chambers were fabricated as describe previously [1,3]. Both thin glass and silicon/glass chambers were bonded to 128° Y-cut, X-propagating lithium niobate with pairs of interdigital transducers (IDTs) designed to operate at 10 and 20 MHz (spacing of 100 and 50 μm , respectively). The IDTs were created using standard photolithography, thermal evaporation (Cr/Au, 10 nm/80 nm), and liftoff processes. IDTs were driven by an amplified sinusoidal signal at resonant frequencies identified by visual observation of particle focusing near design frequencies. Biciliate wildtype (strain CC-125) cells were obtained from the Dutcher Lab at Washington University in St. Louis. Cells were prepared at $\sim 5 \times 10^6$ cells/mL for two-dimensional (2D) patterning experiments and diluted 10X for single-cell trapping and imaging. Single-cell trapping studies were imaged using a 100X oil-immersion objective at 2000 fps. Post processing and image analysis were performed using custom MATLAB codes.

Results and discussion

A single pair of IDTs generated a standing SAW in one direction that actuated a 2D standing BAW field in a square glass chamber oriented at 45° to the SAW propagation direction (Fig. 1a). Swimming biciliate CR cells exposed to SBAW were held in place by a strong acoustic radiation force opposing the direction of the swim force. The microswimmers were confined to the acoustic pressure nodes, which also allowed high resolution imaging of the ciliary beat. In this work, both square chambers of 10-MHz and 20-MHz devices were designed to yield 8 \times 8 grid patterns. However, the thin glass chamber did not exhibit regular grid patterns at either frequency due to the influence of rounded corners. Further, there was a slight mismatch of BAW and SAW resonant frequencies due to the poorly defined chamber dimensions (Fig. 1c and 1d). On the contrary, the Si/glass chamber showed significantly improved cell patterning. 8 \times 8 grid patterns were achieved in both 10-MHz and 20-MHz devices, although a small number of expected nodes were absent or merged (Fig. 1c and 1d). The vertical Si chamber walls also formed the standing BAW field more efficiently than the isotropically etched glass chambers, which is consistent with previous studies [4].

A detailed analysis of cilia dynamics for trapped CR is shown in Fig. 2. For CR cells held using the 10-MHz device, the cilia bend amplitude was ~ 0.90 rad (0.90 ± 0.08 rad, mean \pm SD; $n = 16$), which was not significantly different than that for cells held in the 20-MHz device (0.91 ± 0.04 rad). Similarly, the curvature values were comparable (-0.18 ± 0.03 rad/ μm , 10-MHz device; -0.18 ± 0.02 rad/ μm , 20-MHz device). However, the beat frequency for cells held in the 10-MHz device (69.3 ± 3.5 Hz) was slightly higher than for the 20-MHz device (63.1 ± 2.9 Hz). The difference in frequency may be attributed to an insufficient sample size, but it is more likely due to a slightly higher operating temperature ($\sim 2^\circ\text{C}$) for the 10-MHz device.

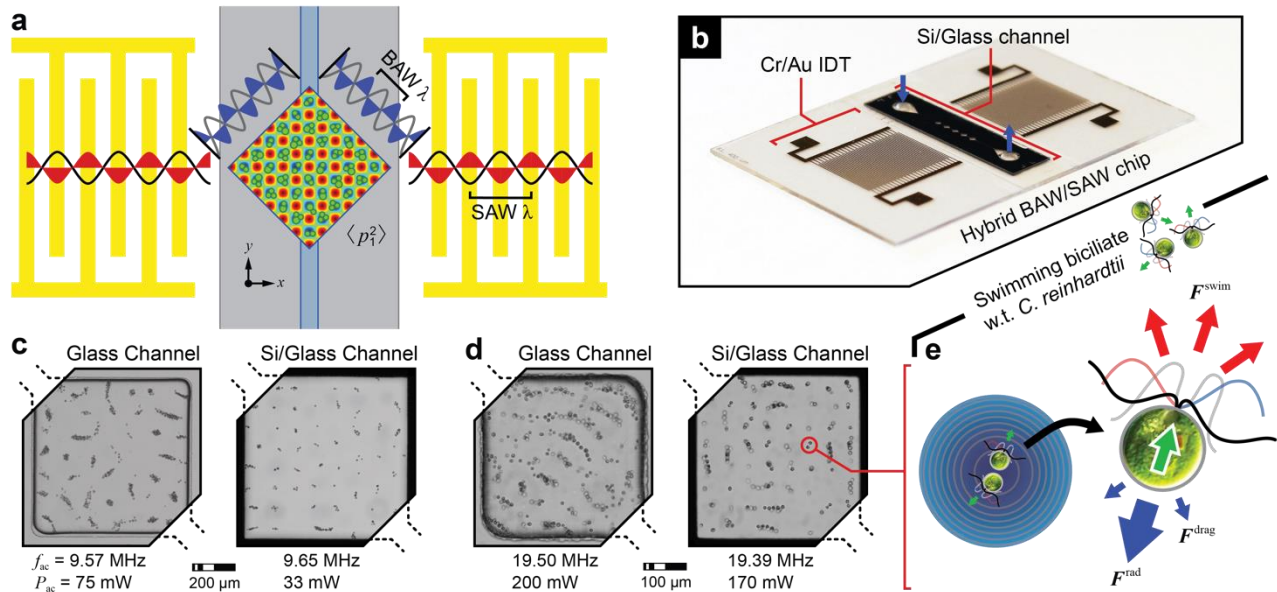


Figure 1: Hybrid BAW/SAW acoustic tweezers. (a) and (e) Illustrations of a hybrid BAW/SAW device for cell patterning and confinement to acoustic potential minima of standing BAW driven by SAW, and (b) assembled device. (c) and (d) Patterning of *C. reinhardtii* cells in glass and Si/glass chambers operating at 10 MHz and 20 MHz, respectively.

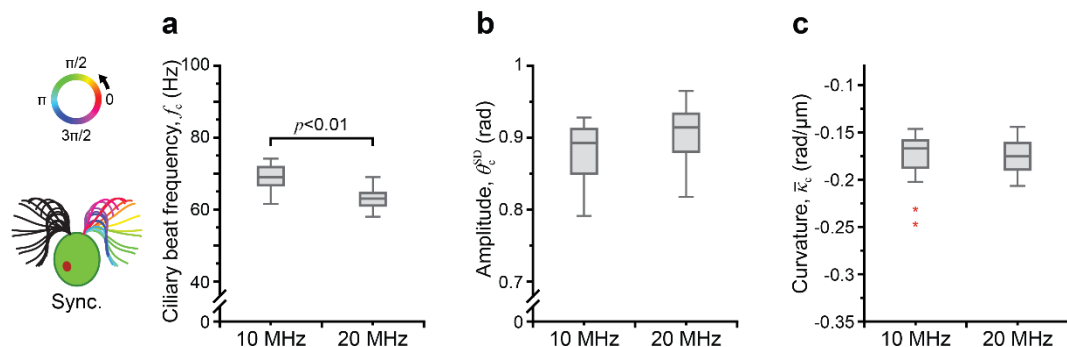


Figure 2: Cilia waveform analysis for trapped, swimming *C. reinhardtii* cells. (a)-(c) Measured beat frequency, bend amplitude, and curvature for cells trapped in 10-MHz and 20-MHz devices.

Conclusion

Compared with hybrid BAW/SAW devices employing thin glass chamber superstrates, the silicon/glass hybrid BAW/SAW devices provide better resolution of cell patterning and improved trapping efficiency. Further, the operating frequency of ultrasound used in hybrid BAW/SAW devices has negligible effects on cilia waveform for swimming CR.

Acknowledgements

This work was supported by the National Science Foundation, under Grant Nos. CMMI-1633971 and CBET-1944063. Fabrication of all devices was conducted in the Institute of Materials Science and Engineering (IMSE) cleanroom at Washington University in St. Louis. The authors thank Prof. Martin Wiklund, Karl Olofsson, and Thomas Frisk at KTH-Royal Institute of Technology for valuable microfabrication discussions.

References

- [1] M. Cui, M. Kim, P. B. Weisensee and J. M. Meacham, *Lab Chip*, 2021, **21**, 2534-2543
- [2] M. Cui, S. K. Dutcher, P. V. Bayly and J. M. Meacham, *Proc. Natl. Acad. Sci. U.S.A.*, 2023, **120**, e2218951120
- [3] M. Cui, M. Binkley, H. Shekhani, M. Berezin and J. Meacham, *Biomicrofluidics*, 2018, **12**, 034110.
- [4] M. Evander, A. Lenshof, T. Laurell and J. Nilsson, *Analytical chemistry*, 2008, **80**, 5178-5185.



Raman-acoustofluidics Spectroscopy for Red Blood Cell Analysis

Uéslen Rocha¹, Giclênio C. Silva², Marcos V. S. Sales³, Flávio O. S. D'Amato¹, Ana C. R. Leite³, and Glauber T. Silva⁴

¹Nanophotonics and Imaging Group, Institute of Physics, Federal University of Alagoas, Maceió, Brazil.

²INTACLAB–Integrated Acoustofluidics Lab Ltd., Maceió, Brazil.

Email: gicleniocavalcante@intaclab.com.br

³Bioenergetics Laboratory, Institute of Chemistry and Biotechnology, Federal University of Alagoas, Maceió, Brazil.

⁴Physical Acoustics Group, Federal University of Alagoas, Maceió, Brazil.

E-mail: gtomaz@fis.ufal.br

Introduction

Acoustofluidics comprises a set of contactless and label-free methods for acoustically manipulating cells, nano, and microparticles in microfluidic systems. Notably, the integration of acoustofluidics with Raman spectroscopy has emerged as a promising approach for the analysis of live cells [1]. In this work, we present an application of acoustofluidics in enabling Raman analysis of living human red blood cells (RBCs) within a 3D-printed chip designed as a half-wavelength multilayer resonator. We comprehensively outline the key features of the Raman-acoustofluidics method for live cell spectroscopy, including chip design, parameter matching between the chip and Raman microscope, and the intricate phenomena of acoustic radiation force and torque acting on the cells [2]. Through a series of meticulously designed experiments, we demonstrate the remarkable capability of the secondary radiation force field to create a stable and precisely organized aggregate of RBCs within the pressure nodal plane, positioned near the mid-height of the resonator. This distinctive configuration allows for precise immobilization of the RBCs, enabling prolonged Raman analysis over several hours or even days. To showcase the potential of our approach, we apply it to both a healthy population of RBCs and a pre-heated group. The latter group undergoes exposure to a heat bath at 56°C for 20 minutes prior to the Raman-acoustofluidics spectroscopy experiments. Utilizing principal component analysis (PCA) on the acquired Raman spectra, we successfully differentiate the RBC groups. By examining the ratio of two specific Raman bands, $r = I_{1588}/I_{1553}$, we verified a correlation of the 50.8% decrease of oxygen uptake in the pre-heated group as measured by a cellular respiration assay. These results highlight the potential use of acoustofluidics for improving Raman spectroscopy of live cells, particularly in the context of RBC investigation.

Methods and materials

The acoustofluidics chip (IntacLab Ltd, Brazil) used for Raman spectroscopy is illustrated in Fig. 1(a). It consists of a 3D-printed cylindrical microchamber with a height $H = 250 \mu\text{m}$ and a diameter $2R = 3.6 \text{ mm}$. The chamber is connected to two microchannels leading to an inlet and outlet. At the bottom, the microchamber is coupled to a piezoelectric actuator through a matching layer of polymeric resin. To seal the chip, a glass coverslide with a thickness $d = 150 \mu\text{m}$ is used. The actuator is excited by a low-voltage ($<5 \text{ V}$) sinusoidal signal at 3 MHz. The RBC suspension is introduced into the device via pipetting, filling the inlet. Subsequently, the acoustofluidic device is positioned on the stage of a confocal Raman microscope (LabRam HR Evolution, Horiba, France). The microscope is equipped with a synapse detector, a cooled charge-coupled device (CCD) detector, and a diode laser operating at 532 nm. The Raman laser is focused on a single RBC through a 40× objective lens with a numerical aperture (NA) of 0.65. The Raman signal, resulting from scattering, was collected using the same objective lens employed for laser focusing. The laser spot size measures approximately $3.2 \mu\text{m}$, while the axial resolution is estimated to be around $3.15 \mu\text{m}$. The irradiated power during the experiments was maintained at 0.25 mW. For each spectrum acquired, a total acquisition time of 14 seconds was utilized, with 10 seconds dedicated to accumulation. To ensure accurate calibration, the Raman setup was calibrated using the phonon band of silicon at 520 cm^{-1} as a reference. In Figure 1(b), we present the dynamic behavior of RBCs upon activation of the acoustofluidic device. The application of acoustic radiation force results in the movement of cells towards the pressure nodal plane, while the radiation torque aligns them parallel to this plane. In Figure 1(c), a digital photography of the acoustofluidic chip and a micrograph of an aggregate of aligned RBCs within the pressure nodal plane. Upon closer inspection, it becomes evident from the micrograph that certain RBCs exhibit a tilted orientation and appear to be stacked on top of each other due to limited space for optimal alignment. To address this issue and promote the formation of a monolayer of cells, we implemented solutions with a low cell concentration, approximately 200 cells/ μL .

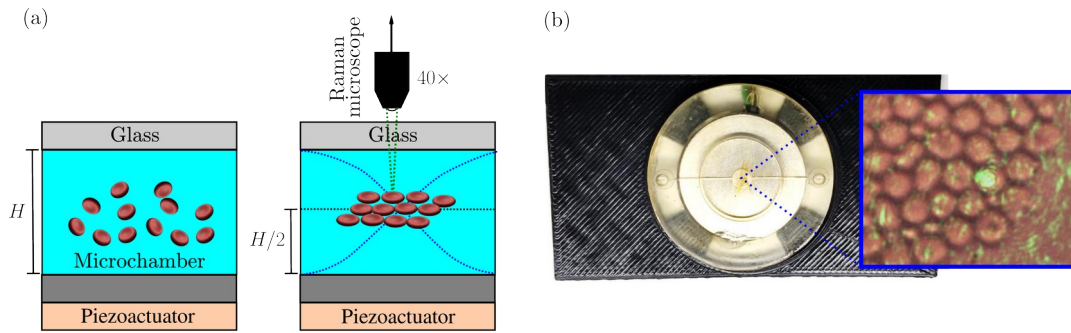


Figure 1: (a) Sketch of the Raman-acoustofluidics setting with the chip switched ‘Off’ and ‘On’. The RBCs are aligned and trapped in the pressure nodal plane (dotted line). The Raman microscope applies a 532 nm-laser on a single RBC through a 40× objective lens. (b) A digital photograph of the acoustofluidic chip. The inset corresponds to the digital micrograph of trapped RBCs showing the Raman laser (bright green spot) acting upon a single cell.

Results

The average Raman spectrum collected from both the control and pre-heated group, each consisting of a population size $n = 17$, is shown in Fig. 2(a). The spectrum obtained from the control group closely resembles previous Raman investigations of normal RBCs [3]. Additionally, the inset illustrates the examination of oxygen uptake by the cell populations. Notably, the pre-heated group exhibited a median decrease of 50.8% in oxygen uptake as measured using the Oxygraph System (Hansatech Instruments, UK). Despite the overall similarity in the Raman spectra of the control and pre-heated populations, differences can be observed in peak intensity and band position. To further analyze the ability of pre-heated Erys to bind oxygen, we examined the Raman bands I_{1588} and I_{1553} for the control and pre-heated groups, respectively, resulting in a ratio $r = I_{1588}/I_{1553}$. The control group exhibited a ratio of 3.20 ± 0.02 , while the pre-heated group displayed a ratio of 2.83 ± 0.01 . This ratio serves as a characteristic indicator of hemoglobin's affinity for ligands, particularly oxygen. The ratio of $r_{\text{heated}}/r_{\text{control}} = 0.88$ suggests a decrease in oxygen uptake by the RBCs. Principal component analysis (PCA) was conducted on the Raman spectra of normal and pre-heated RBCs. The first two principal components (PC1 and PC2) were utilized to construct two-dimensional plots. As depicted in Figure 2(b), the control population (represented by blue dots) and the pre-heated group (represented by red dots) can be easily distinguished.

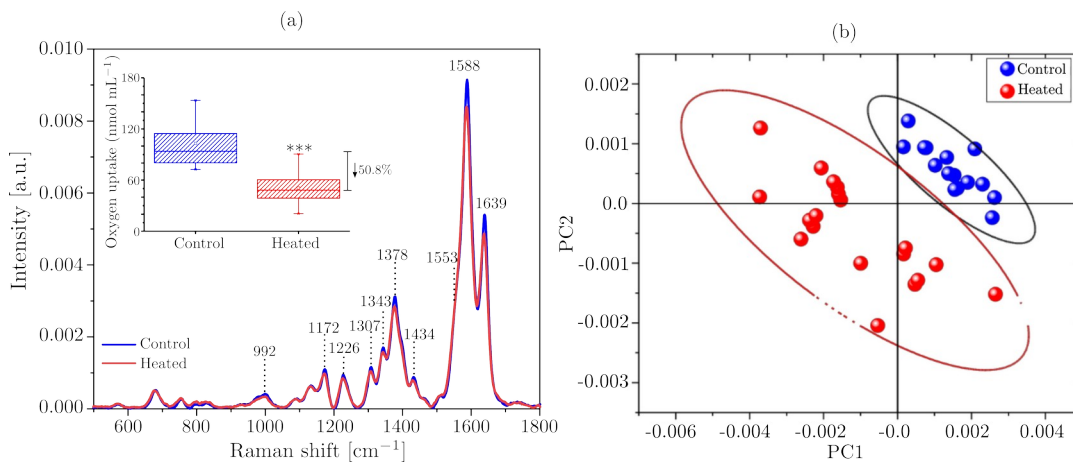


Figure 2: (a) Raman spectrum from the control (blue line) and pre-heated (red line) RBC groups. Inset: Maximal oxygen uptake capacity during 10 s, *** ($p = 0.0002$). A two-sample independent Student’s t -test was applied with a 95% confidence interval. The oxygen uptake of pre-heated RBCs (median value) decreases by 50.8%. (b) PCA scatter plot shows the discrimination of data based on control (blue dots) and pre-heated cells (red dots).

Conclusion

We successfully performed Raman analysis of live RBCs using a 3D-printed acoustofluidic resonator, eliminating substrate backscattered signals. Acoustofluidics aligned RBCs parallel to the nodal plane, enhancing Raman signal acquisition with high stability. Principal component analysis differentiated control and pre-heated RBCs, revealing biomolecular changes with a 50.8% decrease in oxygen uptake. Acoustofluidic resonators effectively support Raman investigation of live RBCs, offering potential for noninvasive disease diagnosis and treatment monitoring, improving patient care and diagnostics.

References

- [1] H. D. A. Santos *et al.*, Adv. Eng. Mat. 23, 2100552 (2021).
- [2] E. B. Lima and G. T. Silva, J. Acoust. Soc. Am. 150 (2021).
- [3] Y. Singh *et al.*, J. Biophotonics 12, e201800246 (2019).

Transient behavior and acoustic streaming effects in acoustically packed blood

Richard Soller, Ola Jakobsson, Wei Qiu, and Per Augustsson

Lund University, Department of Biomedical Engineering, Lund, Sweden

E-mail: per.augustsson@bme.lth.se, URL: <https://bme.lth.se/staff/augustsson-per/per-augustsson/>

Introduction

We have previously shown that acoustically packed red blood cells (RBCs) form a quasi-continuous medium that affects the acoustic contrast and motion of therein suspended cells and particles, and that this mechanism can be exploited to enrich rare cells from RBCs [1]. Here, we report on the transient phase of acoustic packing and relocation of cells, and we investigate the role that acoustic streaming plays in the motion and final positions of rare cells or particles inside the acoustically packed RBC bed.

Experiment overview

Whole blood was spiked with microparticle suspensions (10%_{vol}) of interest: 5- μm silica, 10- μm silica, 5- μm polystyrene (PS), 10- μm PS, 50- μm PS, and K562 cells or RBCs dyed with Calcein Deep Red AM ester. This sample was introduced in a glass-silicon-glass chip with a 375 μm \times 150 μm straight channel, actuated by a side-actuating piezoceramic transducer at the resonance frequency (Fig. 1A). The chip was imaged either from the top with an upright fluorescence microscope and z -stacks were recorded from the bottom with an inverted spinning-disk confocal microscope (Fig. 1B). The transient location of the RBC-plasma interfaces were detected in bright field images. Streaming in the cleared plasma regions was measured by defocusing-based particle tracking [2]. Transient acoustic focusing and streaming in the packed RBCs were analyzed by particle tracking (Fig. 1C) and particle image velocimetry.

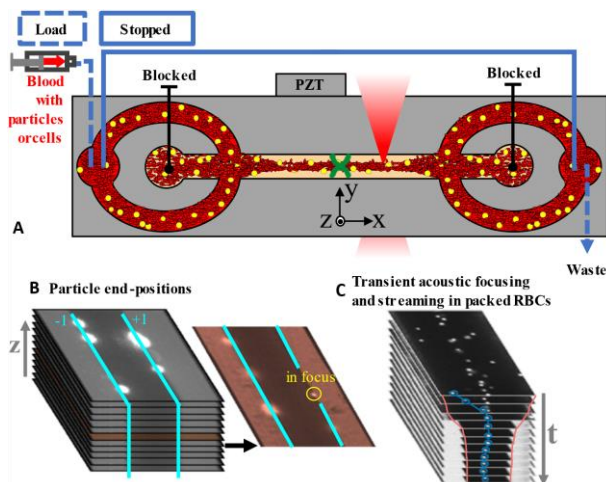


Figure 1: Chip and measurement. Blood is injected, flow is stopped, and sound is activated (A). After ~ 30 s the locations of fluorescently labeled cells and particles are identified in images at different depths (B). To characterize acoustic streaming tracer particles were added and analyzed by defocusing-based particle tracking for a sequence of images.

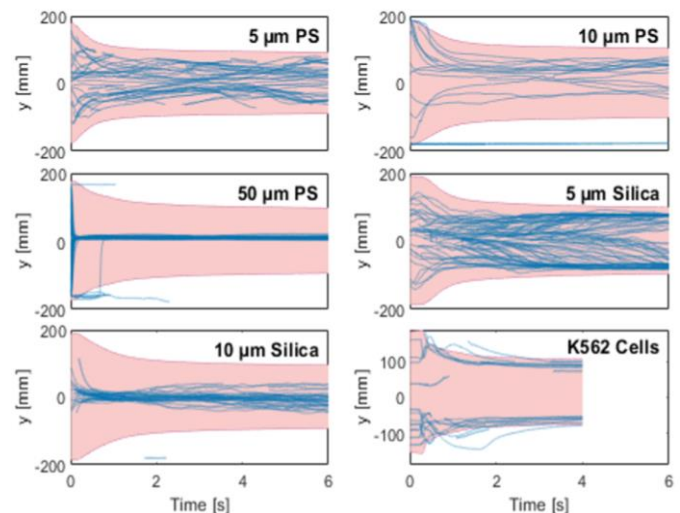


Figure 2: Transient acoustic focusing. Blood is injected, flow is stopped, and sound is activated. Particles or cells (blue) and the RBC/plasma interface (red) are tracked.

Results

All studied cells and microparticles have positive acoustic contrast factors in plasma, but K562 cells have a negative contrast factor in packed RBCs. In the transient phase of acoustic packing, particles and RBCs move, at different, velocities towards the channel center (Fig. 2). As the RBCs become packed, smaller particles appear to become ‘unfocused’, likely due to acoustic streaming. K562 cells initially also move slightly towards the center but as the packing of the RBCs increases, they are pushed to the vicinity of the RBC-plasma interface and some are even temporarily pushed out in the plasma region by the plasma stream.

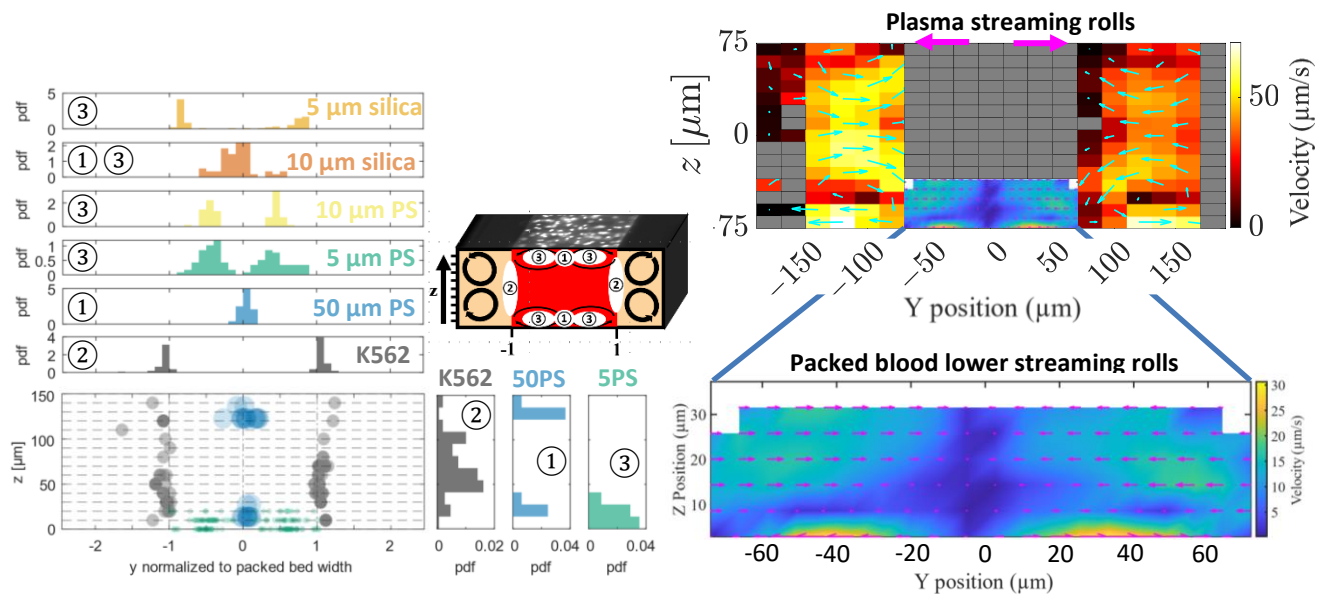


Figure 3: Quasi-stationary positions that particles and cells reach after the transient phase. Particles settle at 3 different positions, depending on their size and acoustic contrast factor. 5- μm -PS data only from imaging from the bottom.

Figure 4: Acoustic streaming in packed RBCs and plasma. Streaming rolls in plasma were tracked with 1.1 μm PS particles and GDPT. In the packed RBCs, labeled RBCs were tracked at different z-levels with a confocal microscope. Arrows at top indicate streaming direction as seen in upright fluorescence microscope.

The final locations of cells and microparticles after prolonged exposure to sound are shown in **Fig. 3**. K562 cells end up at the RBC/plasma interface (positions ②). Larger particles, particularly those with high acoustic contrast factors such as 50- μm -PS and 10- μm -silica particles, settle in the central pressure node at the top and bottom of the channel (positions ①). Smaller particles (10 μm PS, 5 μm PS, 5 μm silica) localize between the central pressure node and the RBC/plasma interfaces and at the top and bottom of the channel (positions ③). 5 μm PS particles form streaming rolls near the center at the top and bottom, but not across the whole packed RBC bed height which indicates that acoustic streaming is present inside the packed RBCs. To assess the presence of acoustic streaming, we imaged packed blood with spiked-in fluorescently labeled RBCs. Four flat streaming rolls were observed in the packed blood region with the highest streaming velocities at the upper and lower channel walls (**Fig. 4**) and a steep decline and sign reversal of the streaming velocity just $\sim 5 \mu\text{m}$ away from the boundaries. There were also two streaming rolls in each of the plasma regions with sign reversal $\sim 15 \mu\text{m}$ away from the boundaries. The plasma streaming rolls rotated faster and in the same direction as the neighboring RBC streaming roll.

Discussion

As K562 cells have a positive contrast factor in plasma and a negative one in packed RBCs, they move inwards till their contrast factor in the denser packed blood changes. Then they are transported to the RBC/plasma interface, by radiation force, aided by streaming, where they are dragged to the mid-height of the channel by the more viscous RBCs and remain there. Particles that have a high enough acoustic impedance and are big enough (50 μm PS, 10 μm silica) have a radiation force that everywhere in the channel is greater than the drag force. This will keep the particles at the pressure node in the middle of the channel. Streaming eventually moves them to the top and bottom. Particles with a smaller acoustic radiation force acting on them (10 μm and 5 μm PS, 5 μm silica) are stronger influenced by acoustic streaming and will partially follow the streaming rolls. They settle at a characteristic equilibrium position at the top/bottom wall and between the central pressure node and the RBC/plasma interface, where the radiation force equals the drag force from streaming. We propose that the driving mechanism for streaming is the same as for 4-roll boundary-driven Rayleigh streaming in a homogeneous medium, but the presence of 8 streaming rolls was unexpected. This indicates that packed RBCs and plasma behave as separate compartments across which streaming cannot recirculate in the bulk, attributed to strong stabilizing acoustic body forces at the interface. We propose that the highly confined streaming rolls in the packed RBCs may be attributed to either a shear thinning effect or stabilizing acoustic body forces due to a gradually increasing RBC concentration towards the pressure node.

References

- [3] R. Soller, O. Jakobsson, P. Augustsson. Procs. pp. 85-86, Acoustofluidics 2021, 26 - 27 August 2021.
 [2] R. Barnkob, M. Rossi, C. Kähler. Lab on a Chip, 15.17 (2015): 3556-3560.

Acoustofluidic shape-based separation of microparticles and cells by acoustic radiation force and torque

Muhammad Soban Khan¹, Mushtaq Ali¹ and Jinsoo Park¹

¹Department of Mechanical Engineering, Chonnam National University, Gwangju, Korea
E-mail: jinsoopark@jnu.ac.kr

Introduction

The ability to continuously separate particles and cells without labeling is crucial in various chemical and biomedical applications. However, most microfluidic approaches have been limited to manipulating particles and cells based only on their size, even though particle shape is a significant factor in defining particle attributes and behavior. In addition, most of the previous techniques faced challenges such as the requirement of labels, labor-intensive and time-consuming. Shape-based separation has attracted interest because of their potential applications in various biomedical and chemical assays. Despite the demand, there has been only a few studies on microfluidic micro-objects separation based on their shape

Here, we suggest on-demand, label-free acoustofluidic separation of prolate ellipsoidal and spherical microparticles based on travelling surface acoustic wave (TSAW)-induced acoustic radiation force (ARF) and torque (ART). For elucidation of the underlying physics, we conducted numerical simulation of the wave scattering of spherical and prolate objects. For validation, we performed a series of separation experiments with polystyrene microspheres, prolate ellipsoids, peanut-shaped microparticles and T.Eccentrica. From quantitative analysis of the separation efficiency, we confirmed high purity and high recovery rate of the proposed acoustofluidic shape-based separation of micro-objects.

Methodology

The proposed acoustofluidic device, depicted in Figure 1(a) consists of slanted-finger interdigital transducer (SFIT) placed on a piezoelectric lithium niobate (LiNbO₃) substrate with a polydimethylsiloxane (PDMS) microchannel placed on top of a substrate.[1] Figure 1(b) provides a top view of the midstream microchannel, where (red) spherical particles and (blue) prolate particles made of polystyrene (PS) are present in the fluid flow. The purpose of our study was to demonstrate the separation of micro-objects based on their shape rather than their size. To achieve this, we produced prolate particles with the same volume as the spherical PS particles by stretching the spherical particles uniaxially. In the presence of the acoustic field, the spherical particles experience an acoustic radiation force (ARF) caused by the scattering of the inhomogeneous wave off them. However, prolate particles align themselves with their major axis parallel to the propagation of the acoustic wave, instead of rotating like the spherical particles. This alignment of prolate particles is due to the combined effect of the TSAW-induced acoustic radiation torque (ART) and ARF. Unlike spherical particles, the rotation of the prolate particles leads to asymmetric wave scattering, resulting in counter-rotating forces. Clockwise or counter-clockwise rotational forces act on the prolate particles until symmetric wave scattering occurs, aligning their major axis with the wave propagation direction. The specific alignment of the prolate particles reduces their projected surface area for acoustic wave scattering compared to the spherical particles. In particular, a decrease in backscattering leads to a reduction in ARF, which is the primary force driving lateral migration of objects in the direction of wave propagation. As a result, the spherical and prolate particles

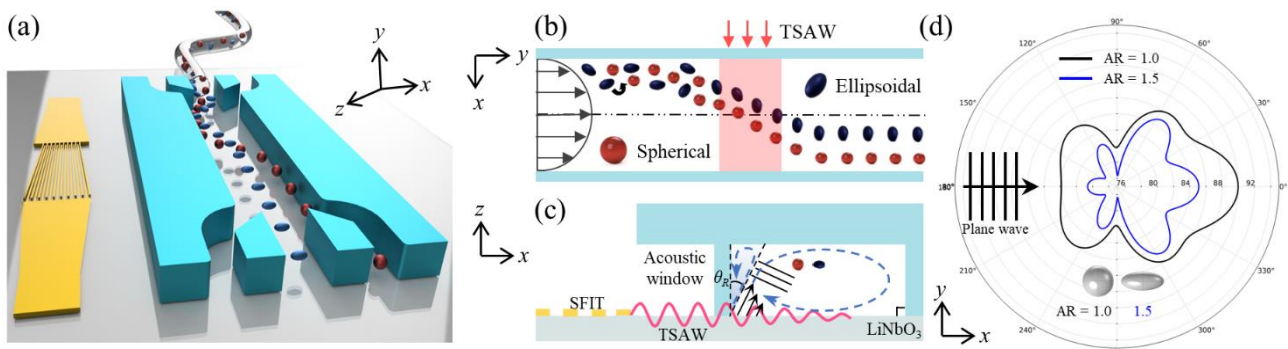


Figure 1: a) A schematic diagram of the proposed acoustofluidic device. b) Top view of the midstream microchannel. c) Cross-sectional view of the midstream microchannel. d) Polar scattering plots from numerical simulation of wave scattering off spherical and prolate ellipsoids showing Wave scattering off spherical (black) and prolate with aspect ratio of 1.5 (blue).

are separated, as shown in the cross-sectional view of Figure 1(c). It should be noted that a microchannel anechoic corner (MAC) region, formed by the refraction of the longitudinal wave at the Rayleigh angle θ_R , is present at the top-left corner of the microchannel, as previously reported[2]. Figure 1(d) describes the acoustic pressure level in the external field for the microspheres (black) and their derivative prolate microparticles with aspect ratio of 1.5 (blue) of the same volume as the microspheres. The incident waves were assumed to be plane progressive waves propagating from left (180°) to right (0°) in the x-direction.

Results and Discussion

Figure 2(a) demonstrates the trajectories of the $5\ \mu\text{m}$ spheres and $6.75 \times 4.5\ \mu\text{m}$ (AR = 1.5) prolate ellipsoids, with the 141 MHz TSAWs at 6.58 mW, respectively. With reference to the lateral migration of the $5\ \mu\text{m}$ microspheres, the ellipsoidal microparticles showed reduced lateral migration. Figure 2(b) shows the deflection of the non-spherical bio-object *Thalassiosira eccentrica* which is a microalgae who are cylindrical in shape with a radius of $17\ \mu\text{m}$ and height of $32\ \mu\text{m}$. Figure 2(c–f) shows the results of acoustofluidic separation of the $7.7 \times 5.1\ \mu\text{m}$ peanut-shaped particles from the $6\ \mu\text{m}$ spherical particles using the 117 MHz TSAWs (Helmholtz number of 1.5) at 6 mW. Figure 2(c) shows the stacked microscopic images in the midstream microchannel. The trajectories of the $7.7 \times 5.1\ \mu\text{m}$ peanut-shaped particles were found to be distinct from those of the $6\ \mu\text{m}$ spherical particles. Despite the morphological difference, the peanut-shaped particles could be approximated as prolate ellipsoids of AR = 1.5. Figure 2(d) shows the mixture of the $7.7 \times 5.1\ \mu\text{m}$ peanut-shaped and $6\ \mu\text{m}$ spherical particles collected from Outlet 1 without the acoustic field. Fig. 2(e and f) show the collected particles after acoustofluidic shape-based separation from Outlet 2 and Outlet 3, respectively. In Figure 2(e), most microparticles were found to be peanut-shaped particles due to their smaller lateral migration. On the contrary, in Figure 2(f), most of the collected particles were verified as microspheres since they experienced the TSAW-induced ARF with greater magnitude compared to the non-spherical particles. Figure 2(g) show the purity and recovery rate for $6\ \mu\text{m}$ spherical (red) and the $7.7 \times 5.1\ \mu\text{m}$ peanut-shaped (blue) particles, respectively. The purity and recovery rate of the $6\ \mu\text{m}$ spherical particles were 100% purity and 96.7% recovery rate, while the $7.7 \times 5.1\ \mu\text{m}$ peanut-shaped particles exhibited purity of 95.3% and recovery rate of 100%.

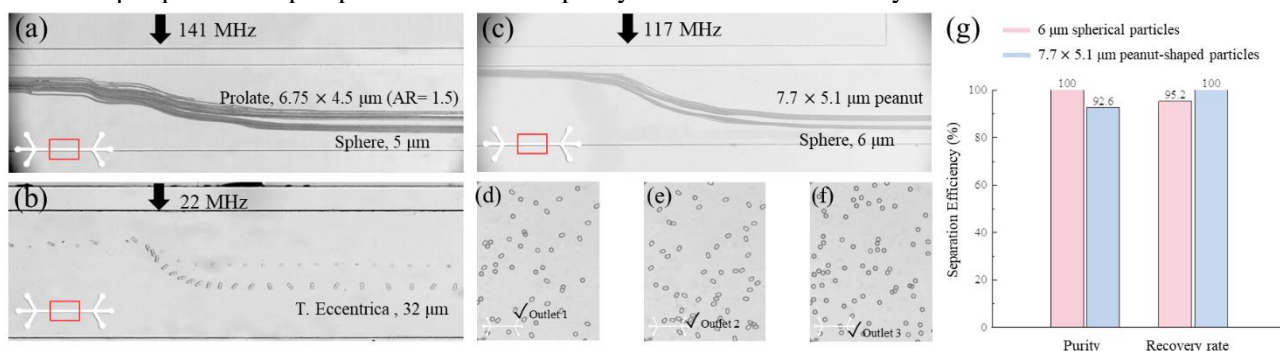


Figure 2: Microscopic images of acoustofluidic shape-based separation of spherical and ellipsoidal PS microparticles. a) $5\ \mu\text{m}$ spherical and $6.75 \times 4.5\ \mu\text{m}$ (AR = 1.5) prolate particles with the 141 MHz acoustic field. b) Microalgae with a radius of $17\ \mu\text{m}$ and height of $32\ \mu\text{m}$ with the 22 MHz acoustic field. c) $6\ \mu\text{m}$ spherical and $7.7 \times 5.1\ \mu\text{m}$ peanut-shaped microparticles with the 117 MHz acoustic field in the midstream. d–f) Collected particles from Outlet 1, 2 and 3. g) Illustrates the efficiencies of separation via purity and recovery rate at the outlets.

Conclusion

We proposed a method for separating spherical and prolate micro-objects based on their shape using acoustofluidics. The prolate ellipsoidal PS microparticles were created by stretching seed microspheres in one direction. Through numerical simulations of wave scattering off spherical and prolate ellipsoids, we discovered that the asymmetrical wave scattering caused a counter-rotating radiation torque on the rotating prolate objects, aligning them such that their major axis was parallel to the progressive wave propagation. Using the proposed acoustofluidic method, we successfully separated spherical and prolate PS microparticles, as well as spherical and peanut-shaped PS microparticles of the same volume. Our quantitative analysis of the separation efficiency confirmed a high purity and recovery rate for the separated spherical and peanut-shaped PS microparticles using this acoustofluidic approach.

Acknowledgements

This work was supported by the National Research Foundation of Korea (NRF) grants funded by the Korea government (MSIT) (Nos. 2020R1A5A8018367 and RS-2023-00210891).

References

1. Ali, M. and J. Park, *Ultrasonic surface acoustic wave-assisted separation of microscale droplets with varying acoustic impedance*. Ultrasonics Sonochemistry, 2023. **93**: p. 106305.
2. Khan, M.S., et al., *Residue-free acoustofluidic manipulation of microparticles via removal of microchannel anechoic corner*. Ultrasonics Sonochemistry, 2022. **89**: p. 106161.

Ultrasonic single-beam manipulation of particles and organoids through a petri-dish and a plastic tube using an acoustic field live-visualisation method

Mario Ortega-Sandoval¹, Krishna Coimbatore Barlam¹, Luke Cox¹, Martha Lavelle², James Armstrong², and Bruce Drinkwater¹

¹Faculty of Engineering, University of Bristol, Bristol BS8 1TR, UK
E-mail: mario.ortegasandoval@bristol.ac.uk

²Department of Translational Health Sciences, University of Bristol, Bristol, BS1 3NY, UK

Introduction

Acoustic manipulation has been used to manipulate particles such as cells, cellulose, and spherical particles underwater in 2D by using surface acoustic waves (SAW) [1] and in 3D using bulk waves in the form of twin-traps [2] and vortex traps [3]. In this work we demonstrate three-dimensional underwater manipulation of particles and cell clusters within a petri dish and a plastic tube. We describe a method to visualize in real-time the acoustic field in which a contained layer of small, high-density particles, allows the trap to be seen in the same image as the particle. As a result, this device has the potential to be implemented in a variety of applications such as non-invasive medical interventions, microorganism manipulation, intra-venous manipulation, and drug delivery.

Materials and methods

The experimental set up is shown in Figure 1 a) which shows a PCB that was designed to allow the attachment of piezoelectric discs to solder-pads using a conductive epoxy adhesive (8331D, MG Chemicals, Canada). The piezoelectric transducers (PZT-5, Beijing Ultrasonic, China) had a resonant frequency at 1.76 MHz, with a thickness of 1.1 mm, and a diameter of 20 mm. The initially circular piezoelectric transducer was split into two equal half-circled pieces and covered with a silver wraparound electrode. A Fresnel-lens of a focal length of 20 mm was printed in a 3D printer (Formlabs 2, Formlabs, USA) using a transparent resin (Clear FLGPCL02, Formlabs, USA). The lens was then glued to the piezoelectric transducer elements with an epoxy glue (Gorilla epoxy 25 ml, Gorilla Glue, USA). The transducer elements were then connected to a signal generator (Keysight 33110A, Agilent technologies, USA) via an amplifier (75A250A, Amplifier Research, USA) and excited with a sinewave. The transducer elements were connected in to produce a 180-degree phase difference between them, which allowed the generation of a twin trap.

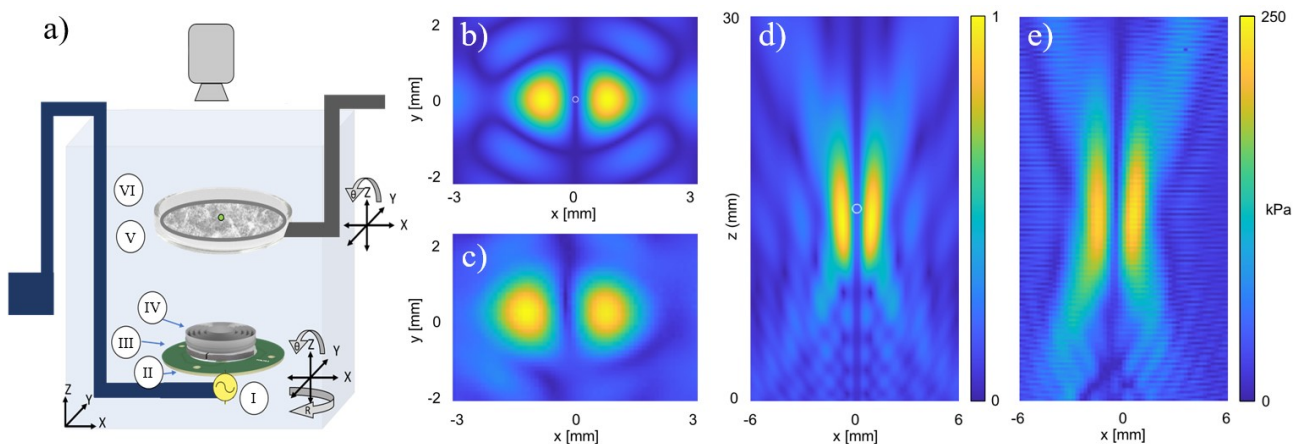


Figure 1: Experimental setup and acoustic pressure fields. a) shows the experiment setup which consists of an electrical connection (I), a PCB board (II) conducting adhesive (III) and Fresnel lens (IV). A cantilever moves the transducer in 3-axes. (V) shows a petri dish attached to a holder below which is the visualisation layer (VI). A camera was positioned above the petri dish. b), c) Huygens' model pressure map in the x-y axis and the x-z axis respectively. c), d) Experimentally measured hydrophone pressure maps.

The acoustic pressure was measured as 238 kPa at the pressure maximum of the twin-trap (fibre optic hydrophone, model FOHS71, Precision Acoustics, UK). A force balance [4] can be performed against flow as performed: $m_p dv(x)/dt = F_s + F_{AM} + F_{ARF}$, where m_p is particle mass, $v(x)$ is the flow speed, F_s is Stokes' drag, F_{AM} is the added mass force due to the displaced fluid and F_x is the acoustic radiation force. The drive voltage was adjusted until the radiation force was just able to hold the particle steady against the flow. At this point the inertia can be neglected and so $-F_{ARF} = F_s$. Stokes' drag was found from $F_s = 6\pi\mu rU$, [5], where r is the radius of the particle, μ is the dynamic viscosity of water and U is the relative velocity between the particle and the fluid. Hence the radiation force was found to be 0.38 μN for this excitation level (14Vpp).

A range of Rayleigh sized particles ($\lambda/4 - \lambda/10$) were manipulated over distances of a few millimetres. The visualisation layer was attached below the petri dish and consisted of a flat container manufactured from acetate sheets filled with a mica particle solution in water. The mica particles allowed visualisation of the high-pressure regions of the twin-trap simultaneously with imaging the manipulated object.

Results

The pressure field was simulated Figure 1 b) and d) and then confirmed with a fibre optic hydrophone in Figure 1 c) and e). When the device was turned on, the twin trap was positioned with help of the visualisation layer such that it trapped the particle. As an example, a 130 μm polyethylene particle was manipulated in 3D as shown in Figure 2 a)-c). In a further 3D example, a 130 μm polyethylene particle was extracted from a 2 mm diameter, 0.5 mm wall-thickness plastic tube d). Finally, a 920 μm diameter fixed immature brain organoid was manipulated within a 0.65 mm thickness petri dish in the horizontal 2D plane e).

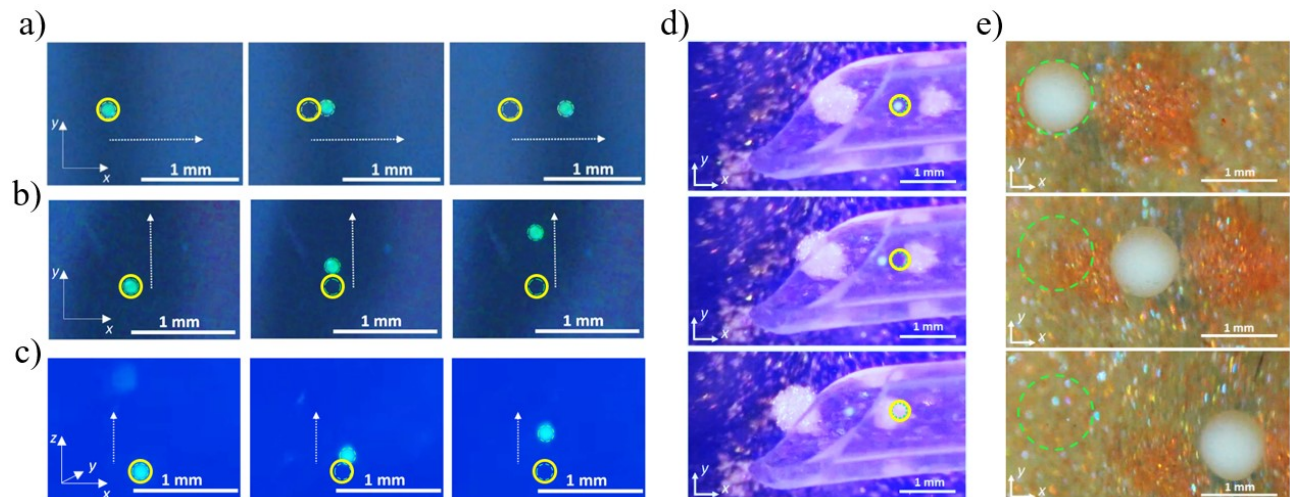


Figure 2: Particle manipulation and applications. 3-axis acoustic manipulation of a single 130 μm particle. Displacement of a 130-micron polyethylene particle in the x-axis direction (a), in the y-axis direction (b) and in the z-axis direction (c). d) Manipulation of a 130-micron polyethylene particle inside a plastic tube, the time from the initial position to the final position is 0.3 seconds. e) Manipulation of a 920 μm diameter fixed immature brain organoid. The total time from the initial to the final position is 18 seconds.

Conclusion

Hydrophone pressure measurements of Figure 1 c) and e) showed that the single-beam device produced a twin trap. The experimental results of Figure 2 show that the device can manipulate particles in the three dimensions and through obstacles such as a petri dish and a plastic tube. The design of this single-beam device is simple in terms electronics and can be manufactured using low-cost components. The design is also scalable in terms of size and frequency. This low-cost and compact implementation of 3D manipulation is potentially suitable for applications such as non-invasive medical interventions, microorganism manipulation, intra-venous manipulation, and drug delivery.

References

- [1] J. Shi, X. Mao, D. Ahmed, A. Colletti, and T. J. Huang. Lab Chip 8, 221–223 (2008).
- [2] A. Franklin, A. Marzo, R. Malkin, and B. W. Drinkwater. Applied Physics Letters 111, 094101 (2017).
- [3] Li, J., Crivoi, A., Peng, X. et al. Commun Phys 4, 113 (2021).
- [4] D. Baresch, J.-L. Thomas, and R. Marchiano. PhysRevLett. (2016).
- [5] P. Glynne-Jones and M. Hill. Lab Chip, vol. 13, no. 6, pp. 1003–1010. (2013).

Electromechanical resonance in electrical double layers driven by MHz-frequency surface acoustic wave

Sudeepthi Aremanda¹ and Ofer Manor¹

¹The Wolfson Faculty of Chemical Engineering, Technion-Israel Institute of Technology, Haifa, Israel.
E-mail: asudeepthi@campus.technion.ac.il, URL: <https://chemeng.technion.ac.il/small-scale-transport-research-laboratory/>

Introduction

We employ for the first time a MHz-frequency mechanical vibration, i.e., a Rayleigh type surface acoustic wave (SAW) in a solid substrate, to dynamically excite an electrical double layer of ions (EDL) in a neighboring electrolyte solution.

The EDL, to appear next to charged surfaces in electrolyte solutions, is an electrical surface phenomenon in which an artificially or naturally charged surface in an electrolyte solution attracts a cloud of ions that introduce osmotic and electrical effects in its vicinity. The EDL is fundamental across countless natural and artificial systems and may considerably vary in properties between one system to another. Its applications range from supporting electrophoresis and electro-wetting to governing the kinetics of particulate coagulation, folding structures of proteins, surface properties of membranes, and particulate adsorption onto an underlying substrate. The generic nature of the EDL and the interplay between physical mechanisms therein alongside its short length scales of usually several nanometers and a relaxation time scale of nano- to micro-seconds render the EDL and the interplay between its different subcomponents an enigma, even now more than a century since it was discovered. A previous theoretical work predicts that electrical field leakage off a SAW excited EDL is measurable and may highlight the internal properties of the EDL [1].

We present here an experimental approach to measure the electrical field leakage off an EDL under SAW excitation. We show that the measured electrical field leakage corresponds to an array of mechanical-electrical responses therein which gives direct insights about dynamical effects in EDLs. We observe that periodic motion of ions in the EDL under SAW excitation results in resonance effects in the excited EDL akin to resonance in an equivalent RLC electronic circuit.

Experimental details

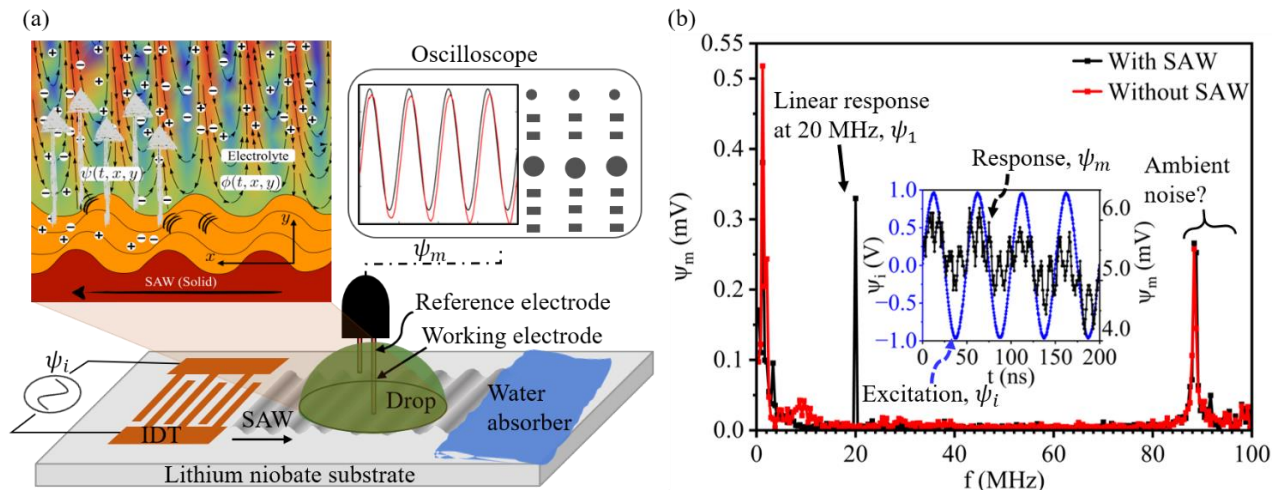


Figure 1: (a) Schematic of the experimental setup including an illustration of the physics in the drop near the SAW excited solid surface, where ψ and ϕ are the voltage and acoustic flow stream function field, respectively. (b) FFT of the electrical potential leakage in NaNO_3 solution with (black line) and without (red line) the SAW-excitation.

Fig. 1a. shows the schematic of the experimental setup and an illustration of the ion movement in the EDL under SAW excitation. We excite a sessile drop of an electrolyte solution atop a solid substrate using a traveling SAW at 20 MHz frequency. The SAW vibrates the ions in the EDL, emanating from the flat solid into the solution and dynamically distorts the equilibrium ordering of ions, leading to the leakage of a measurable electrical voltage, ψ_m away from the EDL. We measure the voltage leakage ψ_m at a separation of 40 microns

away from the solid surface using a working electrode against a reference electrode in the bulk of the drop (1 millimeter away from the solid). The electrodes are connected to an oscilloscope for obtaining frequency variation and to a lock-in amplifier for measuring the 20 MHz-frequency component of the electrical leakage (ψ_1), i.e., the linear (same frequency) response of the EDL to the exciting SAW. Fig. 1b shows the fast Fourier transform (FFT) of the electrical potential leakage in a drop of 1.5×10^{-3} Molar NaNO₃ solution in the presence (black line) and absence (red line) of SAW. The 20 MHz FFT peak gives the linear response, ψ_1 , of the EDL to SAW excitation. In the inset, we show the original voltage signal, ψ_i applied to the piezoelectric actuator and the measured total EDL response, ψ_m .

Results and discussion

In Fig. 2 we demonstrate ionic strength (I) variations of electric potential leakage magnitude, $|\psi_1|$, and phase difference, $\Delta\theta$ in sodium nitrate (NaNO₃) and potassium chloride (KCl) solutions. The phase difference $\Delta\theta$ is the difference of signal phase measured in the drop and in air (in the absence of a drop), keeping the rest of the parameters the same. In the same figure, we further show variations of the same parameters with the time ratio, $t_r(m^+)$, the ratio between the acoustic time (ω^{-1}) and the relaxation time (the characteristic time at which sodium ions attain equilibrium distribution given by $\sigma^2/D(i)$, where σ is the Debye length and $D(i)$ is the diffusion coefficient of the ion ' i ') of the positive ions in the EDL (m^+) in two different electrolyte solutions. We observe that $|\psi_1|$ is maximized and $\Delta\theta$ is minimized when the SAW acoustic time is the same as the positive (m^+) or negative (m^-) ion relaxation time, i.e., $t_r(m^+) = 1$ and $t_r(m^-) = 1$, respectively. Since $t_r(m^-)/t_r(m^+) = D(m^+)/D(m^-)$, we observe in the different sub-figures a $|\psi_1|$ maximum near $t_r(m^+) = 1$ and a second maximum shifted on the $t_r(m^+)$ axis in a manner proportional to the diffusion coefficient ratio, $D(m^+)/D(m^-)$, i.e., near $t_r(m^-) = t_r(m^+) \times [D(m^+)/D(m^-)] = 1$. We further observe higher harmonics of the above mentioned “zero order” $|\psi_1|$ maxima at near integer multiplications of $t_r(m^+)$ and $t_r(m^-)$. These events are reminiscent of electrical impedance decrease and signal phase minimization is an RLC circuit near resonance, and may be employed to obtain electronic circuit equivalent of dynamic EDL response. It is apparent that the peaks are distinctive of the type of ions and their concentration in the electrolyte- which may be used to characterize the electrolyte solutions.

At $t_r(m^+) = 1$ and $t_r(m^-) = 1$, the SAW disturbance of ions and their relaxation toward an equilibrium EDL are correlated in time: The path-length of ion vibration is maximized, becoming comparable to the EDL's Debye length and resulting in a local decrease in the EDL electrical field screening efficiency and thus, in a local measured maximum in the electrical leakage off the EDL. A byproduct of this finding is that one may obtain the concentration of an electrolyte solution by evaluating the Debye length, σ , from the measured path-length of ion vibration, as Debye length is expressed in terms of solution ionic strength (I) [1].

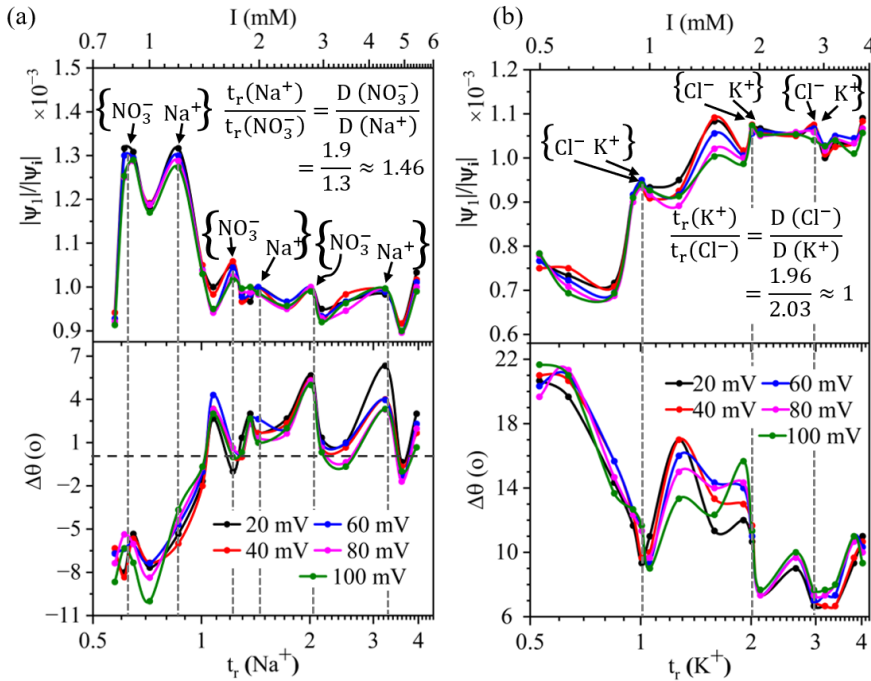


Figure 2: Magnitude of the scaled electrical potential leakage (ψ_1) and phase difference between the excitation SAW signal and ψ_1 plotted against ionic strength (I) and t_r for (a) NaNO₃, (b) KCl at various power levels (at the voltages indicated in the legend) of SAW-excitation.

Conclusion

We experimentally measured the electric field leakage past a SAW excited EDL. We observed that EDLs undergo electro-mechanical resonance under SAW excitation akin to the resonance in electronic RLC circuits which may be employed to obtain electronic circuit equivalent of EDL's dynamic response. The ion-specific electrical leakage spectrum translates to ‘fingerprints’ of the ionic mixture and concentration which can be used as new spectroscopic approach for the characterization of electrolyte solutions.

References

[1] O. Dubrovsky and O. Manor. Langmuir **12**, 37(50), 14679–14687452 (2021).

Acoustophoresis enriches tumor cell clusters in blood of patients with prostate cancer

Cecilia Magnusson¹, Per Augustsson¹, Eva Undvall Anand¹, Andreas Lenshof¹, Andreas Josefsson^{2,3}, Karin Welén², Anders Bjartell¹, Yvonne Ceder¹, Hans Lilja^{1,4}, Thomas Laurell¹

¹Lund University, Sweden

E-mail: per.augustsson@bme.lth.se

URL: <https://bme.lth.se/research-pages/nanobiotechnology-and-lab-on-a-chip/>

²Gothenburg university, Sweden

³Umeå University, Sweden

⁴Memorial Sloan-Kettering Cancer Center, NY, United States.

Introduction

We evaluated acoustophoresis to enrich circulating tumor cells (CTC) in blood from 12 patients with metastatic prostate cancer and from 20 healthy control samples. In patients, both singlets and clusters of CTCs were found as well as aggregates of CTCs and white blood cells (WBC). Further, CTCs were found in patients where the gold standard CellSearch did not. A protocol for cell fixation was developed that enables a largely unchanged ability to separate prostate cancer cells from WBC after 3 days of storage. We believe this is to date the most comprehensive evaluation of acoustic separation of CTCs in patients and healthy control subjects.

Background

CTCs are shed from the primary tumor or metastatic lesions into the systemic blood circulation. Prior reports have established that high CTC counts are associated with adverse outcome and lower overall survival in metastatic cancers [1]. The FDA approved CellSearch assay is considered as the current gold standard and is based on magnetic bead antibody capture but is unable to find cells that have low expression of the surface molecule EpCAM. Therefore, there is an important unmet clinical need to develop complementary approaches that exploits alternative cell properties to isolate CTCs [2].

Experiment

We collected 6 ml blood from 12 patients with advanced prostate cancer. Red blood cells (RBC) were chemically lysed and paraformaldehyde was used to fix remaining cells (WBCs + CTCs). Cells were diluted and separated by acoustophoresis and analyzed by imaging flow cytometry. The approach, illustrated in **figure 1**, is based on the notion that CTCs, and in particular clusters thereof, migrate faster than WBCs when exposed to sound [3-5].

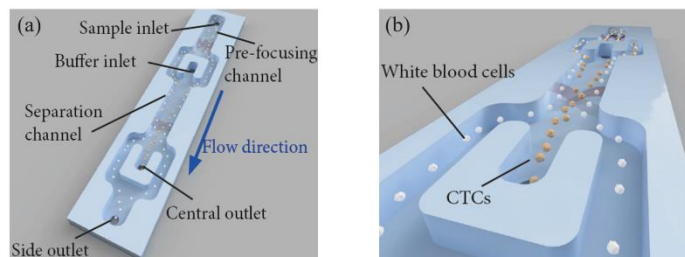


Figure 1: (a) Key features of acoustic pre-focusing and separation of cells. (b) Focused CTCs and CTC clusters exit through the central outlet while WBCs exit through the sides.

Results

For cell-line cells spiked in blood, >99.5% of WBCs can be removed while recovering >95% of cancer cells, **figure 2**. Stability during storage is critical to enable transfer of clinical samples. Over three days after paraformaldehyde fixation, the ability to discriminate cancer cells from WBCs drops only slightly, **figure 3**.

High cancer cell recovery and good WBC discrimination

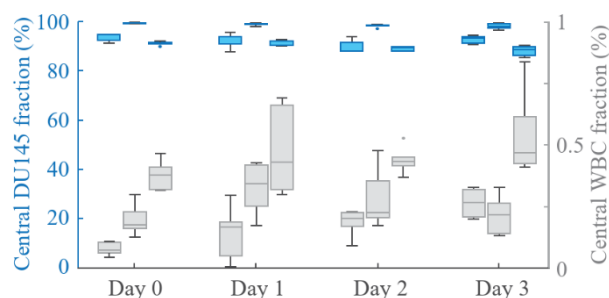


Figure 2: Separation performance for prostate cancer cell line DU145 mixed with WBCs from healthy donors vs storage time after fixation. Each box represents six technical repeats (n=6). Horizontal line in each box represents the median, top and bottom edges are the upper and lower quartiles, whiskers indicate non-outlier minimum and maximum, and dots indicates values outside 1.5 times the interquartile range.

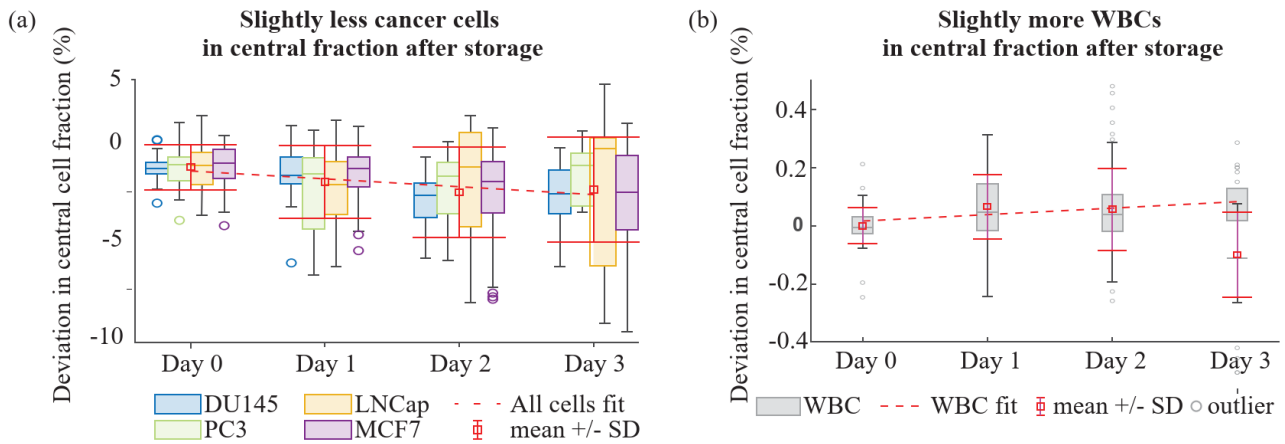


Figure 3: Trend analysis of the deviation in central outlet cell fraction compared to day 0 for increasing storage time after fixation for (a) four different cell lines and (b) WBCs. Dashed red lines represent linear fits of the change in the central fraction for all cells and red squares and whiskers represent mean and SD for each storage time. In (a) $n=18$ samples were analyzed for each box. In (b) $n = 72$ for each box.

We found higher number of cells with CTC-antigen characteristics (EpCAM+, PanCK+, CD45-/CD66b-, DAPI+) in the central (*i.e.* cancer cell) outlet after acoustophoresis both in blood from patients and in healthy subjects, compared to CellSearch, **Figure 4(a)**, [6]. Cancer cell sizes were found to be on average slightly larger than that of contaminating WBCs in the cancer cell outlet, **Figure 4(b)**. Clusters containing two or more CTCs, or combinations of CTCs and WBCs, were found at a much higher frequency in patients with metastatic prostate cancer than in healthy subjects, **Figure 4(c)**, while no clusters were found with CellSearch.

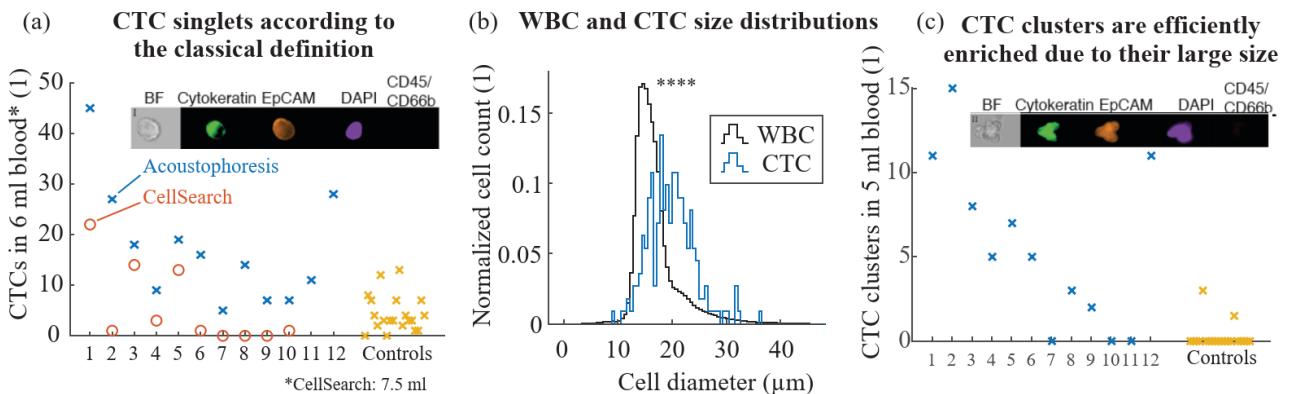


Figure 4: (a) Cells that fulfill the classical definition for CTCs are found in patients. (b) Size distribution of patient CTCs and contaminating WBCs after enrichment (pooled). (c) Clusters are common in patients but very rare in healthy subjects.

Conclusions

Our acoustic CTC-enrichment data from patients with metastatic prostate cancer and healthy control subjects suggest that it is a viable alternative or complement to antibody-antigen capture due to high analytical sensitivity and its ability to detect and enrich CTC clusters for further downstream analysis.

References

- [1] Cristofanilli, M., et al., *New Engl J Med*, **351**(8): p. 781-791 (2004)
- [2] Gabriel, M.T., et al., *Clin Chem*, **62**(4): p. 571-81 (2016)
- [3] Li, P., et al., *Proc Natl Acad Sci USA*, **112**(16): p. 4970-4975 (2015)
- [4] Magnusson, C., et al., *Anal Chem*, **89**(22): p. 11954-11961 (2017)
- [5] Zhang, Y., et al., *Int J Mol Sci*, **24**(4): p. 3338 (2023)
- [6] Allard, W.J., et al., *Clin Cancer Res*, **10**(20): p. 6897-904 (2004)



POROS Giga: Acoustofluidic platform for clinical-scale cell engineering

Mugdha Sinha^{1,2}, Mohammad Albuhsin^{1,2}, Jahir Islam¹, J. Mark Meacham^{1,3}, and Michael M. Binkley¹

¹OpenCell Technologies, Inc., St. Louis, MO 63110, USA

²Department of Biomedical Engineering, Washington University in St. Louis, St. Louis, MO 63130, USA

³Department of Mechanical Engineering and Materials Science, Washington University in St. Louis, St. Louis, MO 63130, USA

Introduction

As cell- and gene-based therapies emerge for cancer treatment and regenerative medicine applications, novel methods of biomolecular delivery of diverse targets (e.g., nucleic acids, proteins, membrane-impermeable molecules) are needed. One such application, the development of chimeric antigen receptor T cell (CAR-T) therapy involves genetically modifying T-cells with payloads encoding a CAR to target a specific cancer type in the patient. Currently available approaches utilize viral vectors (adenovirus, adeno-associated virus, or lentivirus) to deliver small (<7 kba) mRNA or DNA molecules to the cell [1]. Due to the limitations imposed on the genetic payload size, physical methods including mechanoporation (SQZ Biotech, OpenCell) and electroporation (Lonza Nucleofector, MaxCyte) are being evaluated as compelling alternatives [2].

As an established method, electroporation is the standard for benchtop transfection and payload delivery to cells; however, it can lead to low cell viability after treatment (<40%) because of the high strength of the applied electric field (1–2 kV/cm). Here, we present the application of a novel, non-contact mechanoporation system for continuous modification of cell suspensions using an acoustofluidic approach. The POROS Giga platform uses a bimorph transducer to pump sample through a 340-nozzle microarray with either 30- or 40- μm diameter orifices (Fig. 1) [2,3]. As the cells pass through these constrictions, membrane deformation results in reversible pore formation. The 100–150 nm pores remain open for tens of seconds to allow for passive molecule uptake or active electrophoresis of payload using a low-strength external field (~ 100 V/cm). We assess device performance using cell viability, cell recovery, and delivery efficiency for the two MNAs at different operating conditions.

Methods

The POROS Giga is a scaled version of our earlier cartridge-based system, which had a fixed volume of ~ 1 mL. Here we describe a high-throughput prototype device capable of continuous flow operation at up to 50 mL/min (Fig. 1B), evaluating its application for payload introduction to hard-to-transfect cells. The experimental system comprises a bimorph transducer used to drive the atomization process and a micronozzle array (MNA) mounted in a 3D-printed housing. A 25-mm diameter, 1.5-mm thick PZT-8 transducer (APC International, PA) was bonded to a custom fabricated aluminum holder (Veranex Solutions, Inc., RI). The cylindrical aluminum holder geometry was optimized using a combination of computational modeling and ejection experiments conducted from ~ 10 to 150 kHz. The selected design was operated at the frequency exhibiting the

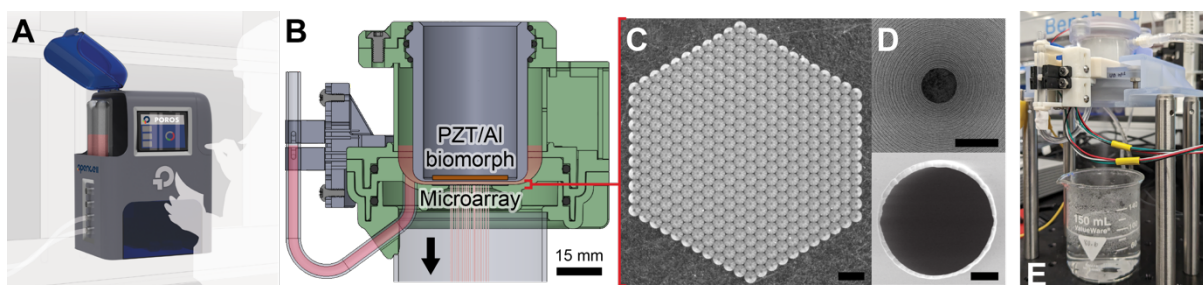


Figure 1: POROS Giga cell transfection and payload delivery platform. (A) and (B) Renderings of commercial system in development and cross-section of the prototype acoustic shear poration (ASP) module. (C) Photograph and (D) SEM images (top, inside; bottom, outlet) of a femtosecond laser-assisted wet etched 40- μm MNA [scale bars: (C) 100 μm , (D) 50 and 10 μm , respectively]. (E) Experimental setup of POROS Giga prototype ejecting DI water at 30 mL/min.

most robust spraying. The fused silica MNA featured conical nozzles with 30 and 40 μm orifices, custom fabricated to a feature resolution of $\sim 1 \mu\text{m}$ (Fig. 1C,D; FemtoPrint, SA). The MNA and transducer were held 1 mm apart using a 3D-printed polycarbonate housing with a sample volume of 50 mL, which could be continuously refreshed using a syringe pump as needed. The transducer was driven using the PDUS210 ultrasonic driver (PiezoDrive, AU) at the experimentally identified operating frequency (Fig. 1D).

To compare the effectiveness of payload delivery between MNAs with the two different orifice sizes (30 and 40 μm diameter) and at two operating flowrates (30 and 40 mL/min), we treated a 10 mL sample of Jurkat cells (1×10^6 cell/mL) suspended in serum-free media (Opti-MEM) with 0.5 mg/mL of FITC-albumin (Invitrogen, MA). Cells were continuously introduced into the fluid reservoir at a flowrate matching that of the ejection process. Controls were sampled from the reservoir upstream of the ejection process to compare outcomes in untreated and ASP-treated cells. Viability and delivery efficiency were determined using flow cytometry (Attune NxT; ThermoFisher, MA).

Results

The experimental operating frequency (f_{ex}) was located by scanning at 1 kHz intervals around the model-predicted operating frequency (f_{model}). Phase and electrical input impedance were measured and used by the PDUS210 ultrasonic driver to maintain constant current to the transducer during operation. $f_{\text{ex}} = 95.7$ kHz, deviating slightly from the predicted $f_{\text{model}} = 98$ kHz.

Overall, Fig. 2 indicates that payload delivery increased with increasing shear rate on the cells (e.g., for the smaller orifice size and higher flowrate), though results were slightly different for viability and uptake. The highest FITC-albumin delivery was observed using the 30- μm diameter orifice MNA with a flowrate of 40 mL/min (i.e., the highest shear rate). For these operating conditions, there was a 3X improvement in delivery relative to the control (34.1% FITC+ vs. 11.7% FITC+; see Fig. 2B); however, this MNA achieved only a modest increase in efficiency at 40 mL/min vs. 30 mL/min (34.1% to 31.1%), suggesting that the larger difference in orifice diameter had more impact on efficiency than the increase in flowrate for this MNA. Orifice diameter also played a role in cell viability (Fig. 2A). At 40 mL/min, the 40 μm orifice had a viability of 80.0% and delivery of 20.3%. By decreasing the orifice diameter to 30 μm , the viability of cell sample lowered to 66.2%, while the delivery efficiency increased to 34.1%. Results are promising for the application of genetic material delivery into difficult-to-transfect cell lines.

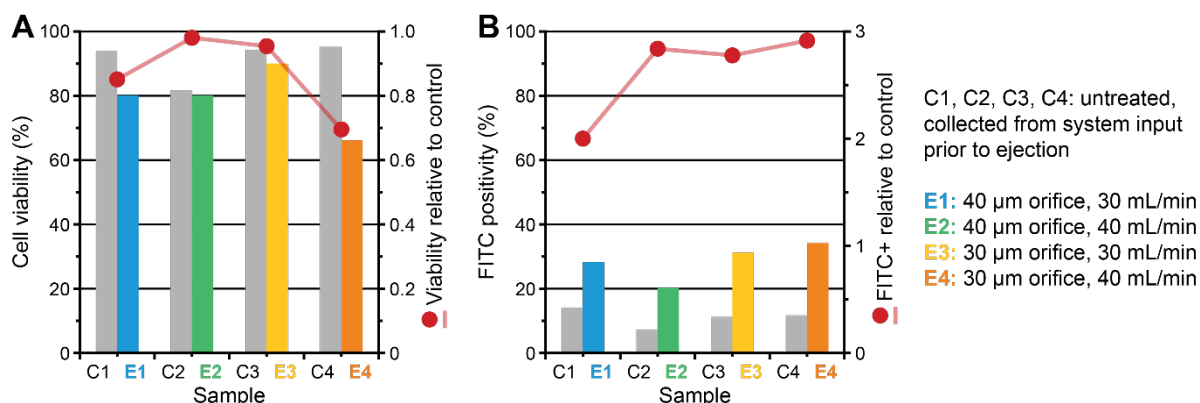


Figure 2: Experimental results of POROS prototype assessed using the 30 and 40 μm orifice sizes with flowrates of 30 and 40 mL/min. (A) Viability data for control and ASP-treated experimental samples as a percentage of total population. Red circles/line indicate viability relative to controls. (B) Delivery efficiency as indicated by FITC+ cells measured by flow cytometry. Again, red circles/line indicate uptake relative to controls.

Conclusion

In this work, we demonstrate the use of acoustic shear poration to enhance delivery of fluorophore-conjugated proteins into hard-to-transfect cells. Optimization of the transducer dimensions and micronozzle array orifice diameter played a critical role in cell viability and payload delivery efficiency. As expected, increasing flowrate through the system and constricting the orifice diameter resulted in higher levels of payload introduction at the expense of overall cell viability; however, performance remains competitive with existing physical delivery methods at significantly improved flow throughput.

The reported system represents the first use of a continuous flow, acoustic shear poration device for the delivery of complex biologics to cells, while still retaining greater than 75% cell viability. Further exploration into the efficiency of mRNA and DNA transfection is warranted to prove the feasibility of POROS Giga-based manufacturing of CAR-T cells for autologous or allogeneic therapies. Cell viability results demonstrate the superiority of acoustic shear poration over conventional electroporation for such applications.

References

- [1] J. Li, J. J. Roise, M. He, R. Das and N. Murthy, *Adv. Drug Deliv. Rev.*, 2021, **168**, 99-117.
- [2] J. M. Meacham, K. Durvasula, F. L. Degertekin and A. G. Fedorov, *Sci. Rep.*, 2018, **8**, 1-10.
- [3] J. M. Meacham, K. Durvasula, F. L. Degertekin, and A. G. Fedorov, *J. Lab. Autom.*, 2014, **19**, 1-18.



Improving microtissue histology using acoustofluidics

Dhananjay V. Deshmukh^{1,2}, Emilie Vuille-dit-Bille³, Nicola Gerber², Christine Fux², Annina Eichenberger², Sarah Heub³, Gilles Weder³, Jurg Dual², and Mark Tibbitt¹

¹Macromolecular Engineering Laboratory, Department of Mechanical and Process Engineering, ETH Zürich, Zürich, Switzerland. e-mail: deshmukd@ethz.ch

²Institute for Mechanical Systems, Department of Mechanical and Process Engineering, ETH Zürich, Zürich, Switzerland

³CSEM SA, Jaquet-Droz 1, 2002 Neuchâtel, Switzerland

Introduction

Microtissues (organoids or spheroids), can model healthy or diseased human tissues and organs. They find applications in drug testing, tissue engineering, and personalized medicine. Imaging microtissues throughout their life cycle is critical to extract high content biological information from these in vitro models. [1] Histology, i.e., slicing the microtissues into thin sections and staining them for analysis, is regarded as the benchmark for microtissue end-point analysis. Although this technique is efficient for large-scale tissue sections or biopsies, it is unfortunately substantially less efficient in the context of these sub-millimeter structures.

Typically, microtissues are suspended within an embedding medium to facilitate their processing, including sectioning, staining, and imaging. This stochastic placement results in sparse loading of microtissues in the final cassette, requiring more sections to be sectioned and imaged increasing the time and cost of the sample analysis (**Figure 1a**). Passive methods, like embedding microtissues in micropatterned gel substrates, improved sectioning efficiency and limited the loss of precious organoids. [2, 3] While effective for homogeneous microtissues, these approaches are less effective when dealing with heterogenous (in size and/or shape) microtissues, motivating the need for an active positioning approach. We developed an acoustofluidic device for arranging microtissues within HistoGel, a commonly used embedding medium in histology. Since the positions of the microtissues within the embedding medium are controlled through acoustofluidics, their downstream processing and analysis can be highly efficient (**Figure 1b**).

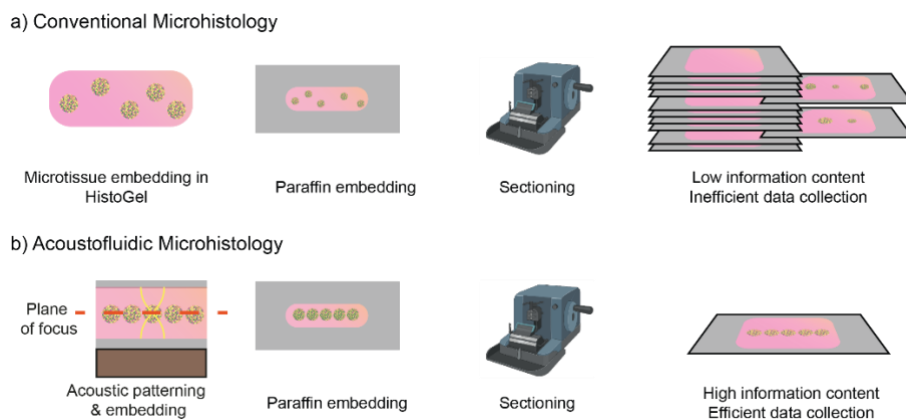


Figure 1: (a) In conventional microhistology, microtissues are randomly distributed in the sample which makes their analysis inefficient. (b) Using acoustofluidics microtissues can be patterned such that they are coplanar, enabling fast and efficient data collection.

Acoustically assisted microhistology

We engineered a metal acoustofluidic device to pattern microtissues within HistoGel. A $\lambda/2$ acoustic mode aligned microtissues in the center of the channel (**Figure 2a**). By regulating the temperature of the acoustic cavity, we modulated the viscosity of HistoGel to enable acoustofluidic patterning at high temperatures

(~50°C) when it was still liquid. Once the microtissues were positioned, the HistoGel was solidified by cooling the device to maintain the pattern. Around 80% of the microtissues were patterned within 100 μm of the center of the channel (**Figure 2b**).

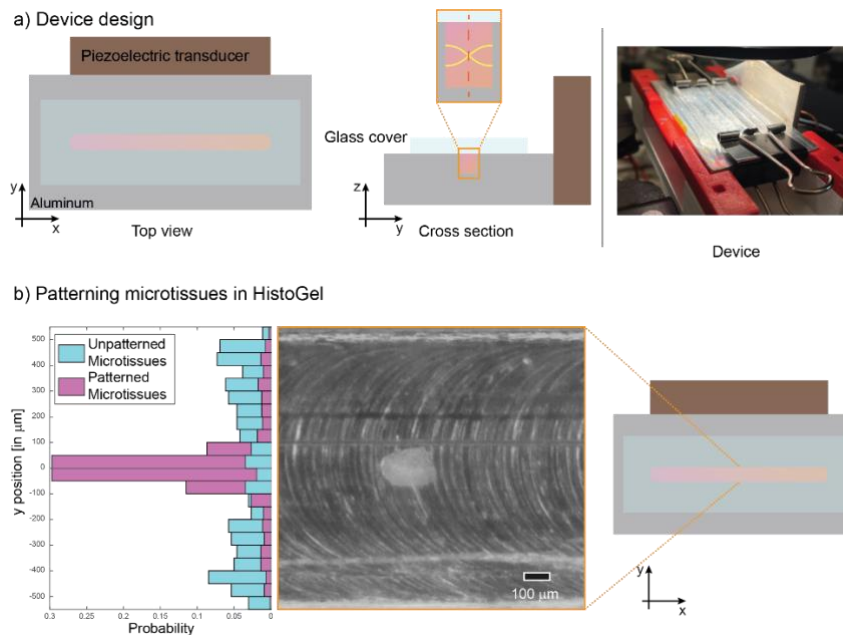


Figure 2: Patterning microtissues within HistoGel (a) Device design and the device under the microscope. (b) Patterning efficiency of microtissues in HistoGel, acoustically patterned (pink), random (blue).

Using this technique, we formed collinear microtissue constructs. Multiple microtissue constructs were combined together in order to make the patterned constructs suitable for further processing (**Figure 3a**). Initial sectioning trials have shown promising results with coplanar microtissues observed in the histological sections (**Figure 3b**).

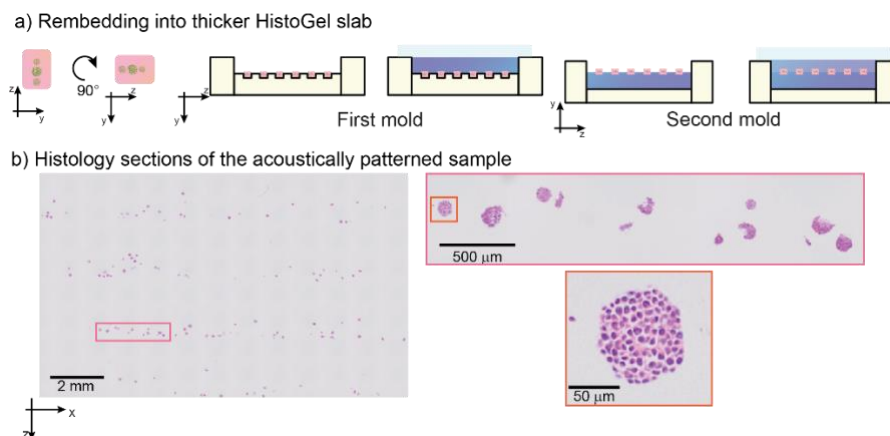


Figure 3: (a) Re-embedding the samples (in pink) into a thicker slab of HistoGel (blue). The surrounding HistoGel is dyed blue to distinguish it from the samples. (b) H&E staining (left) full section of acoustically pattern HistoGel sample. (right) one channel of section and a single micro-tissue.

Conclusion

Through our experiments, we have demonstrated that using acoustofluidics can substantially enhance the efficiency of microtissue histology with only minimal modifications to the traditional procedure.

References

- [1] Rios, A. C. & Clevers, H. Imaging organoids: a bright future ahead. *Nat. Methods* **15**, 24–26 (2018).
- [2] Heub, S. *et al.* Coplanar embedding of multiple 3D cell models in hydrogel towards high-throughput micro-histology. *Sci. Rep.* **12**, 9991 (2022).
- [3] Gabriel, J., Brennan, D., Elisseff, J. H. & Beachley, V. Microarray embedding/sectioning for parallel analysis of 3D cell spheroids. *Sci. Rep.* **9**, 16287 (2019).

Droplet upon a superhydrophobic surface for studying fluid interactions with acoustic waves

Kha Nguyen¹, Jeremy Orosco¹, Shuai Zhang², Antoine Pallois³, Stefan Llewellyn Smith^{1,4}, and James Friend^{1,2}

¹Department of Mechanical and Aerospace Engineering, University of California San Diego, La Jolla, CA 92093

²Department of Materials Engineering, University of California San Diego, La Jolla, CA 92093

³École Polytechnique, Route de Saclay, 91128 Palaiseau, France

⁴Scripps Institution of Oceanography, University of California San Diego, La Jolla, CA 92093

E-mail: jfriend@ucsd.edu, URL: <http://friend.ucsd.edu>

Introduction

Surface acoustic waves (SAWs) generated on a piezoelectric substrate, such as lithium niobate (LiNbO₃ or LN), travel along the substrate and transfer energy into fluid domains that they encounter. Such waves can be generated at wavelengths permitted by micro- and nanosized channels and introduce turbulence and chaotic advection into regions where low-Reynolds-number flow dominates. Thus, their utility in a variety of open and confined microfluidic domains has been explored extensively [2]. However, much of the underlying physics of acoustic streaming remains a puzzle. We demonstrate a novel and easy-to-replicate experimental setup involving traveling SAWs introduced to a well-understood geometry, a spherical droplet stabilized on a superhydrophobic surface, through a microsized circular interface between the substrate and the fluid domain. The experimental configuration is able to portray the transduction of SAWs at the fluid-substrate interface: from internal streaming to bulk kinematic motion of the droplet, along with the interpolated behaviors that marry these extremes. We show that this behavior is a continuously varying function of system geometries and Rayleigh wave properties. We supplement our experiments with a numerical study of the droplet's acoustic streaming field in order to correlate and better understand the observed hydrodynamics.

Materials and method

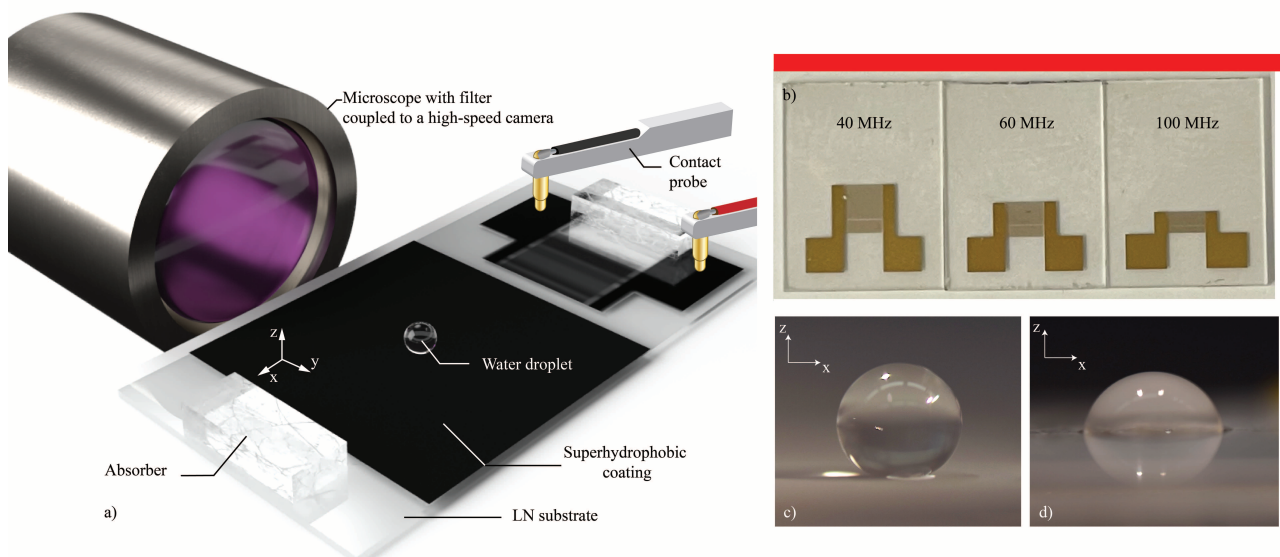


Figure 1: a) The 10 μ l DI water droplet, of approximate diameter 2.7 mm, as it is entrapped at a flaw in the superhydrophobic surface on the b) LN SAW devices of various resonant frequencies. Compared to (c) the relatively wettable surface of LN, with a contact angle for DI water of approximately 45°, the (d) superhydrophobic coating produces a nearly spherical droplet, with a contact angle exceeding 175° despite the micro-scale trapping flaw upon which it rests.

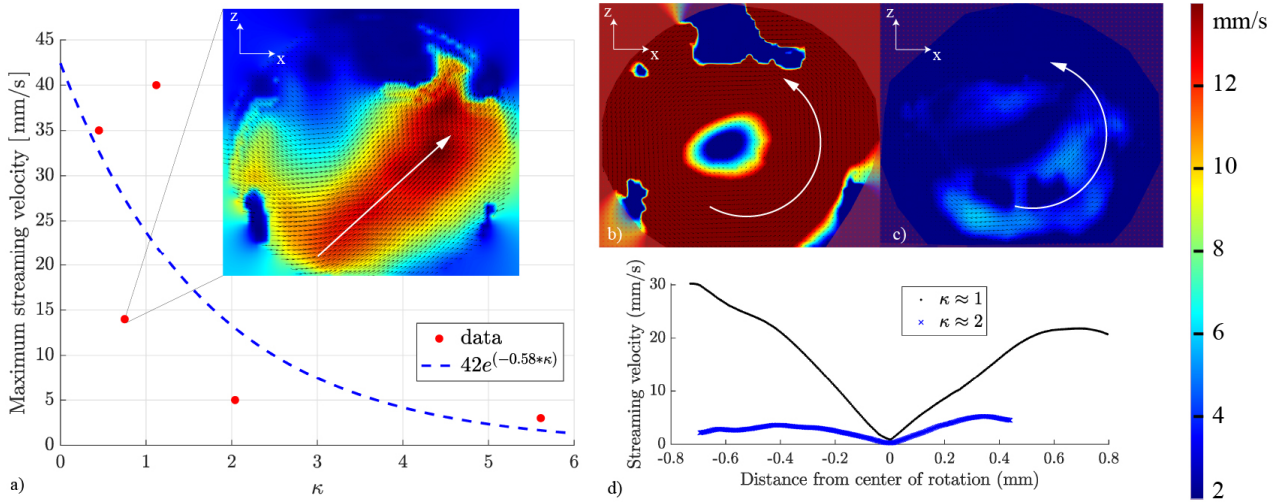


Figure 2: a) Maximum velocity found in droplet reduces exponentially as κ increases. Bulk streaming is observed at $\kappa \approx 0.7$ while rigid-body-like rotation dominates at b) $\kappa \approx 1$ and c) $\kappa \approx 2$ with d) lower streaming velocity.

5 nm/400 nm inter-digital transducers (IDTs) of resonant frequencies of 40, 60, or 100 MHz for SAWs generation were fabricated upon 500 μm thick, double-polished 128° Y-rotated cut LN substrate as seen in Figure 1. Soot collected from incomplete burning of commercially available candles and dispersed in a 1g soot/1 mL acetone solution was spray-coated on LN substrate to create a superhydrophobic coating [3]. Defects on the coating were created by spinning tungsten tips that made brief contact with the sooted substrate. Hence, the defects' sizes were close to the tips' diameters of 100, 200, 500, and 1000 μm . To observe the fluid flow, an experimental setup was devised as shown in Figure 1. The captured images were processed using the PIVLab Toolbox in MATLAB[®].

Preliminary results and discussions

The attenuation length α_r^{-1} of SAWs in solid substrates only depends on system geometries, such as speed of sound and densities of the fluid and solid and the frequency of SAWs [1]. Since the attenuated acoustic wave are transmitted into liquid, the smaller the α_r^{-1} value is, the faster the acoustic energy can be transmitted into droplet in a shorter length. We define the nondimensional parameter $\kappa = \frac{\alpha_r^{-1}}{a}$ with a as the diameter of the circular defect. Intuitively, over a fixed aperture diameter, if $\kappa \ll 1$, then the SAWs attenuate into the fluid rapidly and such transfer a great deal of energy, causing the droplet's internal hydrodynamics such as bulk streaming with maximum velocity at about 35 mm/s as seen in Figure 2 with $\kappa \approx 0.7$. On the other hand, if $\kappa \gg 1$, we observe little to no bulk streaming as evident for $\kappa \approx 2$. Interestingly, our results indicate that there is rigid-body-like rotation. The slope of streaming velocities standard deviation reduces (from 15 mm/s to 7 mm/s for $\kappa \gg 1$ in Figure 2b and $\kappa \approx 2$ in Figure 2c, respectively), suggesting that rigid-body-like rotation is the other extreme of our setup in contrast with bulk streaming. We hypothesize that this is from boundary layer streaming coupling with the asymmetrical nature of the setup. As the generated SAWs enter the droplet on the left, the attenuated SAWs energy causes boundary layer streaming at the fluid-substrate interface which generate rigid body like rotation. Note that at $\kappa \gg 1$, the droplet still has high streaming velocity and also rigid-body-like rotation, marrying the two extremes, aligning with our expectations.

Conclusion

We presented a low-cost, easy-to-set-up platform for observing acoustic streaming in unconstrained spherical droplet, potentially offering a promising means to improve researchers' understanding of the phenomenon.

References

- [1] W. Connacher, J. Orosco, and J. Friend. Droplet Ejection at Controlled Angles via Acoustofluidic Jetting. *Physical Review Letters*, 125(18):184504, Oct. 2020. Publisher: American Physical Society.
- [2] W. Connacher, N. Zhang, A. Huang, J. Mei, S. Zhang, T. Gopesh, and J. Friend. Micro/nano acoustofluidics: materials, phenomena, design, devices, and applications. *Lab on a Chip*, 18(14):1952–1996, July 2018.
- [3] T. F. Qahtan, M. A. Gondal, I. O. Alade, and M. A. Dastageer. Fabrication of Water Jet Resistant and Thermally Stable Superhydrophobic Surfaces by Spray Coating of Candle Soot Dispersion. *Scientific Reports*, 7(1):7531, Aug. 2017. Number: 1 Publisher: Nature Publishing Group.

Microstreaming induced by the complex motion of a micro-pillar

Jules Ghesquiere, Michaël Baudoin, Olivier Bou Matar, and Sarah Cleve*

Univ. Lille, CNRS, Centrale Lille, Univ. Polytechnique Hauts-de-France, UMR 8520 - IEMN - Institut d'Électronique de Microélectronique et de Nanotechnologie, F-59000 Lille, France
*sarah.cleve@univ-lille.fr

Introduction

Acoustically propelled microswimmers open some outstanding perspectives for microsurgery and targeted drug delivery since they can be activated remotely with a biocompatible source of energy. Recent studies have featured the propulsion of solid micro-swimmers, propelled thanks to deformable, acoustically excited tails [1, 2]. The main mechanism of propulsion is the microstreaming induced by the oscillatory interaction between the swimmer and the surrounding liquid. Yet, a fine understanding of the underlying physical mechanisms is still lacking and hinders the development of more advanced 3D steerable swimmers. In the present work, we investigate the link between the vibrational modes of individual tails and resulting streaming structures. The tails are made of deformable micro-pillars attached to a glass slide and excited with a piezoelectric transducer. The frequency response of the micro-pillar and of the glass support is analyzed with a laser Doppler vibrometer and correlated to the induced microstreaming for a frequency range of 1 to 300 kHz. The results exhibit a variety of modes of the pillar vibration, some mainly due to the support vibration and some to the deformation of the micro-pillar itself. These results pave the way towards the 3D control of microswimmers by excitation of specific modes.

Experimental setup and procedure

The experimental procedure consists of three steps: (i) fabrication of the micro-pillar, (ii) observation of microstreaming via particle tracking velocimetry and (iii) characterization of the vibrations of the micro-pillar and the glass slide. Similarly to the procedure proposed in Ref. [3], the micro-pillars are produced by polymerizing polyethylene glycol diacrylate (molecular weight of 250, Sigma-Aldrich) mixed with 10 % photo-initiator (2-hydroxy-2-methylpropiophenone 97 %, Sigma-Aldrich). The solution is filled into the cavity formed by a 200 μm high PDMS chamber and a glass slide. It is then mounted on an inverted microscope (Nikon Ti2-E) and the pillar is grown by exposition to UV light using a numerical mask (Alveole Primo). It is naturally bonded to the silanized glass slide but not to PDMS due to the formation of an oxygen inhibition layer. Consecutively, the PDMS chamber is removed, the sample is washed and a 600 μm high chamber is placed around the pillar and filled with water containing 1 μm tracer particles (Fisher Scientific) to investigate the flow structure with particle

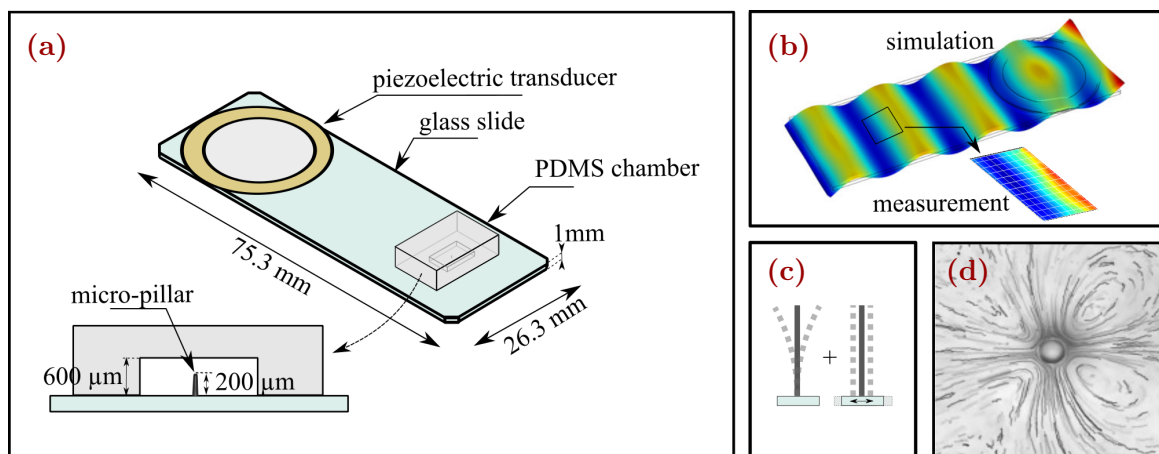


Figure 1: (a) Schematics of the experimental device. (b) Deformation of the glass plate at 32 kHz, (c) corresponding movement of the micro-pillar (motion induced by glass support plus deformation of the pillar), and (d) induced microstreaming.

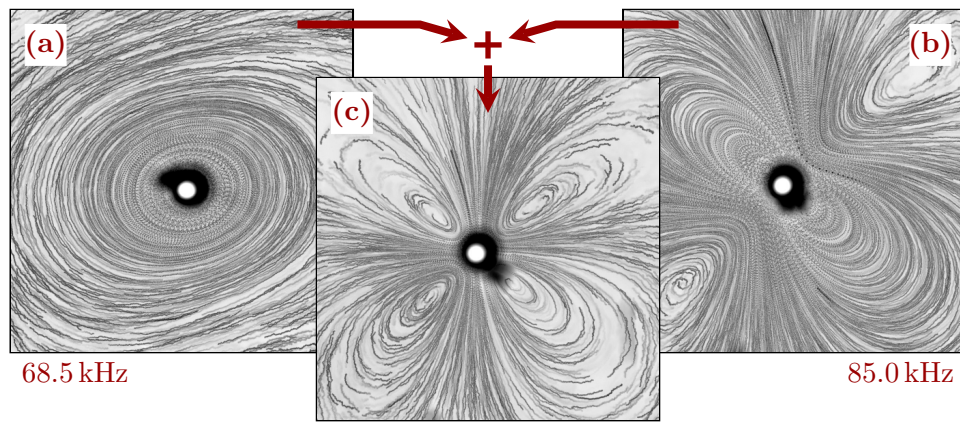


Figure 2: Microstreaming induced (a) at 68.5 kHz, (b) at 85.0 kHz and (c) by superposition of the two. The diameter of the pillar is 55 μm .

tracking velocimetry (PTV). The system, see also fig. 1(a), is then excited with a piezoelectric transducer (RS 724-3162) at frequencies ranging between 1 and 300 kHz. The tracers particle movement is recorded with a camera (Photometrics Prime BSI) at 12 fps for frequencies at which microstreaming sets in. Ultimately, the frequency response of the glass slide as well as of the micro-pillar is measured with a laser-doppler-vibrometer (Polytech MSA-500).

Results

The typical microstreaming flow structures reported in the literature [4] are (i) a structure with four lobes as in fig. 1(d), and (ii) a circular microstreaming flow as in fig. 2(a). They result respectively from translational and circular rigid motion of the micro-pillar. Here, by scanning a large frequency range, we report a variety of flow structures resulting from the combination of support vibrations and micro-pillar deformation eigenmodes, and are further able to link each flow structure to a specific micro-pillar vibration. In addition, we show that these modes can be combined to create new flow structures and finely tune them with different weights of each frequency component (see e.g. fig. 2(b)).

Conclusions

In the present work, we study the microstreaming flow structures induced by an acoustically excited micro-pillar and their correlation to the micro-pillar vibrations. We show that many different modes, including high frequency flexural vibrations of the micropillars, can be excited leading to a variety of flow structures. The combination of these modes by adjusting the frequency content of the excitation gives a large number of degrees of freedom to control the flow structure, paving the way toward the steerability of microswimmers. Extension to further investigation of the 3D flow structures is planned in future experiments.

Acknowledgements

This research work has been partially undertaken with the support of IEMN fabrication (CMNF) facilities. The authors thank David Guerin for valuable help and advice in the fabrication process.

References

- [1] M. Kaynak, A. Ozcelik, A. Nourhani, P. E. Lammert, V. H. Crespi and T. J. Huang. *Lab on a Chip* **17(3)**, 395-400 (2017).
- [2] D. Ahmed, T. Baasch, B. Jang, S. Pane, J. Dual and B. J. Nelson. *Nano letters* **16(8)**, 4968-4974 (2016).
- [3] S. Orbay, A. Ozcelik, H. Bachman and T. J. Huang. *Journal of Micromechanics and Microengineering* **28(2)**, 025012 (2018).
- [4] T. Hayakawa, S. Sakuma and F. Arai. *Microsystems & nanoengineering* **1(1)**, 1-9 (2015).



About altering equilibrium positions of particles trapped in an acoustic tweezer based on a 2DsSAW

Jörg König¹, Zhichao Deng¹, Sebastian Sachs¹, Hagen Schmidt², Christian Cierpka^{1,3}

¹Institute of Thermodynamics and Fluid Mechanics, TU Ilmenau, Ilmenau, Germany
E-mail: Joerg.Koenig@tu-ilmenau.de URL: <http://www.tu-ilmenau.de/ttd>

²IFW Dresden, SAWLab Saxony, Dresden, Germany

³Visiting research fellow, Department of Biomedical Engineering, Lund University, Lund, Sweden

Introduction

Acoustic tweezers based on a two-dimensional standing acoustic wave field (2DsSAW) have been demonstrated to be powerful for arranging particles or biological cells in equidistant, regular patterns [1,2]. Studies revealed either a rectangular or a diamond pattern of individual objects trapped in the microfluidic chamber, mainly depending on the ratio between particle diameter and surface acoustic wave (SAW) wavelength $\xi = d_p/\lambda_{\text{SAW}}$ [2,3,4]. Primarily, the patterns formed have been considered as only governed by the acoustic radiation force (ARF), and the theoretical considerations were limited to 2D. However, the acoustic pressure field within the chamber is of three-dimensional nature and a complex acoustically induced fluid flow pattern exists, which exerts on the particles due to viscous drag. This causes particles to be displaced from locations predicted solely by considering the ARF, and may explain recently found particle trapping locations coinciding with positions associated with antinodes, even though the particles have a positive contrast factor [4]. To strengthen the fundamental understanding of the patterning mechanism governed by the interplay between both forces, investigations are required comprising experiments to determine the particle pattern formation, over the measurement of the 3D fluid flow inside the micro chamber to experimentally assisted numerical simulations considering the particles not only as point but with definite size and shape.

Methods and results

At first, the influence of the particle-diameter-to-wavelength ratio ξ on the formation of the 3D patterns is studied experimentally, employing a SAW device based on a 2DsSAW field excited by two pairs of opposing interdigital transducers. It consists of a micro chamber made of PDMS at central position in between both pairs of opposing IDTs deposited on a 128° rotated Y-cut lithium niobate substrate. The lateral width and the height of the chamber amount to $1200\ \mu\text{m}$ and $88\ \mu\text{m}$, respectively. The SAW wavelength in the crystallographic Y-direction is $120\ \mu\text{m}$ and serves as reference wavelength in terms of the particle-diameter-to-wavelength ratio ξ . Polystyrene particles of $10\ \mu\text{m}$, $19\ \mu\text{m}$ and $33\ \mu\text{m}$ in diameter were used for trapping, yielding a particle-diameter-to-wavelength ratio ranging from 0.083, over 0.158 to 0.275. Besides the determination of the 3D particle patterns, the three-dimensional velocity distribution inside the chamber was measured applying astigmatism particle tracking velocimetry (APTV) [5]. For the flow measurement, polystyrene particles of $450\ \text{nm}$ in diameter were suspended as tracer particles. Details about the APTV setup used and reliability of fluid flow measurements in sSAW-devices can be found in Sachs et al. [6]. During the measurement duration of 5 s, resonant frequency and power were kept constant. To increase the number of particle trajectories, measurements were repeated 165 times under identical conditions.

A transformation from a rectangular to a diamond pattern with increasing ξ was found, see Figure 1. In all experiments, particles were trapped in two different height levels, one being in close vicinity to the substrate surface and the other close to the top of the micro chamber. Interestingly, in the case of the intermediate particle-diameter-to-wavelength ratio of $\xi \approx 0.158$ a rectangular and a diamond particle pattern coexist at the bottom and top of the micro chamber, respectively. Moreover, for the large ratio of $\xi \approx 0.275$, two patterns staggeredly arranged in lateral direction are found, with one close to the bottom and the other close to the top of the micro chamber. More details and further results obtained with comparable values of ξ in a down-scaled SAW device but same ratio between lateral width of the chamber to SAW wavelength can be found in Deng et al. [4]. Considering the distribution of the acoustic force potential expected in those devices, the particle positions depicted in Figure 1c) indicate particles to be trapped not only at pressure nodes but also at antinodes [4]. Figure 1c) also illustrates the spatially and time averaged velocity field close to the mid-plane of the micro chamber. The velocity field reveals a repetitive pattern of 3D vortical structures, where the distribution of the u_2 -component resembles the 2DsSAW [3]. While regions of positive u_2 -velocities coincide with regions

of maximum displacement amplitude of the 2DsSAW, negative u_z -velocities can be seen at positions of minimum displacement amplitude. The latter correspond to positions of acoustic force potential wells, where particles or cells of appropriate size can be trapped [2,3]. Very interestingly, particles of $d_p = 33 \mu\text{m}$ in diameter trapped within these areas were almost in contact with the substrate surface ($\bar{z}_{\text{bottom}} \approx 16.8 \mu\text{m}$), while most of the particles were levitated to a mean height of $\bar{z}_{\text{top}} \approx 44.0 \mu\text{m}$ above the antinodes.

Conclusion

The 3D patterning formation and the acoustically induced fluid flow in a microfluidic chamber of an acoustic tweezer based on a 2DsSAW field has been characterized experimentally. These investigations revealed a complex 3D vortical structure within the chamber, with a formation of the vortices that agree well to the 2DsSAW field at the fluid-substrate interface. As particle trapping locations are governed by the balance of the ARF and drag force, different and coexisting particle patterns result depending on the particle-diameter-to-wavelength ratio ξ [4]. To strengthen the fundamental understanding, further information are acquired by the in situ measurement of the 2DsSAW and three-dimensional numerical simulations, which allows to estimate acoustic forces for arbitrarily shaped particles beyond the Rayleigh limit [7]. This hybrid approach with further results relating particle patterns to the acoustic force distribution are going to be presented and discussed on site, and strengthens fundamental understanding of the interplay of the forces, important to facilitate a more precise manipulation of particles and cells in those acoustic tweezer devices.

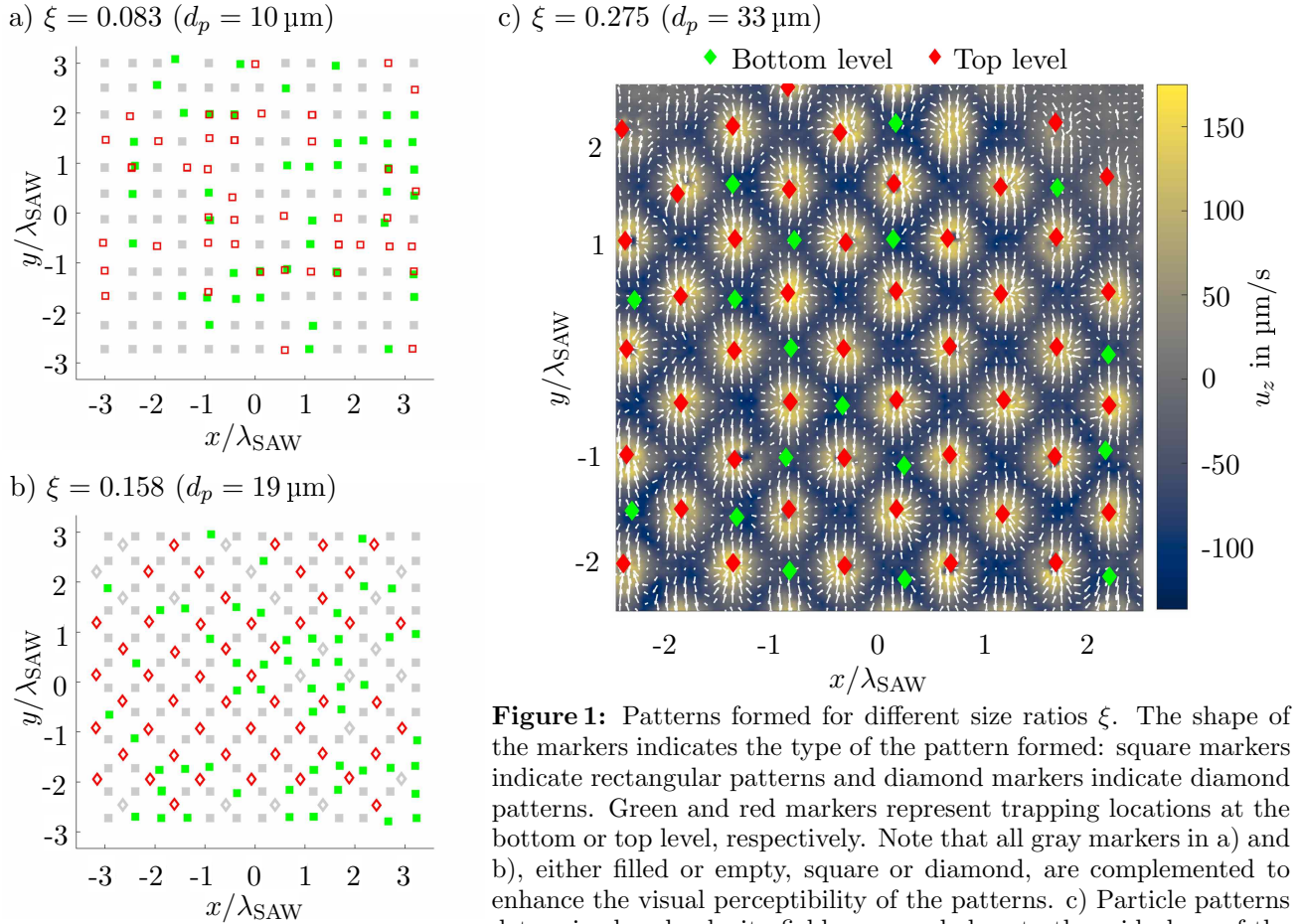


Figure 1: Patterns formed for different size ratios ξ . The shape of the markers indicates the type of the pattern formed: square markers indicate rectangular patterns and diamond markers indicate diamond patterns. Green and red markers represent trapping locations at the bottom or top level, respectively. Note that all gray markers in a) and b), either filled or empty, square or diamond, are complemented to enhance the visual perceptibility of the patterns. c) Particle patterns determined and velocity field measured close to the mid-plane of the micro chamber.

Acknowledgement

Financial support by the Deutsche Forschungsgemeinschaft (DFG) through CI 185/6-1, CI 185/8-1 and SCHM 2365/17-1 is gratefully acknowledged.

References

- [1] F. Guo et al. Proc. Natl. Acad. Sci. U.S.A. **143**, 509-519 (2018).
- [2] D.J. Collins et al. Nat. Commun. **6**, 8686 (2015).
- [3] R. Weser et al. Lab Chip **22**, 2886-2901 (2022).
- [4] Z. Deng et al. Lab Chip **23**, 2154-2160 (2023).
- [5] C. Cierpka et al. Meas. Sci. Technol. **21**, 045401 (2010).
- [6] S. Sachs et al. Lab Chip **22**, 2011-2027 (2022).
- [7] T. Baasch and J. Dual. J. Acoust. SoC. Am. **143**, 509-519 (2018).

Acoustic streaming in the fluid of the inner ear

Charles Thompson^{1,2}, Kavitha Chandra^{1,2}, and Adian Keefe^{1,2}

¹Department of Electrical and Computer,UMASS Lowell, Lowell,MA,USA

E-mail: charles_thompson@uml.edu, URL: <https://morseatuml.us/faculty/charles-thompson>

²CACT, UMASS Lowell, Lowell,MA, USA

Introduction

The cochlea of the inner ear is a small fluid-filled chamber responsible for converting acoustically induced mechanical vibrations into the neural signals we use to interpret sound. The internal sensory structures within the cochlea can be excited by air and by bone conduction. The mechanical process of air and bone conduction hearing is shown in Fig. 1. The arrows in the figure denote the relative velocity directions of the tympanic membrane (TM), oval window (O), and round window (R).

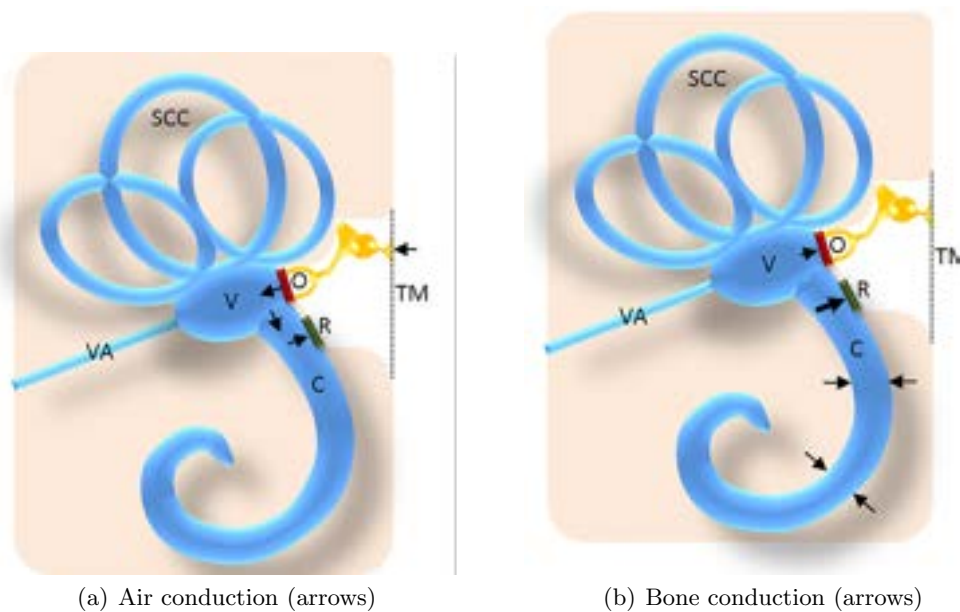


Figure 1: Normal air and bone conduction hearing mechanisms; C, cochlea (uncoiled) ; O, oval window; R, round window; TM, Tympanic membrane(eardrum); SCC, Semicircular canal; V, vestibule; VA, vestibular aqueduct; Schematic from [1]

Air conduction describes the typical process of hearing and is shown in Figure 1(a). Air conduction relies on the airborne sound-induced mechanical vibration of the tympanic membrane (TM). This vibration is communicated to the perilymph-filled cochlea (C) via the oval window (O) of the inner ear through the auditory ossicles. By virtue of the incompressible behavior of the enclosed fluid in the cochlea, the volume velocity of the oval and the round windows have equal magnitude and act in opposite directions. The motion of the oval and the round window establishes a pressure gradient across the basilar membrane that is inside the cochlea setting this flexible membrane into motion.

An alternative process that can be utilized to stimulate hearing is bone conduction. The mechanical features of bone conduction are shown in Figure 1(b). In contrast to air conduction, sound induces vibration of the otic capsule, the bony outer wall of the inner ear that includes the cochlea. By virtue of the incompressible behavior of the enclosed fluid in the cochlea, the sum of the volume velocities at the oval and the round windows must equal the time rate of change of the volume of fluid in the cochlea. A pressure gradient across the basilar membrane is established when the oval and round

windows move at different velocities in like directions.

Problem statement and objective

In this paper the fluid motion that results from air and bone conduction is examined. The analytical approach and cochlear model presented embodies the salient features present in the compressive bone conduction process. The scala vestibuli and scala tympani will be modeled as two-dimensional fluid-filled channels. The channels are connected at the helicotrema and the fluid motion therein through their coupling at the cochlear partition.

The rapid variation in the vibration amplitude of the basilar membrane with position results in the generation of evanescent modes in the cochlear fluid. It is shown that the effect of such vibrations can cause strong and localized acoustic streaming flows which can be varied as a function of frequency. New slip-velocity vector boundary conditions are given and are used to generate flows outside of the boundary layer region. Prior work on bone conduction is summarized in [2] and a description of acoustic streaming relevant to the problem at hand is given in [3].

Findings

In this paper, we will present an analysis of fluid streaming that results from bone and air conduction. Using asymptotic matching, boundary conditions have been derived that allows investigation of the generation of the outer flow field. We have also demonstrated that location sensitive acoustic streaming can be generated by tuning the cochlear partition.

The findings presented here may also provide an alternative to surface wave excitation and manipulation fluid motion via acoustic streaming in microfluidic chip applications. The ability to generate localized streaming over an extended range of frequencies will be investigated in future work.

References

- [1] Mai-Lan Ho, Third Window Lesions, *Neuroimaging Clinics of North America*, **29**, 57-92, (2019).
- [2] David Chhan and Charles Thompson and Kate Aho, Two-dimensional analysis of fluid motion in the cochlea resulting from compressional bone conduction, *Journal of Sound and Vibration*, **333**, 1067–1078, (2014)
- [3] Charles Thompson and Kavitha Chandra, Acoustic streaming resulting from compression of the cochlear bony capsule, *Journal of the Acoustical Society of America*, **150**, 4548–4557, (2021)
- [4] A. Coauthor. *Procs. pp. 124-127, Some International Conference*, Conference City, 1 - 6 July 2014.



Universal interdigital transducer (IDT) for stable multi-patterns aggregation of microparticles in a droplet.

Etien Martinez Roman, Bjørn M. Qvenild-Svenningsen and Diego Saldaña.
Department of Energy and Process Engineering, Norwegian University of Science and Technology,
Trondheim, Norway
E-mail: etien.martinez@ntnu.no

Introduction. Particle aggregation and patterning are key processes in biomedical and biochemical applications such as tissue engineering, control on cell-cell interactions, enhancement of the detection sensitivity, and speed of biosensors and enrichment [1]. Aiming for a fast, simple and compact, low-cost, label-free, biocompatible and non-invasive method to conduct these processes we have acoustofluidics strategies, in particular, the use of surface acoustic waves (SAW) in sessile droplets where micro or nanoparticles are suspended. This versatile technique has been used extensively in biotechnology and material science as a small-scale and less complex alternative to the conventional methods of microfluidics in a channel or sample concentration via centrifugation [2]. A plethora of aggregate states are found, in most of the cases, generating a SAW with an interdigital transducer (IDT). Relevant examples are concentric rings of quasi-static particles, levitating or sedimented roundish clusters, aligned arrays, a rotating ring of particles close to the top of the droplet and a circular deposition at the contour of its base line [2-4]. The aggregates produced by standing SAW are typically obtained for operational frequencies of ≈ 40 MHz [3,4], while those generated by traveling SAW can appear in a range of >20 MHz [4]. Those patterns mentioned are obtained using distinct configurations, ranging from different IDT designs to the variation of the droplet characteristics (e.g., size, relative position to the IDT) and can be modified if the contact angle change change, thus becoming unstable during the evaporation process. The use of multiples IDT raises important issues because its design and implementation cannot be trivially linked with the expected outcome considering that many parameters, like shape, dimensions, type of material and electromechanical properties, must be considered [2]. In that context, we present the controlled formation of stable multi-patterns aggregates of microparticles suspended in a droplet, by solely tuning the operational frequency and the injected power of a single spiral IDT in a piezoelectric substrate. We also find a new configuration where a stationary pattern is established at the high frequency range (>60 MHz). Our results simplify and make more efficient the instrumentation process to produce aggregates and a configuration where we can systematically study different assembly mechanisms.

Materials and methods. Our setup consists in four spirals IDT fabricated using gold, via maskless aligner (MLA) lithography and e-beam metal evaporation on a piezoelectric substrate (128° YX LiNbO_3 , 0.5 mm thickness). Each device has 30 fingers, whose spacing and width set a design frequencies of 20, 40, 80 and 120 MHz. They are driven by AC sinusoidal signals produced by a Belektronig SAW generator BSG F20 that includes an attachable signal attenuator device that significantly reduces all the values of the reflection coefficient thus allowing our system to operate in a frequency range between 0.5 and 120 MHz with powers from 0.5 to 400 mW. We study DI-water droplets of 2 microliters containing fluorescent polystyrene particles (PS-DVB, Bang Lab., Inc.) of either 7 or 4 micrometer diameters at concentration of 5 mg/ml and 1 mg/ml, in that order. The particles dynamics is visualized with an AOS PROMON U1000 Color camera attached to an inverted microscope Nikon Eclipse Ti2.

Results and discussions. Our method moves away from the traditional operational mode of IDT, which establishes that the preferred operational frequency should match with the design one to obtain the maximal efficiency. In contrast, our results prove that, even though we can have losses, this does not prevent obtaining the aggregation patterns. The main analysis is performed with the IDT with 80 MHz design frequency, while the other devices, designs for 20, 40 and 120 MHz, are used to show the reproducibility of the results in other configurations, thus establishing the universal character of the method. Tuning the operational frequency between 5 and 120 MHz we found multiple aggregation patterns (Fig. 1) corresponding to different powers supplied to the IDT. For frequency values ranging from 5 to 40 MHz the particles dynamic, for both 7 and 4 μm , is dominated mostly for pressure traps associated to a stationary acoustic field that the SAW impose in the droplet base. We observe concentric

ring patterns where, increasing the power supplied, we detect clusters formed for few particles (~10) that levitate at a small distance from the substrate, a clear indicator of the relevance of hydrodynamic forces when we provide more energy into the system. For the lowest frequency (wavelengths larger than substrate thickness), we obtain a pattern that is similar to a Chladni figure and can be explained if we consider that in this case Lamb waves are involved [2] and the whole piezoelectric becomes an oscillating plate.

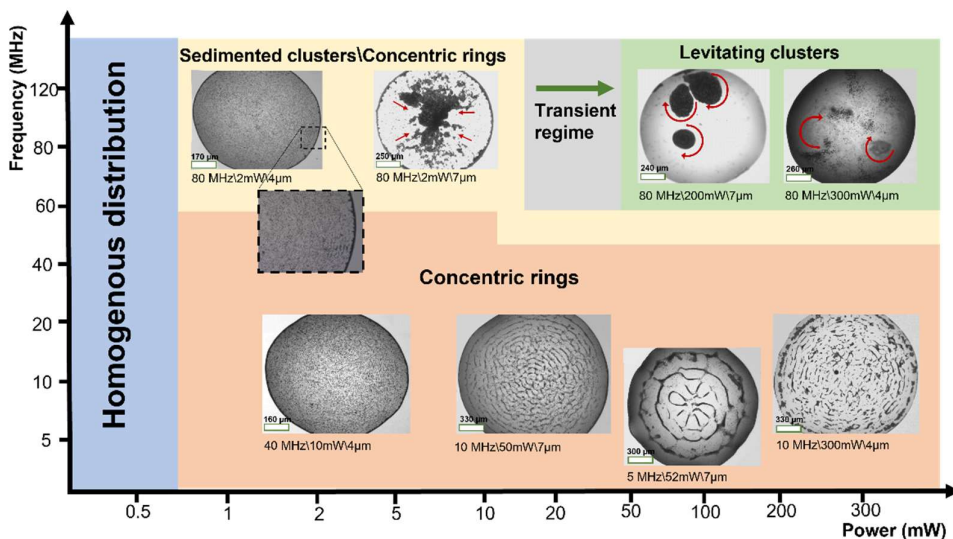


Figure 1. Phase Diagram of the aggregation patterns (not in scale). For the concentric rings distribution, at high powers there is a small-size cluster with limited motility. For high frequency (≥ 60 MHz), depending on the particle size we found either concentric rings (4 μm) or not (7 μm). By increasing the power, we found an evolution, for 7 μm , from clusters at the bottom to levitating ones, having a transient state where both phases coexist. This evolution for 4 μm particles always displays ring-like trapping. The red arrows indicate the direction of the flow.

In the frequency range from 60 to 120 MHz and low powers, using the 4 μm particle size, we can also detect the predominance of the pressure traps with the appearance of steady concentric rings, an unexpected result according to previous reports for these frequency values [4]. By increasing the particle diameter, we found the cluster formation and the disappearance of the concentric pattern. In the case of both types of particles, for the highest powers there is the same tendency in the aggregation patterns (sedimented and levitating aggregates) with the following features: i) For the 4 micrometer-particles there are always concentric rings although for 120 MHz, they are only located close to the contact line. The sedimented cluster is irregularly formed with the junction of particles trapped in the rings. The levitating clusters coexist with vortical regions where the particles are not concentrated but just follow the streamlines. ii) For the 7-micrometer particles, there can be multiple sedimented clusters or just a central sedimented cluster. The sedimented multi-clusters always coexist with levitating assemblies, which can trap almost all the particles in the suspension for the highest frequency and powers. In the range 5-80 MHz, we found that the spacing between the rings is half the wavelength of the acoustic field in the fluid, implying that the relevant pressure traps are not on the piezoelectric substrate. The static ring-like pattern could be explained exploiting the analogy with the nodal pattern of three-dimensional membranes under the acoustic field. The sedimented cluster, either central or not, occurs due to a pressure gradient that drags the particles and, if the acoustic streaming is high enough (for high frequencies or powers) it is possible that vortical regions appear where the particles are trapped and levitating. Once they are in these rotatory regions and close to the droplet free surface, they can be concentrated similarly as in spin-coating method for particle assembly.

Conclusions. We demonstrate the creation of aggregation patterns of microparticles suspended in a droplet under the action of a SAW generated by a single IDT device with spiral shape, solely tuning the operation frequency and the power supplied in relatively wide ranges. In this configuration we found that patterns produce by standing waves can appear at high frequency.

References

- [1] Trends in Analytical Chemistry **160**, 116958 (2023). Nature Reviews Methods Primers **2**(1), 30 (2022).
- [2] Applied Physics Reviews **10**, 011315 (2023). Nanotechnol. Precis. Eng. **5**, 035001 (2022)
- [3] J Nanopart Res **24**, 81 (2022)
- [4] Lab Chip **16**, 660 (2016)

Theory and numerical studies of shallow travelling-wave micropumps

Søren A.S. Kuhberg and Henrik Bruus

Department of Physics, Technical University of Denmark, Kongens Lyngby, Denmark
 E-mail: sorku@dtu.dk, URL: www.fysik.dtu.dk/microfluidics

Introduction

Peristaltic pumps are often used in microfluidics [1]. A sub-class of these are travelling-wave (TW) pumps [2], an old concept but less applied in microsystems. Here we study the basic principles of TW micropumps, in which the pumping action is set up by letting a transverse displacement wave propagate along the top and bottom walls. The wave propagation creates an oscillatory flow with a non-zero time-averaged flow rate $\langle Q \rangle$. We present the theoretical pumping characteristics with numerical validation. We find numerically that the transient time to overcome is set by the momentum diffusion time T_d and not by the oscillation period T_0 .

Model: governing equations and boundary conditions

We consider a 2D model in the xz -plane of a long, shallow microchannel of length L along x and unperturbed height $2H_0 \ll L$ along z with hard top and bottom walls at $z = \pm H_0$, see Fig. 1(a). The width W along y is assumed large, $2H_0 \ll W$, with translation invariance so that any y -dependence is disregarded. The vertical hard-wall displacement $H_1(x, t)$ is defined by a traveling wave with wavelength $\lambda = \frac{1}{n}L$ (n integer), frequency f , wave number $k = 2\pi/\lambda$, angular frequency $\omega = 2\pi f$, period $T_0 = 1/f$, and relative amplitude ϕ_0 . Thus, the total perturbed height is $2H(x, t)$ with the hard-wall positions at $z = \pm H(x, t)$,

$$H(x, t) = H_0 + H_1(x, t) = [1 + \phi_0 \cos(kx - \omega t)]H_0 \quad \text{and} \quad \text{Wo} = \sqrt{H_0^2 \omega / \nu}. \quad (1)$$

The fluid in the microchannel (density ρ , dynamic and kinematic viscosity η and $\nu = \rho/\eta$, velocity field \mathbf{v} , and pressure field p) is incompressible and governed by the Navier–Stokes equation, $\rho[\partial_t \mathbf{v} + (\mathbf{v} \cdot \nabla) \mathbf{v}] = -\nabla p + \eta \nabla^2 \mathbf{v}$, and the continuity equation, $\nabla \cdot \mathbf{v} = 0$. The non-linearity of the system is characterized by the usual Womersley number Wo given in Eq. (1). No-slip boundary conditions apply on the hard top and bottom walls, $\mathbf{v}(x, \pm H(x, t), t) = \pm \partial_t H_1 \mathbf{e}_z$, and periodicity at the end walls, $\mathbf{v}(0, z, t) = \mathbf{v}(L, z, t)$ and $p(0, z, t) = p(L, z, t)$, where the latter implies zero back pressure: the unloaded case $\Delta p = 0$. The time-averaged flow rate is $\langle Q \rangle$.

Analytical results: the time-averaged pump characteristic

The linear $\langle Q \rangle$ - Δp pump characteristic of the TW micropump is defined by the maximum time-averaged flow rate $\langle Q \rangle^{\max}$ at zero back pressure $\Delta p = 0$ (the unloaded case) and the maximum back pressure Δp^{\max} at zero flow rate $\langle Q \rangle = 0$ (the maximally-loaded case). An analytical expression for $\langle Q \rangle^{\max}$ versus Wo is found by second-order perturbation theory in ϕ_0 ,

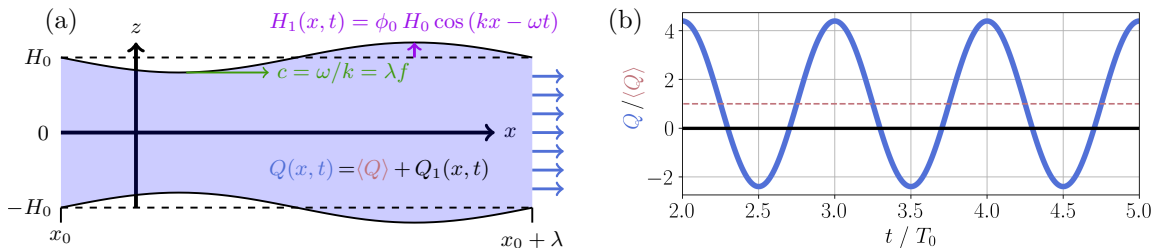


Figure 1: (a) A sketch of one wavelength of the traveling wave in the TW micropump of unperturbed height $2H_0$ at an arbitrary time t showing the hard-wall displacement $H_1(x, t)$ (magenta) with relative amplitude $\phi_0 = 0.2$, wave speed c (green), and flow rate Q (blue arrows). (b) The corresponding normalized flow rate $Q(t)/\langle Q \rangle$ (blue) versus normalized time $2 < t/T_0 < 5$ and its time-averaged value of unity (red dashed).

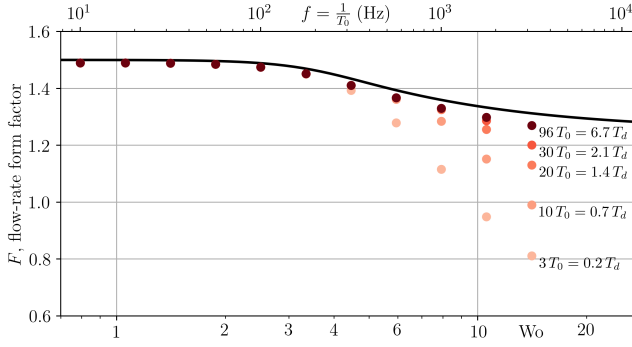


Figure 2: The flow-rate form factor F from Eq. (2) versus Wo for $H_0 = 0.1$ mm and $\nu = 8.9 \times 10^{-7}$ m²/s (water). We show the analytical perturbation-theory result (black line), with limits $F(Wo) \rightarrow \frac{3}{2} - \frac{1}{3150} Wo^4$ for $Wo \rightarrow 0$ and $F(Wo) \rightarrow \frac{5}{4} - \frac{5}{4\sqrt{2}Wo}$ for $Wo \rightarrow \infty$, and the numerical results (dots) at 11 selected frequencies at the five given times t from earliest (light red) to latest (dark red) in units of both the oscillation period T_0 and of the diffusion time $T_d = (2H_0/\pi)^2/\nu = 4.6$ ms. Numerical time averages are computed over one full oscillation starting at the times 3, 10, 20, 30, and 96 T_0 .

$$\langle Q \rangle^{\max} = \frac{2LWH_0}{n} F(Wo) f \phi_0^2, \quad F(Wo) = \frac{5 Wo^2 \left\{ \cosh(\sqrt{2} Wo) + \cos(\sqrt{2} Wo) - \frac{1}{\sqrt{2} Wo} [\sinh(\sqrt{2} Wo) + \sin(\sqrt{2} Wo)] \right\}}{8 \left\{ \frac{Wo^2 + 1}{2} \cosh(\sqrt{2} Wo) + \frac{Wo^2 - 1}{2} \cos(\sqrt{2} Wo) - \frac{Wo}{\sqrt{2}} [\sinh(\sqrt{2} Wo) + \sin(\sqrt{2} Wo)] \right\}}. \quad (2)$$

In a loaded micropump with non-zero back pressure Δp , a Poiseuille back flow $Q^{\text{pois}} = -\Delta p/R_{\text{hyd}}$ is superimposed to the TW flow $\langle Q \rangle$ due to the hydraulic resistance $R_{\text{hyd}} = 12\eta L/[W(2H_0)^3]$. The maximum back pressure Δp^{\max} is found from the zero-flow condition $\langle Q \rangle^{\max} + Q^{\text{pois}} = 0$,

$$\Delta p^{\max} = R_{\text{hyd}} \langle Q \rangle^{\max} = \frac{3\eta L^2}{nH_0^2} F(Wo) f \phi_0^2. \quad (3)$$

Clearly, it is advantageous to operate with as large a value of ϕ_0 as possible. However, this may invalidate the perturbation results, and therefore we move on to numerical simulations.

Numerical results: pump characteristic and the role of momentum diffusion

One wavelength of the pump is simulated using the finite-element software COMSOL Multiphysics with $H_0 = 0.1$ mm, $\lambda = 60$ mm, and $\phi_0 = 10^{-4}$ from time 0 to $100 T_0$ in steps of $0.01 T_0$ for a given TW frequency f . We compute the time-averaged flow rate through the cross section at $x = \lambda/2$ as $\langle Q \rangle(t) = \frac{1}{T_0} \int_t^{t+T_0} Q(t') dt'$. In Fig. 1(b) is shown $\langle Q \rangle(mT_0)$ for $m = 3, 10, 20, 30$, and 96 at 11 frequencies in the range $10 < f < 3200$ Hz. We note that below the cross-over frequency $f_d = 1/T_d = 220$ Hz, where $T_d = (2H_0/\pi)^2/\nu = 4.6$ ms is the momentum diffusion time, the numerics has converged to the analytical results after the third oscillation period, $m = 3$. In contrast, for $f = 3200$ Hz the deviation is 38% for oscillation period $m = 3$ and still as much as 3% at $m = 96$. This points to the important criterion for overcoming the transient behavior in the TW micropump: convergence is only achieved for times $mT_0 \gg T_d$. In Table 1, examples of the maximum flow rate $\langle Q \rangle^{\max}$ and back pressure Δp^{\max} are shown for increasing frequency f and decreasing channel height H_0 , keeping the displacement H_1 constant. Whereas the simple scaling laws (2) and (3) $\langle Q \rangle^{\max} \propto H_0 f \phi_0^2$ and $\Delta p^{\max} \propto H_0^{-2} f \phi_0^2$ are not quite fulfilled, the improvement in pumping performance is still significant for increasing f and decreasing H_0 . Especially decreasing H_0 is important for increasing Δp^{\max} .

H_0	H_1	ϕ_0	f	$\langle Q \rangle^{\max}$	Δp^{\max}
100 μm	10 μm	0.1	100 Hz	1.1 $\frac{\text{mL}}{\text{min}}$	1 kPa
100 μm	10 μm	0.1	1000 Hz	9.7 $\frac{\text{mL}}{\text{min}}$	13 kPa
50 μm	10 μm	0.2	1000 Hz	19.5 $\frac{\text{mL}}{\text{min}}$	208 kPa

Table 1: The maximum flow rate $\langle Q \rangle^{\max}$ and back pressure Δp^{\max} as functions of H_0 and f for $H_1 = 10$ μm , $W = 1$ mm, $\lambda = 60$ mm and $\nu = 8.9 \times 10^{-7}$ m²/s (water). The obtained values compare favorably to typical flow rates (0.01 - 5 mL/min) and back pressures (10 - 500 kPa) in micro- and acoustofluidic micro-dosing pumps for drug delivery applications [3].

Conclusion

Travelling-wave micropumps show potential in acoustofluidics even far from occlusion at $\phi_0 = 0.1$. Larger ϕ_0 is obviously better for both $\langle Q \rangle^{\max}$ and Δp^{\max} , and this may be achieved using soft-walled channels and strong mechanical or electromechanical actuators [3]. However, in systems where a large displacement H_1 is unobtainable, decreasing the unperturbed height H_0 could prove crucial in overcoming a large back pressure. As the relative flow-rate oscillation amplitude is large, $Q/\langle Q \rangle \approx 1/\phi_0$, it may be necessary to add an external hydraulic compliance to smoothen out the oscillatory flow. Lastly, we note that the presented analysis can also assist in analyzing how the flow rate and back pressure in peristaltic pumps may be affected by an imperfect occlusion $\phi_0 \lesssim 1$.

Acknowledgments. This work was supported by the PRISMA project funded by the European Union's Horizon EIC Transition Open 2021 Program, Grant No. 101057436.

References

- [1] F. Forouzandeh, A. Alfadhel, A. Arevalo, D.A. Borkholder, *Sens. Act. A. Phys.* **326**, 112602 (2021) [doi]
- [2] M.Y. Jaffrin and A.H. Shapiro, *Annu. Rev. Fluid Mech.* **3**, 13 (1971). [doi]
- [3] A.B. Bußmann, L.M. Grünerbel, *et al.* *Sens. Act. A. Phys.* **330**, 112820 (2021) [doi]

Impact of acoustic scatterer elasticity and frequency on acoustophoresis in a standing wave field

Khemraj Gautam Kshetri¹ and Nitesh Nama¹

¹Department of Mechanical & Materials Engineering, University of Nebraska-Lincoln, USA
E-mail: kgautamkshetri2@huskers.unl.edu

Introduction

Acoustofluidic systems often employ pre-fabricated acoustic scatterers that perturb the imposed acoustic field to realize the acoustophoresis of immersed microparticles [1,2]. We present a numerical study to systematically investigate the acoustic streaming and radiation force fields in the vicinity of a scatterer. We leverage these fields to study the acoustophoresis of immersed particles and identify a critical transition size at which the motion of immersed microparticles shifts from being streaming-dominated to radiation-dominated. We consider different scatterer material to examine the impact of this choice on the streaming and radiation force fields as well as on the critical transition size. Our results reveal significant qualitative and quantitative differences in the streaming and radiation field for different scatterer material choices. These differences lead to a decrease in the critical transition size with an increase in acoustic contrast factor between the scatterer and the surrounding fluid. We also consider a range of acoustic frequencies to reveal that the critical transition size decreases with increasing frequency. Combined, these observations justify the hitherto unexplained choice of acoustic frequencies and scatterer material in previously reported experimental studies [1,2]. Overall, our results not only explain prior experimental results concerning microparticle acoustophoresis in scatterer-based acoustofluidic systems, but also provide a pathway to realize radiation force-based manipulation of small particles by increasing the frequency and acoustic contrast between the scatterer and the fluid.

Numerical Model

We consider a cylindrical scatterer with radius=5 μm placed in a fluid that is subjected to a background standing wave along the y direction (Figure 1). The fluid domain around the scatterer is modeled as being infinite by surrounding it with a perfectly matched layer, and is chosen to be sufficiently large to avoid the impact of outer boundaries on the fluid response around the scatterer. We treat the fluid as a Newtonian fluid and employ the standard perturbation approach to split the fluid variables into their first- and second-order components [3-5]. The solid is modeled as a linear elastic material; therefore, it's response is completely defined by the first-order displacement, which is coupled to the first-order fluid variables. Consequently, the behavior of the system can be studied via a coupled fluid-solid system of equations at the first-order, and the fluid system of equations at the second-order.

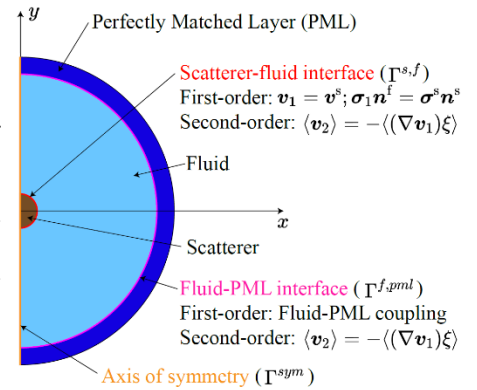


Figure 1: Schematic of the computational domain comprising an acoustic scatterer surrounded by a fluid domain, and a perfectly matched layer, and corresponding boundary conditions.

A major goal of this work is to characterize the impact of scatterer's material properties and acoustic frequency on the motion of immersed microparticles that are often immersed in the fluid domain surrounding the scatterer. Therefore, to characterize the acoustophor-

etic motion of immersed microparticles, we implement a particle tracking strategy by considering a balance of streaming-induced hydrodynamic drag force, and the acoustic radiation force on these particles. This yields the velocity of immersed microparticles as $\mathbf{v}_p = \langle \mathbf{v}_2 \rangle + \tilde{a}^2 \mathbf{v}_{1\mu\text{m}}^{\text{rad}}$, where \tilde{a} denotes the non-dimensional radius of the immersed particle, $\langle \mathbf{v}_2 \rangle$ is the streaming velocity, and $\mathbf{v}_{1\mu\text{m}}^{\text{rad}}$ is the purely radiation-dominated velocity of a particle with reference size 1 μm . Here, the first term on the right-hand side represents the contribution of the streaming to the particle velocity, while the second term represents the contribution from the radiation force. Consequently, following Barnkob *et al.* [5], we define the critical transition size at which $\langle \mathbf{v}_2 \rangle = \tilde{a}^2 \mathbf{v}_{1\mu\text{m}}^{\text{rad}}$. Complete methodological details on numerical implementation will be provided in the presentation.

Results

A. Impact of scatterer material: To characterize the impact of the scatterer material choice on the streaming and radiation fields, we investigate two different choices of scatterer material: glass and Platinum. For the same surrounding fluid (water), these choices yield significant difference in viscous acoustic contrast factor (0.872 for Platinum-water vs. 0.557 for glass-water). Figure 2 shows the resulting radiation and streaming fields. Comparing the radiation force fields for glass (Figure 2A) and Platinum (Figure 2B), an increase in acoustic contrast factor leads to an increase in the radiation force. In contrast, the streaming fields for corresponding cases (Figure 2C and 2D) exhibit a decrease in streaming velocity with increasing contrast factor. In concurrence with these results, the critical transition size decreases with increasing acoustic contrast between the scatterer and the fluid (results not shown here). This trend points to the possibility of realizing smaller critical transition sizes by increasing the acoustic contrast between the scatterer and the fluid. We remark that in addition to glass and Platinum, we have considered several other choices of scatterer material that are not discussed here. A complete discussion of these results will be provided in the presentation.

B. Impact of acoustic frequency: To assess the impact of acoustic frequency on the streaming and radiation fields around the scatterer, as well as on the critical transition size, we consider a $5\ \mu\text{m}$ copper scatterer placed in background acoustic wave fields with two different frequencies: 5 kHz and 1 MHz. We observe that, for a given scatterer-fluid system, an increase in acoustic frequency leads to an increase in the acoustic radiation force and a decrease in the streaming velocity. Accordingly, the critical transition size for a specific scatterer-fluid system decreases with increasing frequency. In line with this observation, Figure 3 shows the trajectories of $5\ \mu\text{m}$ particles at (A) 5 kHz and (B) 1 MHz, where the motion is observed to be streaming-dominated at 5 kHz and radiation-dominated at 1 MHz. These results illustrate that the motion of particles of a specific size can be tuned to be either streaming-dominated or radiation dominated by tuning the acoustic frequency. Further, these results also explain the absence of particle trapping in our prior experimental systems [1] that employ an acoustic frequency of 5 kHz.

Conclusion

We investigated the radiation and streaming fields, and the resulting acoustophoresis, around a scatterer to elucidate the impact of the choice of acoustic frequency and scatterer material on the acoustophoresis of immersed microparticles in the vicinity of a scatterer. We also defined and investigated the critical transition size at which the particle motion transitions from being streaming-dominated to being radiation-dominated. Our numerical results indicate that the choice of acoustic frequency and scatterer material significantly impact the acoustophoresis around the scatterer and reveal a potential pathway to realize manipulation of small particles in scatterer-based acoustofluidic systems by increasing the frequency and the acoustic contrast between the scatterer and the fluid. Our results systematically explain prior experimental results in relation to the choice of specific scatterer material and acoustic frequency [1,2]. The results reported in this presentation will not only provide an augmented understanding of acoustophoresis around a scatterer but will also significantly aid in identifying the optimal design and operational parameters for future experimental studies.

References

- [1] Huang PH, Xie Y, Ahmed D et al. Lab on a Chip **13**(19), 3847-52 (2013).
- [2] Leibacher I, Hahn P, and Dual J. Microfluidics and Nanofluidics **19**(4), 923-933 (2015).
- [3] Nama N, Huang TJ, and Costanzo F. Journal of Fluid Mechanics **825**, 600-630 (2017).
- [4] Baasch T, Pavlic A, and Dual J. Physical Review E **100**(6), 061102 (2019).
- [5] Barnkob R, Augustsson P, Laurell T, and Bruus H, Physical Review E **86**(5), 056307 (2012).

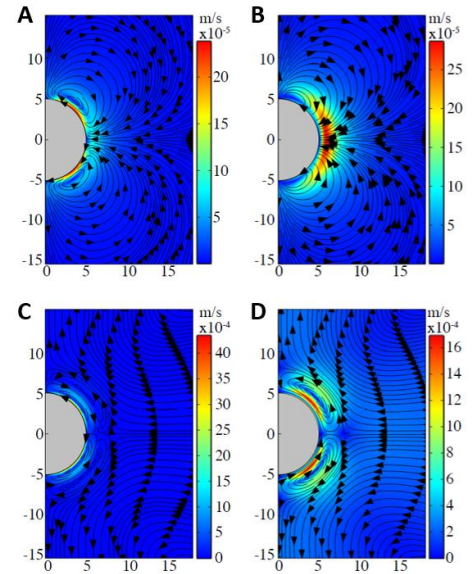


Figure 2: Impact of scatterer material on the radiation dominated velocity $v_{1\ \mu\text{m}}^{\text{rad}}$ and the streaming velocity $\langle v_2 \rangle$ around a $5\ \mu\text{m}$ scatterer surrounded by water and placed at the velocity antinode of the standing wave with an acoustic frequency of 900 kHz. (A, B) plot the radiation dominated velocity when the scatterer material is taken to be (A) glass and (B) Platinum. (C, D) plot the corresponding streaming velocity field. Color legends indicate the magnitude of the respective fields, while the numbers on the axes indicate distances in μm .

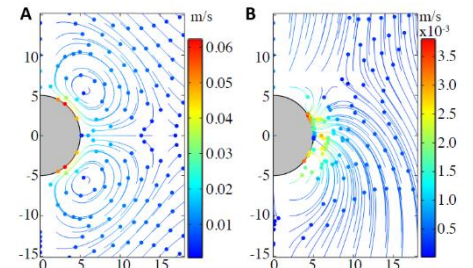


Figure 3: Trajectories of 157 evenly spaced $5\ \mu\text{m}$ polystyrene particles immersed around a copper scatterer for an acoustic frequency of (A) 5 kHz and (B) 1 MHz. The colored discs represent the final position of the immersed particles moving along colored lines. Color legends indicate the magnitude of the particle velocity, while the numbers on the axes indicate distances in μm .

AcouStokes: Framework for multibody acoustophoresis simulations including acoustics, hydrodynamics and contacts

Alen Pavlič^{1,2}, Wei Qiu³, Jürg Dual¹, and Thierry Baasch³

¹Institute for Mechanical Systems, ETH Zurich, Zurich, Switzerland

²California Institute of Technology, Pasadena, CA, USA

E-mail: apavlic@ethz.ch

³Department of Biomedical Engineering, Lund University, Lund, Sweden

Introduction

Acoustophoresis is, for sufficiently large particles, dominated by the acoustic radiation force (ARF). The trajectories of smaller particles can be dominated by the acoustic streaming (AS). When the local particle concentration is high or the particles are close to walls, acoustic interaction forces (AIF) become significant. While the first-order Stokes drag opposes the acoustically-induced motion, the secondary hydrodynamic forces due to the presence of the walls and additional particles either hinder or enhance acoustophoresis. The presence of an externally induced flow in the system exerts additional hydrodynamic forces on the particles. If the particles approach each other or the walls, contacts might emerge, preventing the penetration. The plethora of the described effects featured in multibody acoustophoresis highlight the complexity of such systems and underline the difficulty of their modeling. [1, 2]

Here, we present an open-source computational framework AcouStokes that combines the aforementioned forces in a Matlab-based time-stepping algorithm capable of simulating the complex dynamics of multibody systems undergoing acoustophoresis.

Overview of the computational framework

The AcouStokes framework is based on the low-Reynolds-number Stokesian-dynamics algorithm (SD) of Durlinsky, Brady and Bossis [3], extended to accommodate discrete wall patches [4]. SD predicts velocities of all the spherical particles in the system, based on their positions, fluid properties, and externally applied forces, torque and flow. The algorithm includes the far-field many-body hydrodynamic particle-particle and particle-wall interactions, as well as the near-field particle-particle lubrication interactions.

The external forces that are supported in the current version of AcouStokes are the ARF, the AIF, the gravitational force and particle-particle/particle-wall rigid contact forces. The supported flows include Poiseuille flows between two infinite plates and through a rectangular cross-section, and pure shear flow.

For a 1D plane standing wave (SW), the ARF is modeled according to Yosioka and Kawasima [5], while the AIF is computed according to Silva and Bruus [6]. For an exemplary SW acoustic field, the corresponding device is represented with a fluid cavity of a rectangular cross-section of width w and height h , with the coordinate system defined in Fig. 1a. The walls for the hydrodynamic effects and contacts are optionally placed at $y = \pm w/2$ and $z = \pm h/2$.

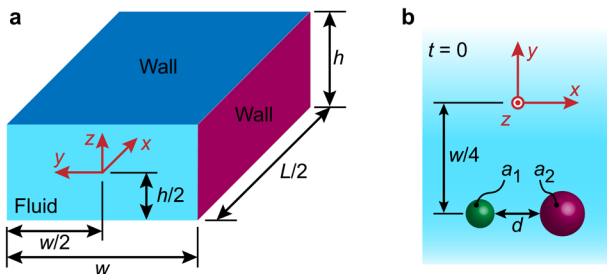


Figure 1: (a) The geometry of a rectangular fluidic cavity within which a SW is imposed along the y -axis. The origin of the Cartesian coordinate system (x, y, z) is positioned at the center of the cavity. (b) The initial configuration of particles used for the exemplary studies. Particle 1 (green) and particle 2 (violet) with radii a_1 and a_2 , respectively, are at a surface-to-surface distance of d , positioned at $y = -w/4$ and $z = 0$.

Results

To demonstrate the capabilities of AcouStokes, we use a simple example of acoustic focusing of two spheres in a SW in water at a 300 kPa pressure amplitude and the frequency of 2 MHz (acoustic wavelength $\lambda = 750 \mu\text{m}$), corresponding to the $\lambda/2$ mode in an acoustically-hard channel of $w = 375 \mu\text{m}$, typical for acoustofluidic devices, with $h = 150 \mu\text{m}$. For the hydrodynamic walls, we assume the length of the channel L to be $\geq 375 \mu\text{m}$. The spheres are initially positioned as shown in Fig. 1b, at $y = -w/4$ and $z = 0$, while x is defined by the surface-to-surface spacing d . In Fig. 2, we study how the presence of the second particle (2)

affects the acoustophoresis of the polystyrene particle (1) with $a_1 = 5 \mu\text{m}$. Specifically, we study the trajectory of particle 1 in a fixed time of 0.08 s for different proximities, sizes and materials of particle 2. A similar configuration was recently featured in a method for the measurement of AIF [7]

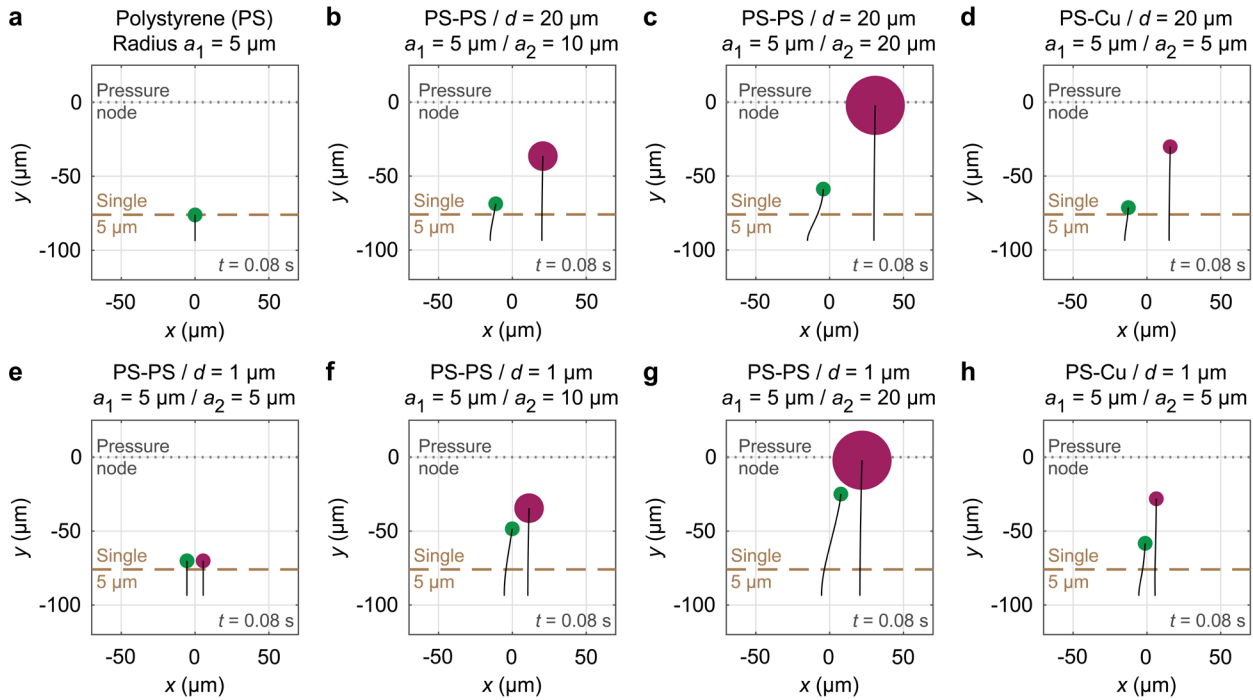


Figure 2: Analysis of acoustic focusing in a SW in water with AcouStokes. The trajectories correspond to the fixed time span of $0 \leq t \leq 0.08$ s. The dashed line (Single 5 μm) represents the reference end position of an isolated polystyrene sphere with $a = 5 \mu\text{m}$ from (a) in equivalent conditions (with the hydrodynamic effects of the walls included). (b)-(d) Show the results for the initial spacing of $d = 20 \mu\text{m}$, whereas (e)-(h) correspond to $d = 1 \mu\text{m}$. The materials of particle 1 (green) and particle 2 (violet) are defined in each of the insets, covering polystyrene (PS) and copper (Cu). The particle outlines are indicating their position at $t = 0.08$ s. The gravity and external flow are neglected for the sake of simplicity.

The results in Fig. 2 illustrate how the trajectory of particle 1 can be drastically affected by the presence of the second particle, when compared to the corresponding single-particle path shown in Fig. 2a. The increase is especially pronounced for close interparticle distance and large size of particle 2 (e.g. Fig. 2g). The “pull” by particle 2 is in the featured cases mainly of hydrodynamical origin, since the inviscid interparticle AIF is of repulsive nature along the y -direction [6].

Conclusion

The presented results concern a very basic configuration of two particles, but nevertheless indicate exciting and interesting behaviour that can be studied with AcouStokes. The framework can, without any extensions, model much larger assemblies of hundreds of particles in fully three-dimensional configurations.

As a tool, AcouStokes enables theoretical investigation of the dynamic phenomena involved in the multibody acoustophoresis. It can aid the design of novel acoustofluidic devices or optimization of operating parameters of existing systems. Furthermore, AcouStokes can be fed the initial particle configurations from experiments, and used to measure the amplitude and distribution of acoustic fields [8] more accurately, or improve the acoustophoresis-based assessment of material properties of, for example, biological cells [9].

AcouStokes is open-source and developed to be user-friendly and extendable to materials, particle sizes, device geometries, acoustic fields and external flows of practical relevance.

References

- [1] Baasch, T., Leibacher, I., & Dual, J. The Journal of the Acoustical Society of America, **141**(3), 1664-1674 (2017).
- [2] Barnkob, R., Augustsson, P., Laurell, T., & Bruus, H. Physical Review E, **86**(5), 056307 (2012).
- [3] Durlofsky, L., Brady, J. F., & Bossis, G. Journal of Fluid Mechanics, **180**, 21-49 (1987).
- [4] Durlofsky, L. J., & Brady, J. F. Journal of Fluid Mechanics, **200**, 39-67 (1989).
- [5] Yosioka, K., & Kawasima, Y. Acta Acustica united with Acustica, **5**(3), 167-173 (1955).
- [6] Silva, G. T., & Bruus, H. Physical Review E, **90**(6), 063007 (2014).
- [7] Saeidi, D., Saghafian, M., Haghjooy Javanmard, S., Hammarström, B., & Wiklund, M. The Journal of the Acoustical Society of America, **145**(6), 3311-3319 (2019).
- [8] Barnkob, R., Augustsson, P., Laurell, T., & Bruus, H. Lab on a Chip, **10**(5), 563-570 (2010).
- [9] Hartono, D., Liu, Y., Tan, P. L., Then, X. Y. S., Yung, L. Y. L., & Lim, K. M. Lab on a Chip, **11**(23), 4072-4080 (2011).

Design of bimorph transducer for high-throughput gene editing

Mohammad Albuhsin^{1,2}, Mugdha Sinha^{1,2}, Jahir Islam¹, J. Mark Meacham^{1,3}, and Michael M. Binkley¹

¹OpenCell Technologies, Inc., St. Louis, MO 63110, USA

²Department of Biomedical Engineering, Washington University in St. Louis, St. Louis, MO 63130, USA

³Department of Mechanical Engineering and Materials Science, Washington University in St. Louis, St. Louis, MO 63130, USA

Introduction

As the fields of immuno-oncology and cell/gene therapy expand to accommodate clinical volumes for autologous and allogeneic CAR-T cell production, throughput and the reliability of intracellular payload delivery processes need to increase. One novel method of payload introduction is the use of acoustic shear poration (ASP) to locally disrupt the cell membrane resulting in 100 to 150-nm sized pores through which payloads can passively diffuse into the cell or be actively driven using an external field. Such pores, which remain open for tens of seconds to minutes, can be exploited for delivery of small (fluorescent dyes) to large (DNA) molecules, or even nanomaterials like liposomes, in continuous flow operation. We have shown that this non-contact method of intracellular delivery retains high cell viability (>80%), while achieving comparable transfection efficiency to that of commercial electroporation systems (e.g., Eppendorf Multiporator and Lonza Nucleofector) [1,2]. The ASP technology comprises two main modules: a transducer and a micronozzle array (MNA). In earlier embodiments, the MNA was fixed in a small-volume cartridge for bench-scale processing of ~1 mL batches in ~30 s. Here, we introduce a new configuration, POROS Giga, that can operate in continuous flow at vastly increased sample throughput of up to 50 mL/min (Fig. 1A-C).

We first describe the use of finite element analysis (FEA) to simulate the behavior of a bimorph transducer for the ejection of cell suspensions. Results of computational models were used to guide the down-selection of possible transducer designs to two, which were fabricated for experimental flowrate testing. The bimorph design, with a lead zirconate titanate (PZT-8) element bonded to the inner surface of a hollow anodized aluminum cylinder, was selected as the optimal shape to eliminate direct contact with the fluid sample and simplify cleaning between runs. For experiments, the MNA was etched in a 200- μm thick fused silica sheet. Nozzles were cones with orifice diameters of 40 μm . The conical taper was used to focus the flow prior to ejection, and sharp-edged orifices reduced pressure drop, facilitating low-power sample atomization. The bimorph was positioned above the MNA slightly submerged in a sample reservoir that was continuously refreshed using a syringe pump (Fig. 1C). Devices operated at tens to hundreds of kHz, relying on transducer modes (vs. previous chamber modes) to drive sample ejection from the MNA. This study scales previously reported devices—from an MNA with 32 nozzles to 340 nozzles—to achieve treatment of clinically relevant volumes of cells with consistent, repeatable operation.

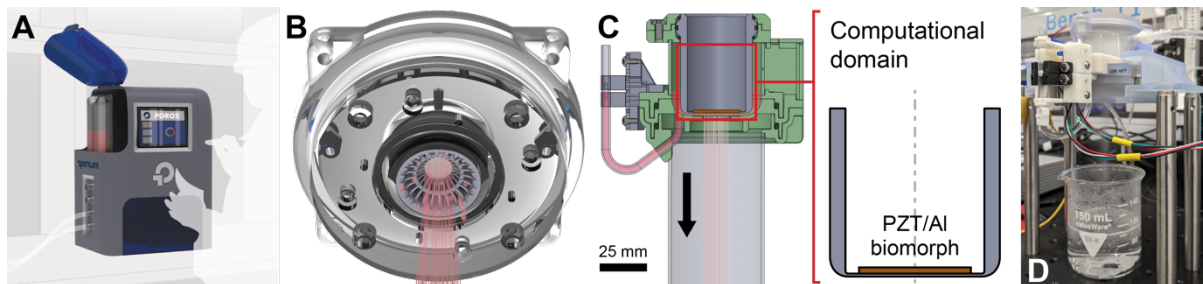


Figure 1: POROS Giga cell transfection and payload delivery platform. (A) and (B) Renderings of system and acoustic shear poration (ASP) module in development. (C) System cross section highlighting the FEA computational domain. (D) Experimental setup shown ejecting DI water at 30 mL/min.

Methods

We used FEA (COMSOL Multiphysics 5.6) to simulate possible design configurations to reduce the number of experimental prototypes. Five parameters were varied: wall thickness (t_{wall}), aluminum isolation layer thickness (t_{al}), transducer thickness (t_{trans}), bimorph curvature (BM_{curv}), and transducer radius (r_{trans}). Aluminum isolation layer radius was determined from the fixed overall diameter of the aluminum cylinder and t_{wall} . A 2D

section of the circularly symmetric assembly was modeled. t_{wall} and t_{al} were identified as most critical to device operation, and a parametric sweep was performed for both wall and isolation layer thickness of 0.5–4.5 mm in 0.25 mm step sizes (operating frequency range 15 to 100 kHz; constant voltage across the PZT). Displacement at the midline of the transducer and mode shape were used to optimize geometry for fluid ejection from the device. Optimal cylinder designs were manufactured in aluminum by Veranex Solutions, Inc. (Providence, RI). A 25-mm diameter, 1.5-mm thick PZT-8 piezoceramic (APC International, PA) was bonded inside the cylinder using a two-part epoxy cured at 60 °C overnight.

Experimental prototypes were assessed on two factors: duration of operation and flowrate at operating frequency. Experimental operating frequency was found by scanning a 15 kHz range about the FEA-predicted frequency using a 1 kHz step size. Assembled bimorph transducers were actuated using a PDUS210 ultrasonic driver (PiezoDrive, AU). The bimorph and MNA were held in a 3D-printed fluid reservoir (max volume 50 mL) (Fig. 1C,D). To prevent damping of the transducer during operation, the fluid level height was set to 10 mm above the MNA and kept constant throughout ejection using a syringe pump. The applied power and flowrate were measured during device characterization.

Results

Average displacement was used to compare performance with different aluminum isolation layer thicknesses and to identify an optimal design for final prototypes (Fig. 2A,B). While $t_{\text{al}} = 0.5$ mm offered the highest relative displacement, $t_{\text{al}} = 0.75$ mm was selected due to practical thermal management and manufacturing considerations. An operating frequency of 98 kHz was predicted by the COMSOL model as the most optimal (Fig. 2A). Eigenmode shape and resolved stress profile indicated that the pumping motion of the bimorph design was enhanced at this condition to increase atomization and peak flowrate. The measured orifice diameter of the MNA (FemtoPrint, SA) was 39.8 ± 0.3 μm , closely matching the desired geometry. Slight imperfections due to the laser width were found on the fluid reservoir side and near the proximity of the orifice, but these did not influence spray characteristics (not shown). Assembled devices were analyzed for spray characteristics. Experimental operating frequency (f_{ex}) was found to be 95.8 kHz, closely matching the model prediction. Results for the $t_{\text{al}} = 0.75$ mm bimorph are shown in Fig. 2C. Flowrate vs. power followed a nonlinear trend, reaching a maximum of 50 mL/min before overheating. The prototype device sustained a flowrate of 50 mL/min for 3 min, for a total treated volume of 155 mL.

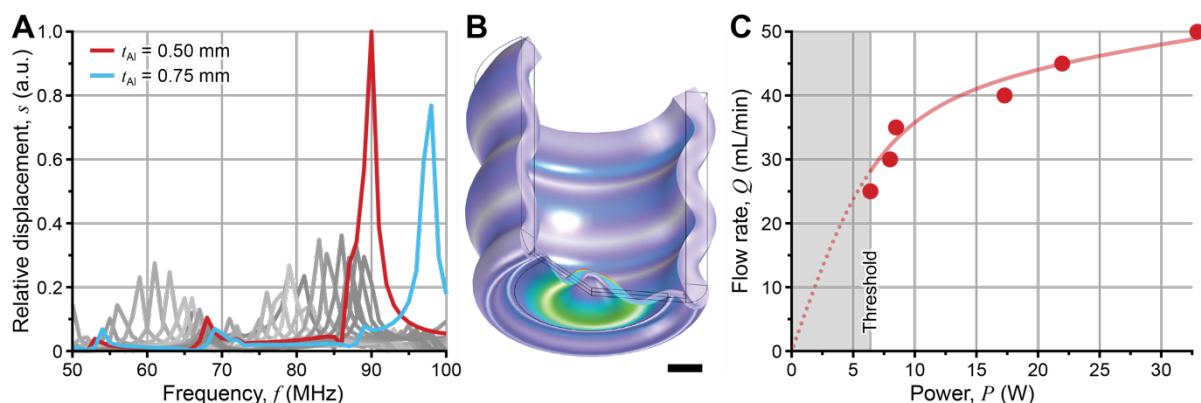


Figure 2: Computational and experimental assessment of modified bimorph transducer design used in an ASP-based platform for effective intracellular delivery and transfection. (A) Model-predicted relative displacement vs. frequency for two bimorph designs. Best performing geometry are $t_{\text{al}} = 0.5$ mm and $t_{\text{al}} = 0.75$ mm are shown in red and blue, respectively. (B) Predicted displacement field for $t_{\text{al}} = 0.75$ mm at frequency corresponding to maximum displacement ($f_{\text{op}} = 98.0$ kHz). Scale bar is 5 mm. (C) Measured flowrate as a function of applied power to the bimorph transducer under optimal operating conditions ($f_{\text{ex}} = 95.8$ kHz).

Conclusion

Herein, we have shown successful optimization of a bimorph transducer design for atomization of fluids including use in acoustic shear poration to achieve efficient cell and gene therapy. Numerical simulations were used to estimate peak displacement to select geometry for functional prototypical designs. Models were validated by comparing observed experimental operating frequency with FEA predicted values.

An optimized system was able to maintain 50 mL/min ejection for sustained operation, treating >150 mL in 3 min. Flowrate through the device was non-linearly related with power input to the transducer. Ongoing work is focused on characterization for cell and gene therapy, payload introduction, and cell modification to compare POROS Giga performance to previous cartridge-based systems.

References

- [1] J. M. Meacham, K. Durvasula, F. L. Degertekin and A. G. Fedorov. *Sci. Rep.*, 2018, **8**, 1-10.
- [2] J. M. Meacham, K. Durvasula, F. L. Degertekin and A. G. Fedorov. *J. Lab. Autom.*, 2014, **19**, 1-18.
- [3] A. D. Ledbetter, H. N. Shekhani, M. M. Binkley and J. M. Meacham. *IEEE Trans. Ultrason. Ferroelectr. Freq. Control*, 2018, **65**, 1893-1904.

Microscale characterization of a versatile ultrasonic droplet generator

Hongyu Bai¹, Li Shan^{1,2}, and J. Mark Meacham¹

¹Department of Mechanical Engineering and Materials Science, Washington University in St. Louis, St. Louis, MO 63130, USA

E-mail: bhongyu@wustl.edu, meachamjm@wustl.edu; Web: <https://meachamlab.wustl.edu>

²Department of Mechanical Engineering, University of Texas at Dallas, Richardson, TX 75080, USA

Introduction

Controllable, uniform droplet generation is critical to many industrial processes and biomedical applications (e.g., materials synthesis, fuel combustion, cell handling, and aerosol drug delivery). We have previously described a micromachined ultrasonic atomizer capable of producing sprays with microdroplets in the ~ 3 to $50\text{-}\mu\text{m}$ diameter range while operating at frequencies from ~ 0.5 to 2.5 MHz [1,2]. A bulk piezoelectric transducer generated a standing acoustic pressure wave that drove ejection of droplets or continuous jets from an array of microscopic orifices. While the device was demonstrated with a variety of working liquids from low surface tension fuels to viscous polymers, these systems were limited to operation at a small number of longitudinal resonances dictated by the fixed reservoir geometry. We recently introduced a new system configuration with a continuously variable liquid reservoir height for dynamic adjustment of the operating parameters [3]. A combination of computational modeling and macroscale experiments confirmed our earlier understanding of the system harmonic response. In addition, we investigated how the interplay of longitudinal and lateral resonances affected the spray uniformity from a 13×13 -nozzle microarray. We concluded that certain resonances lead to variability in the pressure gradient at the orifices, which may affect the droplet size distribution; however, no droplet size measurements were performed. Here, we introduce a new device configuration that allows high-resolution stroboscopic imaging of the air-liquid interface evolution at each orifice (Fig. 1). Although the entire micronozzle array remains acoustically active, we use orifice size to control the flow resistance, restricting ejection to a single preselected orifice (Fig. 1b,c). In this way, we relate ejection uniformity to orifice size, operating frequency, and drive amplitude, observing ejection regimes that resemble classical descriptions of droplet/jet breakup (Rayleigh, wind-induced, and atomization).

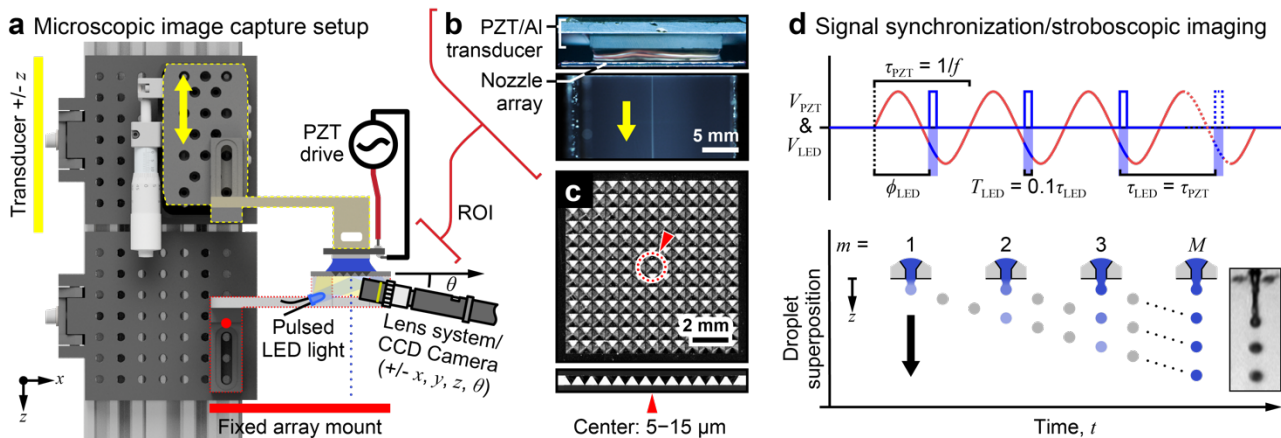


Figure 1: Ultrasonic droplet generator microscale characterization setup. (a) Schematic overview illustrating the configuration of system components. (b) PZT/Al transducer and microarray assembly, and (c) microarray design for ejection from a single active orifice of the larger microarray. (d) Actuation and LED signal synchronization for stroboscopic imaging of the air/liquid interface evolution during droplet/jet ejection.

Experimental

Imaging ejection events from a single orifice was difficult using the earlier microarrays due to obstruction by droplets/jets originating from adjacent orifices. To isolate the target orifice, only that orifice was created with the size of interest (e.g., $5\text{--}15\ \mu\text{m}$), and the diameter of all other nozzles was reduced to $\sim 1\ \mu\text{m}$ to suppress ejection (Fig. 1b). Pyramidal nozzles were fabricated using a combination of photolithography, reactive ion etching (RIE) through a nitride masking layer, and anisotropic wet etching in 45% w/w potassium hydroxide (KOH) with 10% isopropyl alcohol at $75\ \text{C}^\circ$. The array of squares used to define the KOH etch was designed

to ensure that the etch terminated $\sim 10\ \mu\text{m}$ from the backside of the wafer. The wafer was then inverted, and orifices were located at the nozzle tips using a combination of RIE and deep reactive ion etching (DRIE).

The experimental setup comprised the droplet generator, the imaging and illumination system, and signal generation/synchronization (Fig. 1). The nozzle array was fixed in place below a 1.5-mm thick lead zirconate titanate (PZT) element bonded to a 2-mm thick aluminum coupling layer. The transducer was mounted to a z-translation stage allowing adjustment of the distance between the transducer and microarray (i.e., the liquid reservoir height). A pulsed light emitting diode (LED) was synchronized with the ejection waveform to achieve an effective framerate of ~ 10 million fps (Fig. 1d; ~ 10 frames per period are required to describe the ejection cycle). Ejection was driven by an amplified sinusoidal signal to the PZT. Note that captured images represent the superposition of thousands of identical ejection events.

Results and discussion

The microscale image capture platform enables detailed characterization of the air-liquid interface evolution during droplet and jet ejection from a target nozzle. To demonstrate these capabilities, we investigated the droplet size as a function of operating frequency using a 5- μm diameter orifice located at the center of the microarray. For the range 0.5 to 2.0 MHz, droplet diameter was found to decrease with increasing frequency as $d \sim f^{-0.33}$ (Fig. 2a), which matches accepted theoretical predictions [1]. We then demonstrated a new capability to investigate how drive amplitude affects the mode of droplet ejection. After initiating droplet production at a threshold waveform generator amplitude of 100 mV, the drive voltage was gradually increased to 140 mV in 10 mV steps (Fig. 2b; the amplified voltage was not measured but would be significantly higher). As expected, droplet velocity increased (from ~ 14 to 28 m/s). However, the increase in momentum also seemed to promote a more chaotic breakup process with the appearance of satellite droplets (see yellow arrow in Fig. 2b), as well as a twist that resembled the classical wind-induced droplet breakup regime.

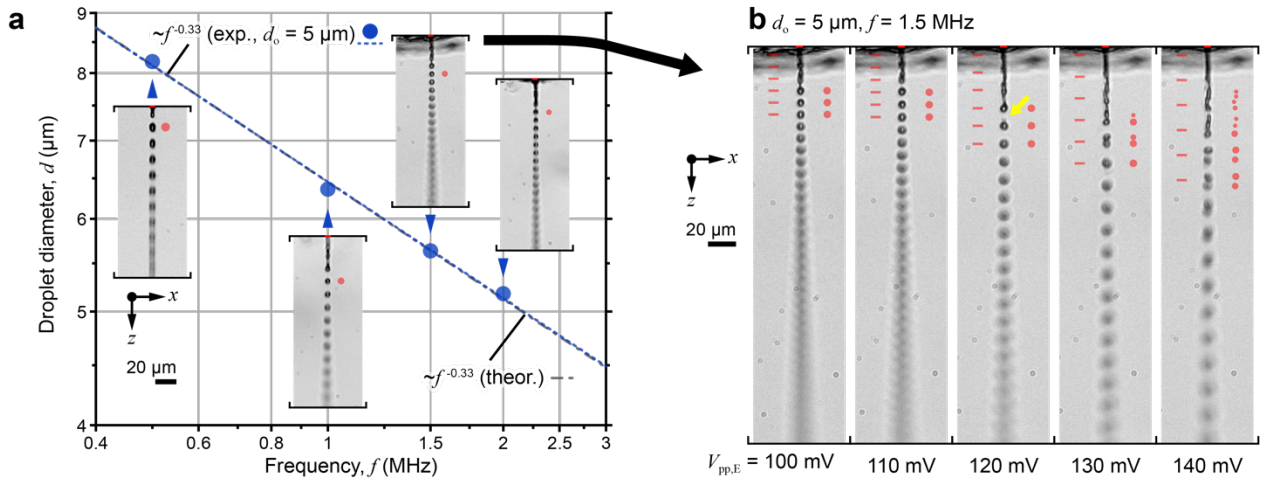


Figure 2: Stroboscopic imaging enables parametric investigation of droplet ejection. (a) Droplet size as a function of operating frequency for a microarray with 5 μm orifices driven from 0.5 to 2.0 MHz at the threshold amplitude for droplet production. (b) Evolution of droplet breakup as a function of drive amplitude for a 5 μm orifice driven at 1.5 MHz.

Conclusion

We introduce a new experimental setup that enables high-resolution imaging of droplet/jet production from an ultrasonic droplet generator with continuously variable operating frequency and drive amplitude. Operating frequency is varied by adjusting the transducer up or down relative to a nozzle microarray, providing real-time control over droplet size within a range dictated by the orifice size. In addition, orifice size is used to isolate a single active orifice. For the first time, we observe how droplet production changes with increasing drive voltage without obstruction from inactive nozzles. Ongoing work is focused on developing a regime map that can be used to predict breakup regimes (Rayleigh, wind-induced, and atomization) based on orifice size, operating frequency, and drive amplitude.

References

- [1] J. M. Meacham, M. J. Varady, F. L. Degertekin and A. G. Fedorov, *Phys. Fluids*, 2005, **17**, 100605.
- [2] J. M. Meacham, A. O'Rourke, Y. Yang, A. G. Fedorov, F. L. Degertekin and D. W. Rosen, *J. Manuf. Sci. Eng.*, 2010, **132**, 030905.
- [3] L. Shan, M. Cui and J. M. Meacham, *J. Acoust. Soc. Am.*, 2021, **150**, 1565-1576.

Integrated Transparent Surface Acoustic Wave Technology for Active De-Fogging and Icing Protection on Glass

Hui Ling Ong¹, Luke Haworth¹, Jikai Zhang¹, Prashant Agrawal¹, Hamdi Torun¹, Qiang Wu¹, and Yong-Qing Fu^{1,*}

¹Faculty of Engineering and Environment, Northumbria University, Newcastle upon Tyne, NE1 8ST, UK
E-mail: huiling.ong@northumbria.ac.uk / h.l.ong@northumbria.ac.uk

*Corresponding Authors: Prof. Richard YongQing Fu, E-mail: Richard.fu@northumbria.ac.uk

Introduction

There have been great concerns on fogging, condensation, icing, and frosting formation on glass surfaces, which leads to poor visibility and hazardous issues in various applications such as lenses, windshields, windows of vehicles/airplane/helmet, and solar panels [1]–[5]. Passive and active methods have been demonstrated to combat surface accretions induced by fogging, icing and/or frosting. There have been several existing approaches implemented for the eradication of fogging. The techniques utilized to remove fogging generally require external energy, including external heating, dynamic perturbation method (or mechanical mixing method), seeding hygroscopic particles, and utilizing refrigerants which are harmful to the environment. These methods of eliminating fogging tend to consume huge amounts of energy, and pose as a pollution issue [6], [7]. Moreover, one of the key passive anti-icing methods is to reduce surface energy of the solid surface and decrease water-ice adhesion using superhydrophobic and icephobic surfaces [8]. Although superhydrophobic surfaces with a large contact angle can significantly delay the droplet freezing when compared to those on hydrophilic surfaces, these superhydrophobic surfaces often have poor mechanical/adhesion properties and durability issues [8]. Additionally, utilizing functionally treated surfaces for ice mitigation does not appear to reduce ice adhesion or increase icing protection. Due to these issues, there have been studies to investigate other methods such as surface acoustic waves (SAWs), which cause effective nanoscale vibration and acousto-thermal effects to allow fog/ice interface to break, localized melting, and ice separation from glass substrate. As illustrated in Figure 1, at the localized area where the fog or ice is being accumulated, SAWs can be utilized along with surface hydrophobic treatments to combat surface accretions and fog/ice elimination at different SAW RF powers, frequency, and acousto-thermal effects.

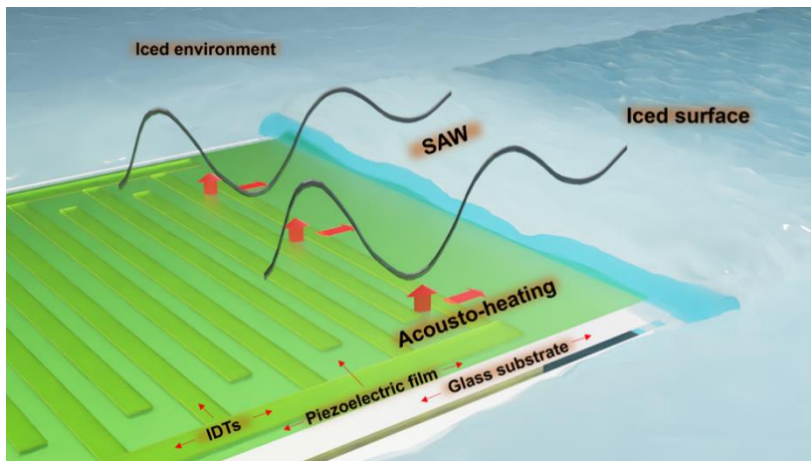


Figure 1: Illustration of structural design of thin film-based SAW device integrated onto glass substrate

SAW acoustofluidics device and characterization

In this work, ZnO thin film was deposited onto glass substrate, and SAW devices were fabricated via lithography technique. The SAW devices exist in different wave modes such as Rayleigh, Sezawa, and higher order wave modes. Based on the velocity of the substrate material, the wavelength can be determined at different frequency. To promote efficient icing and fogging efficiency during operation with SAW agitations, the SAW devices were treated with a hydrophobic fluoropolymer, CYTOP. The ZnO/glass SAW devices were explored for active icing and fogging based on the evaluation of RF powers, frequency, and acousto-thermal effects. Experimental studies have shown that due to strong localized vibrations and acousto-thermal effect at the ice/glass interface during SAW agitation, formation of the ice can be observed to delay significantly and ice formation on the SAW devices are efficiently removed. With the addition of CYTOP to the SAW device surface, the time required for active anti-icing and de-icing at different RF powers were affected, prompting the hybrid ice mitigation with CYTOP treatment.

Demonstration on active anti-icing, de-fogging and droplet de-icing

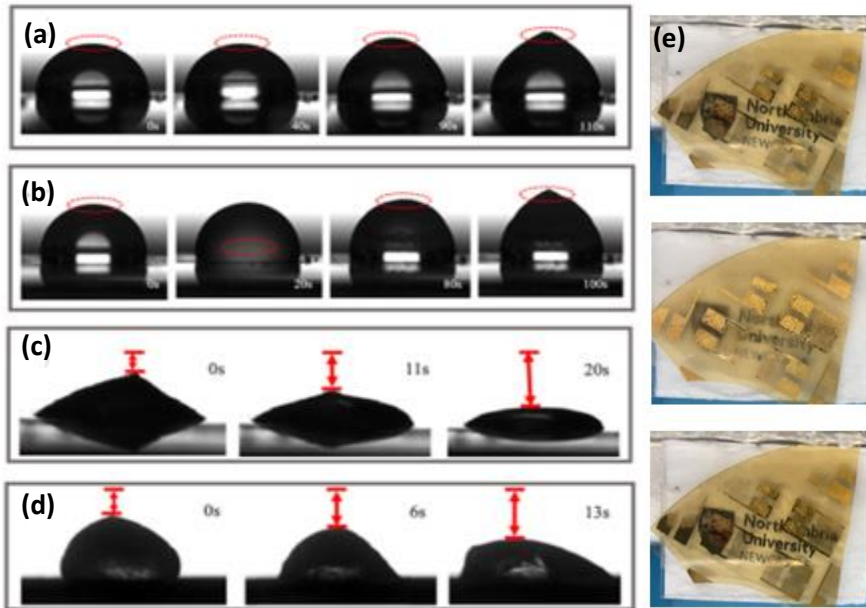


Figure 2: Droplet freezing on ZnO/glass SAW device on (a) untreated surfaces, (b) CYTOP treated surfaces; De-icing on ZnO/glass SAW device (c) without CYTOP treatment, (d) with CYTOP treatment; (e) Illustration of de-fogging process

Active anti-icing, de-fogging, and droplet de-icing demonstrations were conducted using the SAW devices, with the ice/condensates being placed in front of the IDT area. Figures 2(a) and 2(b) show examples of the droplet freezing process. Droplet freezing was first conducted on untreated ZnO/glass SAW device, without using SAW energy. The captured shape evolutions of the droplet during glaze icing are shown in Figure 2(a), where icing is shown to occur after ~19 seconds. The snapshots at different time frames depict that the freezing front tip moves upwards and the remaining part of water droplet which was not frozen remains a spherical shape. At a time of ~80.9 s, the ice expands vertically and pushes against the spherical cap of the liquid water droplet. With the addition of confining effect of surface tension, it leads to the pointy tip as seen at ~91.4 s. Droplet freezing was then conducted on ZnO/glass SAW device which was surface treated with CYTOP but without applying any SAW power, and the obtained results are shown in Fig. 2(b). At the same testing conditions, glaze icing was observed to start to form at ~42.3 seconds, with frozen phenomena like those of untreated ZnO/glass SAW device, and ice crystal was formed after ~109 seconds. It was observed that with the implementation of hydrophobically treated CYTOP layer, the droplet freezing was delayed compared with the untreated samples.

Figures 2(c) show the de-icing results for glaze ice using the ZnO/glass SAW devices. On the untreated device surface, there were changes in the ice shapes when the SAW was applied, which can be due to the introduction of strong localized vibrations and acousto-thermal effect at the ice/glass interface due to the SAWs. During the deicing process, tiny cracks could be generated at the solid/ice interfaces and the growth of these cracks were increased with the continuous SAW agitations. Due to the formation and propagation of cracks, the mechanical adhesion of ice to the glass surface is weakened. Simultaneously due to the localized acousto-thermal effect, ice at the interface also starts to become partially melted before it further becomes liquid.

Figures 2(d) shows the shape evolution of clear ice with CYTOP when the SAW power was applied, and the obtained phenomena are like those illustrated in Figures 2(c). By applying the layer of CYTOP in Figure 2(d), the time taken to de-ice was reduced. This further suggests that surface treatment with CYTOP helps to promote the de-icing performance.

Demonstration on rime ice de-icing

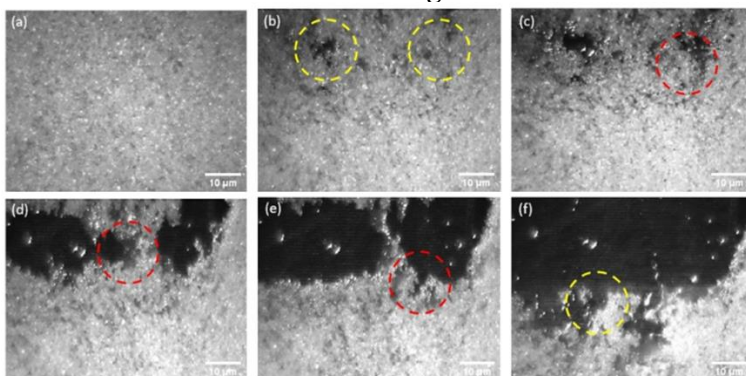


Figure 3: Rime ice de-icing process of ZnO/glass SAW device at (a) 0 s, (b) 5.912 s, (c) 6.868 s, (d) 8.420 s, (e) 10.988 s, (f) 34.040 s

Figures 3(a) to 3(f) illustrate the rime ice de-icing process on the ZnO/glass SAW device which was treated with CYTOP. The morphology of the rime ice was observed to be solid, porous, and loosely attached to the surface as shown in Figure 3(a). When RF powers are applied, the mechanical vibrations from the SAW acoustic energy damage the interface of the rime ice clusters with substrate, which leads to the change in the microstructures of the porous rime ice and its morphology as shown in Figure 3(b). Due to the significant vibrations at the interface, additional new areas of rime ice removal are generated as depicted in Figure 3(c). Other than the mechanical vibrations from the applied RF power, interfacial localized heating (acoustic thermal effect) is also induced on the ZnO thin film due to SAW energy dissipation, and this can be observed in Figure 3(d). This will eventually lead to the shrinkage and removal of the porous rime ice as observed in Figure 3(e). As time progresses, multiple porous rime ice will continue to shrink and be removed, which fulfills the de-icing process as a result from SAW agitations and acousto-thermal effect as depicted in Figure 3(f).

Conclusion

ZnO thin film on glass SAW device was fabricated and then used to perform de-fogging, active anti-icing, and de-icing. Different RF strengths were used to assess the efficacy of de-fogging and icing concerns. When the SAW devices were exposed to humid air flow, the de-fogging time was drastically reduced when the SAW powers were increased. Due to intense localized vibrations and acousto-thermal action at the ice/glass interface during SAW operation, formation of the ice has been significantly delayed and both clear ice and rime ice generated on the SAW devices have been efficiently removed. Furthermore, the addition of CYTOP to the SAW surface affects the time required for active anti-icing and de-icing at different RF strengths, prompting hybrid ice mitigation with the CYTOP treatment.

References

- [1] K. Kasahara, T. Waku, P. W. Wilson, T. Tonooka, and Y. Hagiwara, "The Inhibition of Icing and Frosting on Glass Surfaces by the Coating of Polyethylene Glycol and Polypeptide Mimicking Antifreeze Protein," *Biomolecules*, vol. 10, no. 2, Feb. 2020, doi: 10.3390/BIOM10020259.
- [2] L. Tian, Z. Zhang, X. Jiang, L. Shu, J. Hu, and H. Qin, "Study on the Icing Accretion Characterization of Porcelain and Glass Insulator," *ICHVE 2018 - 2018 IEEE Int. Conf. High Volt. Eng. Appl.*, Feb. 2019, doi: 10.1109/ICHVE.2018.8642201.
- [3] X. Du, Z. Yang, Z. Jin, Y. Zhu, and Z. Zhou, "A numerical prediction and potential control of typical icing process on automobile windshield under nocturnal radiative cooling and subfreezing conditions;," <https://doi.org/10.1177/0954407019875356>, vol. 234, no. 5, pp. 1480–1496, Sep. 2019, doi: 10.1177/0954407019875356.
- [4] A. Ene and C. Teodosiu, "Studies dealing with defogging and de-icing phenomena on vehicles' windshield: A review," *IOP Conf. Ser. Earth Environ. Sci.*, vol. 664, no. 1, May 2021, doi: 10.1088/1755-1315/664/1/012071.
- [5] I. R. Durán, J. Profili, L. Stafford, and G. Laroche, "Unveiling the origin of the anti-fogging performance of plasma-coated glass: Role of the structure and the chemistry of siloxane precursors," *Prog. Org. Coatings*, vol. 141, p. 105401, Apr. 2020, doi: 10.1016/J.PORGCOAT.2019.105401.
- [6] C. Liu, Z. Tian, Y. Zhao, and X. Zeng, "Review and prospect of fog elimination technology based on acoustic condensation," *IOP Conf. Ser. Earth Environ. Sci.*, vol. 514, no. 3, Jul. 2020, doi: 10.1088/1755-1315/514/3/032011.
- [7] C. Liu, Y. Zhao, Z. Tian, and H. Zhou, "Numerical Simulation of Condensation of Natural Fog Aerosol under Acoustic Wave Action," *Aerosol Air Qual. Res.*, vol. 21, 2003, doi: 10.4209/aaqr.2020.06.0361.
- [8] K. Xu, J. Hu, L. Shu, X. Jiang, and Z. Huang, "Influence of hydrophobicity on ice accumulation process under sleet and wind conditions," *AIP Adv.*, vol. 8, p. 35113, 2018, doi: 10.1063/1.5022422.

Dynamic Droplet Impact under Acoustic Waves: Surface Inclination, Hydrophobic Coatings and Non-Newtonian Liquids

Luke Haworth¹, Mehdi Biroun², Prashant Agrawal¹, Hamdi Torun¹, Glen McHale³ and Richard YongQing Fu¹

¹ Faculty of Engineering and Environment, Northumbria University at Newcastle, NE1 8ST, UK

² Department of Chemical Engineering, University College London, London, WC1E 7JE, UK

³ Institute for Multiscale Thermofluids, School of Engineering, University of Edinburgh, EH9 3FB, UK

Introduction

Controlling the behaviour of droplet impact holds immense importance across various fields, including anti-icing, anti-fouling and inkjet printing [1, 2]. Generally, passive methods such as surface treatments and coatings have been used in the literature to alter the droplet impact characteristic parameters such as impact regime and contact time. Textured surfaces, superhydrophobic coating, and liquid-infused coatings are examples of these passive methods [3, 4]. Recently, active methods such as applying magnetic fields to the impact region, surface vibration, and surface acoustic waves (SAWs) have been used to control droplet impact onto surfaces [5-7]. In this study, we focus on combining these active (using SAWs) and passive (nature-inspired surface coatings) methods to introduce a more effective method to alter and control the droplet impact on the surface. The active method allows controlling and modifying the impact dynamics in real-time and on demand, and the passive method (i.e., surface treatment) helps to design the surface effectively. For instance, in a particular scenario requiring reduced contact time, utilising either a superhydrophobic or liquid-infused coating would markedly serve the design purpose [8]. Besides, since liquids are non-Newtonian with complex rheologies in most microfluidics applications, we investigate the effect of liquid rheology on the impact dynamics.

Results and discussion

Effect of Surface Coatings with SAW

Firstly we combined the active SAW method using propagating waves and a passive hydrophobic polymer-coated surface for altering impact regimes (Figure 1(a)) [8]. We then combined a porous superhydrophobic and hydrophobic slippery liquid-infused porous surface (SLIPs) under propagating waves (Fig. 1(b)) [9]. We demonstrated that through an active and passive polymer approach, we can reduce the droplet contact time by as much as 35%. We then showed that although we can use a simple process to create a porous superhydrophobic surface, the wave cannot penetrate into the droplet due to surface porosity. Using a simple lubricant-infused surface, we can also show an active reduction in contact time by up to 30% compared to without acoustic waves. Further, we showed that we could change both impact time and rebound angle in both surface impact scenarios on different surfaces.

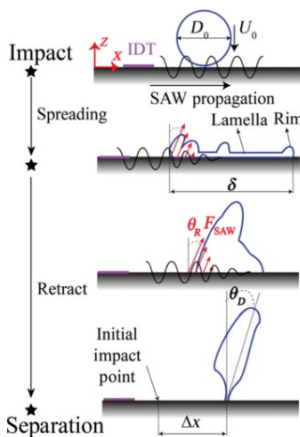


Figure 1a: Illustration of the evolution of a droplet impacting a solid surface with a propagating SAW.

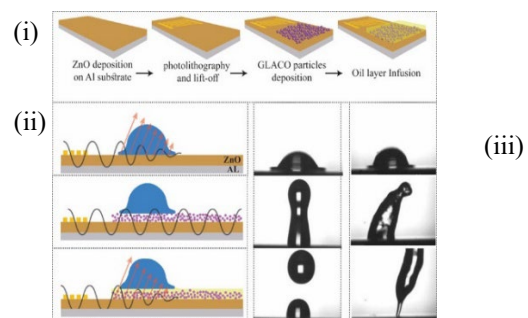


Figure 1b: (i) SAW device coated with SLIPs. (ii) SAW interacting with droplet on uncoated and SLIP surface. (iii) Droplet impacting on SLIPs surfaces, with and without propagating SAWs.

Effect of Substrate Inclination

Following the initial work on droplet impact on horizontal surfaces with surface coatings, we then investigated droplet impact on inclined hydrophobic coatings (as shown in Figure 2) [10]. We coated a SAW device with a hydrophobic polymer before inclining the surface for droplet impact. We used a numerical simulation method to explore the mechanisms of droplet impact. The numerical results revealed that applying SAW alters the energy budget inside the droplet, which leads to different droplet impact behaviour. We showed that using SAW, the impact regime on hydrophobic

inclined surfaces changes from deposition to complete rebound. We showed that the maximum contact time is reduced by 50%, and the droplet spreading and retraction dynamics are altered. We also demonstrated that by changing the direction of the acoustic wave, we could alter the rebound direction, as shown schematically in Fig. 2.

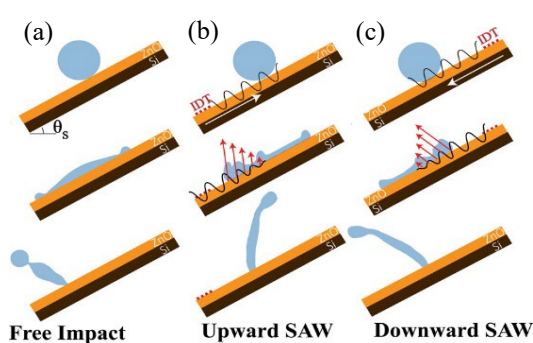


Figure 2: (a) Illustration of droplet impact without SAW. (b) Illustration of droplet impact with SAW travelling upwards. (c) Illustration of droplet impact with SAW travelling downwards.

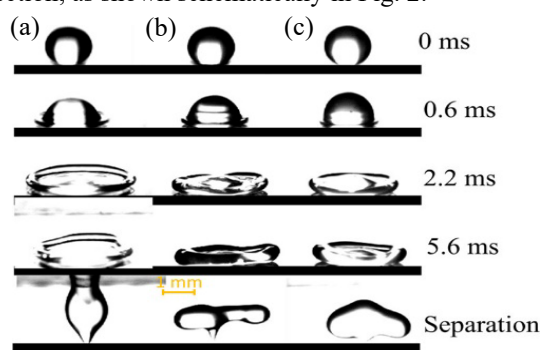


Figure 3. Snapshots of (a) X800, (b) X4000, and (c) X6000 solutions impacting on GLACO-coated surface. In all experiments, a droplet with a volume of $3.6 \mu\text{l}$ impacts the solid surface with a velocity of 1.4 m/s .

Non-Newtonian Droplet Impact With and Without SAW

We further studied one type of non-Newtonian droplet impact onto superhydrophobic surfaces to investigate the effect of changing liquid rheology [11]. We showed that through the introduction of xanthan polymer to create non-Newtonian liquids, we can alter an impacting droplet rebound shape (see Fig. 3). By increasing the concentration of xanthan polymer in the liquid droplet we can reduce the contact time of the impacting droplet by 50%. We compare these liquids with Newtonian glycerol droplets of similar viscosity. We find that the differences in the rebounding droplets shape (which look like a mushroom cap) are as a result of the viscoelastic behaviour of the non-Newtonian droplets (see Fig. 3). We also showed that by increasing the Weber number, we can decrease the contact time and increase the droplet's maximum spreading radius. We also examined the influences of non-Newtonian droplet impact on hydrophobic-coated SAW devices. Similar to Newtonian liquids, we showed that in the impact scenarios of non-Newtonian droplets, the applied acoustic energy to the liquid during the interaction with the solid surface could alter the impact regime from deposition and partial rebound to complete rebound. We also showed that by using SAWs, we not only changed the contact time of an impacting droplet but also altered the spreading and retraction dynamics and jetting angles.

Conclusion

This study investigated droplet impact on both flat and inclined hydrophobic SAW devices with propagating SAWs. We investigated the influences of SAWs on porous superhydrophobic surfaces and found that SAWs cannot transfer to the droplet due to porosity. We showed that we effectively altered droplet impact dynamics by using hydrophobic liquid-infused surfaces. In the case of all flat and inclined hydrophobic surfaces, we showed SAW has an active reduction in contact time and changed the droplet impact dynamics. We showed that we altered droplets' contact time onto the superhydrophobic surface and the droplets' shape by adding xanthan polymer to form non-Newtonian liquids. By changing the Weber number, we changed the droplet's contact time. Finally, in more recent work, we showed that SAW reduced the contact time of impacting non-Newtonian and Newtonian liquids.

References

1. Cionti, C., T. Taroni, and D. Meroni, *Bouncing Droplets: A Hands-On Activity To Demonstrate the Properties and Applications of Superhydrophobic Surface Coatings*. Journal of Chemical Education, 2019. **96**(9): p. 1971-1976.
2. Derby, B., *Inkjet Printing of Functional and Structural Materials: Fluid Property Requirements, Feature Stability, and Resolution*. Annual Review of Materials Research, 2010. **40**(1): p. 395-414.
3. Bird, J.C., et al., *Reducing the contact time of a bouncing drop*. Nature, 2013. **503**(7476): p. 385-8.
4. Zhang, S., et al., *Bioinspired Surfaces with Superwettability for Anti-Icing and Ice-Phobic Application: Concept, Mechanism, and Design*. Small, 2017. **13**(48).
5. Jezeršek, M., et al., *Control of Droplet Impact through Magnetic Actuation of Surface Microstructures*. Advanced Materials Interfaces, 2023. **10**(11).
6. Weisensee, P.B., et al., *Droplet impact on vibrating superhydrophobic surfaces*. Physical Review Fluids, 2017. **2**(10).
7. Niu, X., et al., *Pillar-induced droplet merging in microfluidic circuits*. Lab Chip, 2008. **8**(11): p. 1837-41.
8. Biroun, M.H., et al., *Acoustic Waves for Active Reduction of Contact Time in Droplet Impact*. Physical Review Applied, 2020. **14**(2).
9. Biroun, M.H., et al., *Surface Acoustic Waves to Control Droplet Impact onto Superhydrophobic and Slippery Liquid-Infused Porous Surfaces*. ACS Appl Mater Interfaces, 2021. **13**(38): p. 46076-46087.
10. M, H.B., et al., *Dynamic Behavior of Droplet Impact on Inclined Surfaces with Acoustic Waves*. Langmuir, 2020. **36**(34): p. 10175-10186.
11. Biroun, M.H., et al., *Impact Dynamics of Non-Newtonian Droplets on Superhydrophobic Surfaces*. Langmuir, 2023. **39**(16): p. 5793-5802.



Structural reorganization of actin filaments in a circular flow using surface acoustic waves

Minseo Kim, Donyoung Kang¹, and Hyungsuk Lee¹

¹School of Mechanical Engineering, Yonsei University, Seoul, Republic of Korea
E-mail: kdy5131@yonsei.ac.kr, URL: <https://leelab.yonsei.ac.kr>

Introduction

Actin, a major cytoskeletal protein, plays a pivotal role in providing structural support to cells and executing key functions, such as cell migration, and division. Actin filament is 7 nm in diameter and its persistence length is approximately 15 μm . Since the contour length of actin filament is similar to the persistence length, actin filament behaves as a semi-flexible polymer which is not rigid and not flexible. In cells, actin filaments are cross-linked and bundled via interacting with types of actin binding proteins. Recent studies demonstrated that mechanical environmental conditions such as substrate stiffness and cytoplasmic streaming play an important role in determining the organization of actin filaments [1,2]. However, it still remains unclear how the organization of actin filaments are regulated in the presence of streaming flow. We developed an experimental platform that was able to generate a circular flow in the sessile droplet mimicking the cytoplasmic flow observed in a cell using surface acoustic waves. We demonstrated how the circular flow affects the reorganization of actin filaments into a higher-order structure. The computational model consisting of actin filaments and streaming flow elucidated the mechanism of actin filament assembly subjected to the circular flow. Our study suggests that the intracellular flow plays an important role in determining the organization of the cytoskeletal protein into a specific structure to perform the cellular function.

Circular flow within a living organism can cause changes in protein structure

Various types of circular flow are present in cells and tissues. As the cell is a poroelastic material, intracellular flows are present in varied forms and they produce a localized shear stress to the cytoskeleton filament networks [3]. Actin filaments subjected to shear stress can undergo buckling, tumbling, and alignment depending on the magnitude and direction of the stress [4]. Shear stress produced by extracellular flow can lead to reorganization of actin networks and formation of stress fibers within the cell [2]. In particular, intracellular flows exhibit circular patterns due to the geometric boundary defined by the cell membrane. The interaction between the endoplasmic reticulum (ER), microtubules, and kinesin-1 generates circular flow, leading to the local alignment of microtubules according to the flow direction [5]. The circular flow formed by the actin flow near the cell boundary contribute displacing the meiotic spindles towards the cortical cap [6]. These findings indicate that circular intracellular flow affect the actin filament structures formed with actin binding proteins (ABPs) and motor proteins. The previous study demonstrated that the bundling of actin filament by ABP filamin was significantly promoted in the presence of flow [2]. However, it remains elusive how the circular flow observed in cells dictates the structure reorganization of actin filaments assembly.

Circular flow is generated using Leaky SAW in a sessile droplet

In this study, in order to produce circular flows in an *in vitro* cell-mimicking droplet, we applied traveling surface acoustic waves to a half of the ground area where the droplet comes into contact with the LiNbO_3 substrate. (Figure 1a). Using COMSOL Multiphysics, we developed a model of the sessile droplet with the circular flow, similar to the experiment (Figure 1b). A traveling wave formed from one port of IDT became a leaky SAW when it encountered the bottom side of the droplet. Both acoustic pressure and streaming field in a droplet subjected to the leaky SAW were obtained using the developed model. We also analyzed streamlines of particles of nm- μm scales to predict trajectories of actin filaments. Particle Image Velocimetry (PIV) method was used to obtain the velocity map of the circular flow in a sessile drop (Figure 1c).

Assembly of actin filaments subjected to the circular flow

Using a device that produces a circular flow in a 3D sessile droplet by SAW, we investigated the effect of the circular flow on actin filaments assembly. Fluorescence image analysis revealed that actin filaments were assembled into a bundled structure more in the presence of the circular flow at the critical speed (Figure 1d). These results indicate that the circular flow and consequential shear stress play a role in altering the organization manner of actin filaments assembly. Experiments with various types of ABP and divalent cations

suggest that actin filaments reorganization is regulated by not only chemical and mechanical environment in a complex manner.

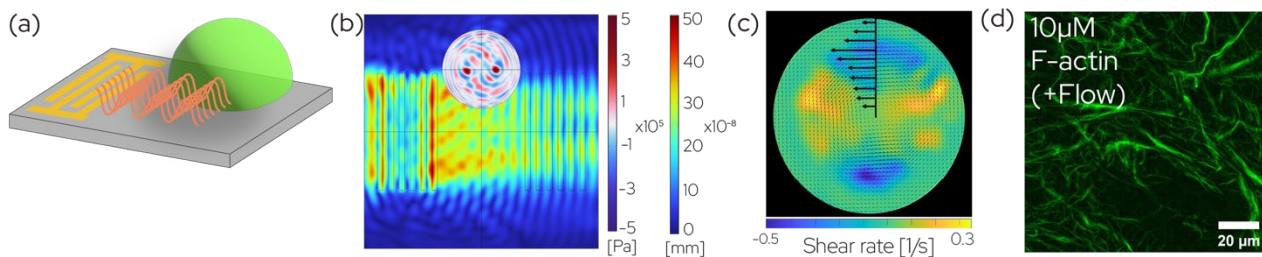


Figure 1: Experimental and computational setup for generating circular flow in an aqueous sessile droplet. (a) Schematic illustration of SAW generator and the droplet. (b) Computational model of the circular flow in a sessile droplet. (c) Particle image velocimetry-derived shear rate distribution in a sessile droplet. (d) Structural reorganization of actin filaments in circular flow.

Conclusion

We designed an acoustofluidic device that is able to produce a circular flow in a cell-like sessile droplet to investigate the effect of intercellular flow on organization of actin filaments assembly. We demonstrated that the structures of actin filament assembly were reorganized into various forms in the presence of the circular flow. We analyzed the change in size and mechanical properties of reorganized actin filaments by circular flow at varying speeds. Our results suggest that intercellular flow plays an important role in regulating actin filaments reorganization for conducting a specific function in a spatiotemporal manner. Our methods and techniques can be used not only to elucidate the mechanisms of structure reorganization but also to fabricate a higher-order structures of biopolymers such as actin, microtubules, extracellular fiber collagen, and DNA. We are looking forward to presenting our study for the international acoustofluidics community at the *Acoustofluidics 2023 in person Conference* on 16 - 18 August 2023.

References

- [1] D.H. Wachsstock, W.H. Schwartz, and T.D. Pollard. *Biophysical Journal* **65**(1): p. 205-214 (1993).
- [2] B. Kang, S. Jo, J. Baek, F. Nakamura, W. Hwang and H. Lee. *Acta Biomaterialia* **90**: p. 217-224 (2019).
- [3] E. Moeendarbary, L. Valon, M. Fritzsche, A. R. Harris, D. A. Moulding, A. J. Thrasher, E. Stride., and L. Mahadevan. *Nature Materials* **12**(3): p. 253-261 (2013).
- [4] M.P Murrell., and M.L. Gardel. *Proceedings of the National Academy of Sciences*. **109**(51): p. 20820-20825 (2012)
- [5] K. Kimura, A. Mamane, T. Sasaki, K. Sato, J. Takagi, R. Niwayama, L. Hufnagel, Y. Shimamoto, J. F. Joanny, S. Uchida., and A. Kimura. *Nature Cell Biology* **19**(4): p. 399-406 (2017).
- [6] K. Yi, J. R. Unruh, M. Deng, B. D. Slaughter, B. Rubinstein, and R. Li. *Nature Cell Biology* **13**(10): p. 1252-1258 (2011).

Piezoelectric phononic crystal-based acoustic tweezers

Feiyan Cai¹, Jun Wang^{1,2}, Yongchuan Li¹, Ke Deng², Hairong Zheng¹

¹Paul C. Lauterbur Research Center for Biomedical Imaging, Shenzhen Institutes of Advanced Technology, Chinese Academy of Sciences, Shenzhen 518055, China

E-mail: fy.cai@siat.ac.cn

²Department of Physics, Jishou University, Jishou 416000, China

Introduction

Acoustic tweezers are a promising technology for cell separation, tissue engineering, and drug delivery due to their non-contact nature, low power consumption, weak biological damage, and deep penetration depth [1,2]. This technology relies on the exchange of momentum between the acoustic field and particle to induce an acoustic radiation force that controls particle movement [3]. To achieve high-performance acoustic tweezers, it is crucial to shape the acoustic fields. Traditionally, there are two main categories of the field for acoustic tweezers, bulk acoustic wave (BAW) and surface acoustic wave (SAW). The SAW-based acoustic tweezers operate at high frequencies (>20MHz) with high precision, while the BAW-based acoustic tweezers operate at lower frequencies and require the use of artificial structure (such as lenses, holograms, metasurface, etc.) on the transducer surface to shape the field [4,5]. However, these additional artificial structures make the device complex and unstable. Piezoelectric phononic crystals offer tunability of frequency band structure through electric command use [6]. In this study, we design low-frequency piezoelectric phononic crystal-based acoustic tweezers (PPCAT) to achieve periodic alignment of particles at different heights.

Numerical simulation

This PPCAT consists of a piezoceramic plate with a one-dimensional periodic array of electrodes set on one side and an entire electrode layer on the other. By precisely designing the period of electrodes and the thickness of the plate, two specific modes can be excited, one is the zero-asymmetric (A0) Lamé wave intrinsically in the plate, and the other is the wood's anomaly due to the periodic electrode resonance [4]. The resonances of the piezoceramic phononic crystals tune the sound fields, and radiation forces can realize desired manipulations.

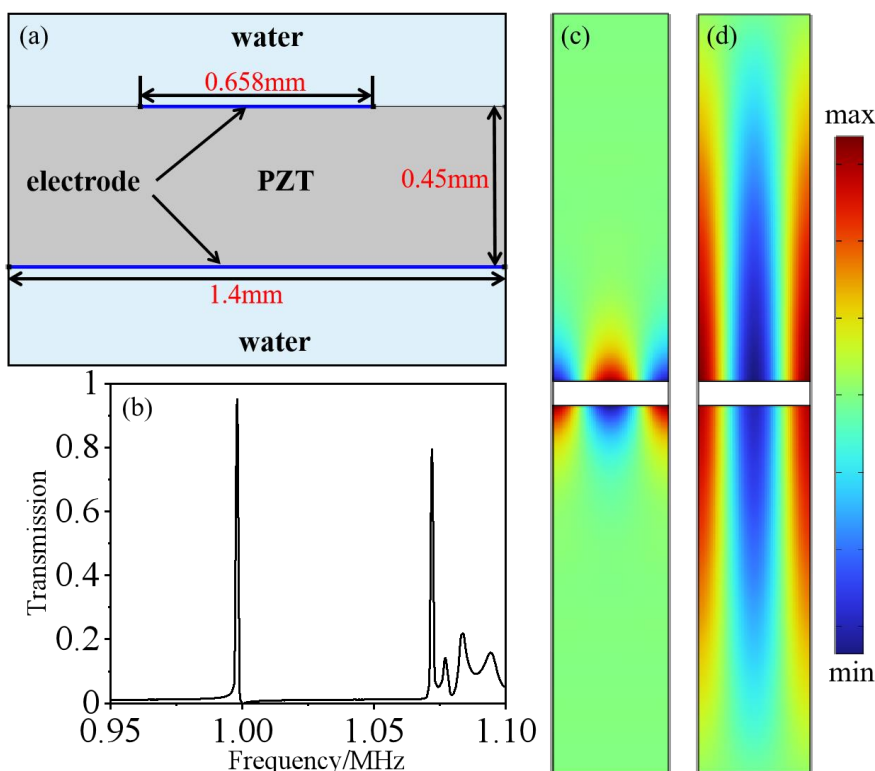


Figure 1: (a) Schematic of a unit cell of the piezoelectric phononic crystal plate. (b) The acoustic resonant spectrum of the piezoelectric phononic crystal plate, with two significant peaks corresponding to frequencies of 0.998 MHz and 1.072 MHz. Pressure field distribution around a unit cell of the piezoelectric phononic crystal at the frequency of 0.998 MHz (c) and at the frequency of 1.072 MHz (d).

We use finite element COMSOL Multiphysics® software for numerical simulations. As shown in Fig. 1(a), the left and right sides used periodic boundary conditions, while the top and bottom sides used radiation boundary conditions. Fig. 1(b) shows the acoustic resonant spectrum of the PPCAT system. There are two significant resonant peaks with frequencies of 0.998 MHz and 1.072 MHz, respectively. The resonant pressure field of 0.998MHz is shown in Fig. 1(c). It is clearly observed that the pressure fields are a standing field parallel to the plate surface and a gradient field vertical to the plate surface, i.e., the excited A_0 Lamb wave. Fig. 1(d) shows the resonant pressure fields of 1.072MHz, while the pressure field is also a standing field parallel to the plate surface but a weak gradient field vertical to the plate surface. This field is the excitation of the wood's anomaly.

Experimental process

We fabricate a piezoelectric phononic crystal plate, as shown in Fig. 2(a). Then we conduct an experiment to manipulate polystyrene (PS) particles with a radius of $80\mu\text{m}$. Initially, these water-immersed PS particles are random on the surface of the plate, as shown in Fig. 2(b). When the PPCAT is loaded with an electrical signal with a resonant frequency of 0.998 MHz, these PS particles can be periodically trapped on the surface of the PPCAT, as shown in Fig. 2(c). When the PPCAT is loaded with an electrical signal with a resonant frequency of 1.072 MHz, these PS particles can be periodically suspended in water, as shown in Fig. 2(d-e).

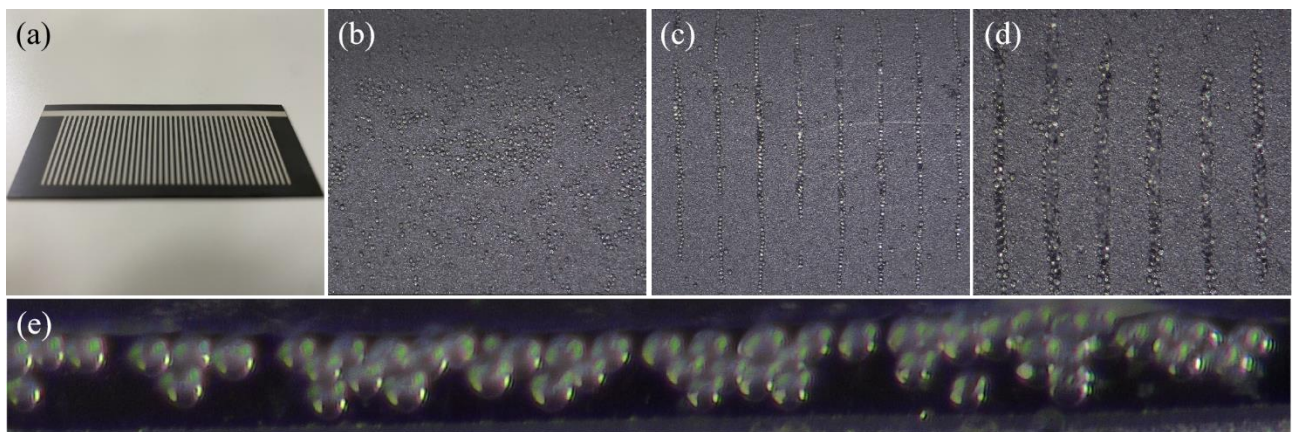


Figure 2: (a) A top view of the piezoelectric phononic crystal plate sample. (b) The state of the PS particles when the PPCAT is not loaded with an electrical signal. (c) The state of the PS particles when the PPCAT is loaded with an electrical signal at a frequency of 0.998MHz. (d) The same as (c) but at a frequency of 1.072MHz. (e) A side view of (d).

Conclusion

We numerically and experimentally demonstrate the manipulation of particles based on piezoelectric phonon crystal plates. The concepts and realization of manipulation of particles by PPCAT advance the development of compact acoustic tweezers with high precision and low energy consumption.

References

- [1] Fushimi T, Marzo A, Drinkwater BW, Hill TL. Acoustophoretic volumetric displays using a fast-moving levitated particle. *Applied Physics Letters*. 2019; 115(6).
- [2] Joseph Rufo, Feiyan Cai, James Friend, Martin Wiklund & Tony Jun Huang. Acoustofluidics for biomedical applications. *Nature Reviews Methods Primers* 2022; 2(30).
- [3] Hasegawa T, Hino Y, Annou A, Noda H, Kato M, Inoue N. Acoustic radiation pressure acting on spherical and cylindrical shells. *The Journal of the Acoustical Society of America*. 1993; 93(1):154-61.
- [4] Fei Li, Feiyan Cai, Likun Zhang, Zhengyou Liu, Feng Li, Long Meng, Junru Wu, Jiangyu Li, Xiaofeng Zhang & Hairong Zheng. Phononic-Crystal-Enabled Dynamic Manipulation of Microparticles and Cells in an Acoustofluidic Channel. *Physical Review Applied* 2020; 13, 044077.
- [5] Fei Li, Fei Yan, Zhiyi Chen, Junjun Lei, Jinsui Yu, Mian Chen, Wei Zhou, Long Meng, Lili Niu, Junru Wu, Jiangyu Li, Feiyan Cai & Hairong Zheng. Phononic crystal-enhanced near-boundary streaming for sonoporation. *Applied Physics Letters* 2018; 113, 083701.
- [6] Kherraz N, Chikh-Bled FH, Sainidou R, Morvan B, Rembert P. Tunable phononic structures using Lamb waves in a piezoceramic plate. *Physical Review B*. 2019; 99(9).

Acoustofluidic trapping and analysis of microswimmers

Advaith Narayan¹, Mingyang Cui^{1,2}, and J. Mark Meacham¹

¹Department of Mechanical Engineering and Materials Science, Washington University in St. Louis, St. Louis, MO 63130, USA

E-mail: narayan@wustl.edu, meachamjm@wustl.edu; Web: <https://meachamlab.wustl.edu>

²Research Laboratory of Electronics, Massachusetts Institute of Technology, Cambridge, MA 02139, USA

Introduction

Motile cells like *Chlamydomonas reinhardtii* and *Tetrahymena thermophila* are popular model organisms for research in the biomedical sciences, genetics, and cell biology, as well as for fundamental studies of cilia and microswimmer dynamics [1,2]. Acoustofluidics offers unique opportunities to trap and analyze these cells without inhibiting or influencing their innate swimming behavior due to its label-free trapping capability [2]. The work reported here summarizes our use of various acoustic microfluidic technologies to trap and analyze microswimmers to better understand (i) the motility of the whole organism and (ii) the movement of propulsive cilia. Within these two categories, we have (1) applied bulk acoustic wave (BAW) devices for large-population trap-and-release of *C. reinhardtii* to rapidly measure and differentiate cell types based on motility, (2) used BAW driven by surface acoustic wave (SAW) actuators to study motion coupling of two confined *C. reinhardtii* cells, and (3) performed high-resolution (in space and time) studies of cilia waveform in single-cell organisms (*C. reinhardtii* and *Tetrahymena*) using hybrid BAW/SAW devices.

Population-based acoustic trap-and-release of *C. reinhardtii* cells

Ciliated cells exist throughout the human body to actively move fluids and/or foreign matter by beating hair-like cilia. Ciliary dysfunction can disrupt critical flows of fluids; defects in structure and function are implicated in several disorders. In swimming unicellular organisms, abnormalities in the cilia affect propulsive capability. Investigation of motility impairment often involves tedious measurement of individual cell trajectories to characterize a population. Alternatively, less-sensitive population-based studies are applied. Our recently described acoustic trap-and-release of large cell populations provides the efficiency of population-based approaches while maintaining the sensitivity of the individual-cell studies (Fig. 1a) [1].

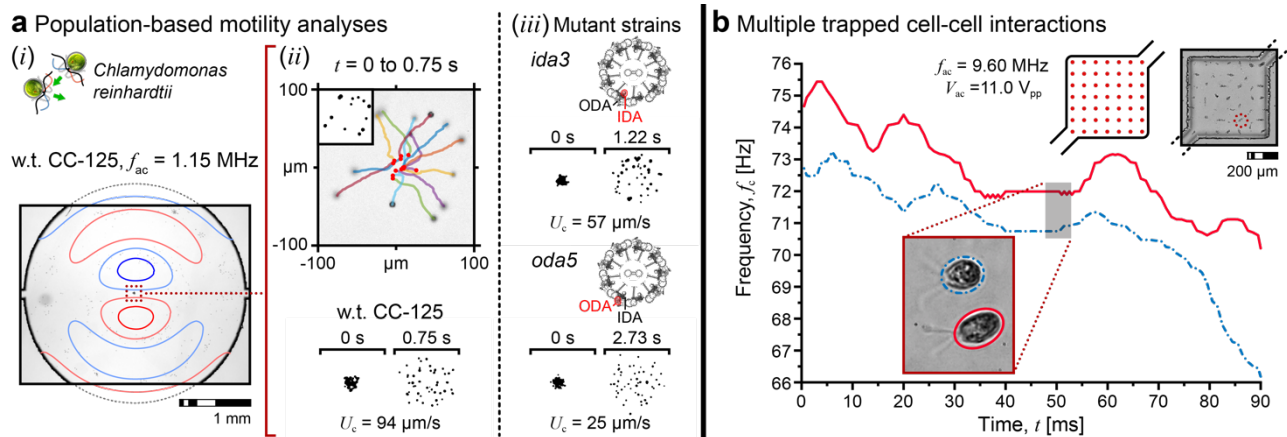


Figure 1: Acoustofluidic studies involving more than one cell. (a) BAW-based acoustic trap-and-release to measure and differentiate wildtype *C. reinhardtii* cells from motility-impaired mutants (strains *ida3* and *oda5*) (adapted from [1]). (b) Hybrid BAW/SAW trapping and analysis of cell-cell interactions for two acoustically confined *C. reinhardtii* cells.

Silicon BAW devices were fabricated using standard photolithography, deep reactive ion etching (DRIE), and anodic bonding to glass. A bulk piezoelectric (PZT-8) transducer was used to generate a two-dimensional (2D) circular trap that concentrated cells in a tight agglomerate prior to release (Fig. 1a). Average motility was assessed by measuring swimming speeds based on the variation in polar area moment of inertia for spreading cell populations. Our method semiautomatically determined the cell motility for hundreds of cells in a matter of minutes, finding that $U_{c,w.t.} = 94 \mu\text{m/s}$ exceeded $U_{c,ida3} = 57 \mu\text{m/s}$ and $U_{c,oda5} = 25 \mu\text{m/s}$. Results matched measurements using mean squared displacement of individual cell trajectories, which took hours to obtain [1].

Two-cell motion coupling of acoustically confined *C. reinhardtii* cells

We have applied a hybrid BAW/SAW technology to analyze the motion of two *C. Reinhardtii* cells confined within a single acoustic potential well to characterize intercellular coupling of their swimming behavior (Fig. 1b). In BAW/SAW devices, a single pair of IDTs generated a standing SAW to actuate a 2D BAW field in a square glass chamber oriented at 45° to the SAW propagation direction (Fig. 1b). Glass chambers bonded to 128° Y-cut, X-propagating lithium niobate (LiNbO₃) substrates were fabricated as described previously [3]. When dilute suspensions of *C. Reinhardtii* were loaded into the chamber, one to three cells were held at each acoustic pressure node of an $\sim 7 \times 7$ grid. Two-cell traps were selected, and the x, y displacements and θ rotation of each cell were tracked with respect to their anterior-posterior (A-P) axis. A Hilbert transform was used to reveal the instantaneous frequency of each cell and phase difference. We observed phase locking and frequency coupling, with one cell typically leading a follower cell. Ongoing experiments will determine whether this phenomenon is due to viscous coupling *via* the fluid, body force interactions, or feedback due to cilia-body or cilia-cilia contact.

Single-cell investigations of cilia motion in *C. reinhardtii* and *Tetrahymena*

The cilia that drive movement of physiological fluids are abundant, but the mechanisms governing their motion are still poorly understood. Model organisms like the biciliate *C. reinhardtii* and the multiciliate *Tetrahymena* are used to elucidate the relationships between structure and function of human cilia. We recently applied our hybrid BAW/SAW acoustic tweezers to conduct a detailed investigation of cilia synchronization, three-dimensional (3D) swimming, and the ciliary response to changing environmental conditions (e.g., temperature, viscosity) for wildtype *C. reinhardtii* cells (Fig. 2a) [2]. Acoustic actuation was found to have no adverse effect on cell swimming with various waveform parameters (beat frequency f_c , amplitude θ_c^{SD} , and average curvature $\bar{\kappa}_{c,wt}$) matching those determined using free-swimming or pipette-held cells. θ_c^{SD} and $\bar{\kappa}_{c,wt}$ were stable with increasing temperature from 15 to 25 °C, while f_c and the helical rotation rate increased by $\sim 20\%$ for each 5 °C increase in temperature over this range (e.g., helical rotation frequency increased from 2.1 to 2.6 to 3.2 Hz). In addition, increases in viscosity were found to promote asynchronous beating for media with viscosities $\eta = 1$ cP, 3 cP, 5 cP, and 8 cP. No synchronous beating of the two cilia was observed beyond $\eta = 3$ cP (Fig. 2a.iii). Ongoing experiments will extend our method to investigate ciliary motion and coordination in *Tetrahymena thermophila*, a single-cell organism with 100s of cilia (Fig. 2b). Critical to our approach is that acoustic confinement imparts negligible torque on swimming cells (vs. use of micropipette e.g.), allowing cells to move with six degrees of freedom while trapped. Further, the hybrid BAW/SAW technology combines the efficiency of BAW with the resolution of SAW, enabling prolonged observation of cells using oil-immersion microscopy.

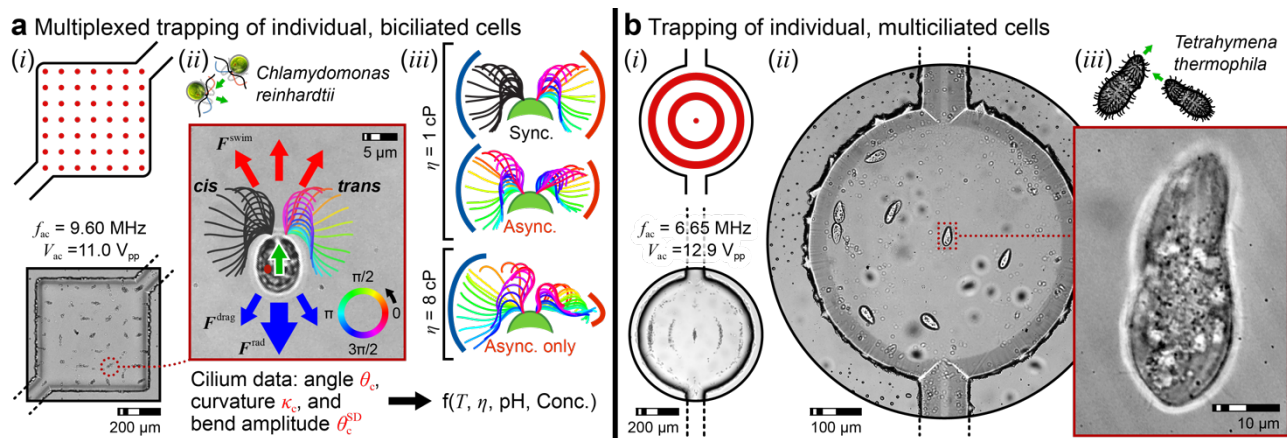


Figure 2: Acoustofluidic studies involving single cells. **(a)** Hybrid BAW/SAW acoustic tweezers enable investigation of cilia waveform for wildtype *C. reinhardtii* cells (adapted from [2]). **(b)** Observation of acoustically confined *Tetrahymena*.

Conclusion

Acoustofluidics enables study of microswimmer locomotion and dynamics at various scales from population-based motility assessment to cilia motion at the single-cell level. Prolonged exposure to ultrasound does not appear to affect swimming mechanics and enables analysis of locally free-swimming cells. Hybrid BAW/SAW devices are particularly well-suited to single- and two-cell studies due to a high efficiency and compatibility with high-speed oil immersion microscopy. Thus, our approach can be adopted in a wide range of applications in biology, biomedical engineering, and biophysics.

Acknowledgements

This work was supported by National Science Foundation Grant Nos. CMMI-1633971 and CBET-1944063.

References

- [1] M. Kim, E. Huff, M. Bottier, S. K. Dutcher, P. V. Bayly and J. M. Meacham, *Soft Matter*, 2019, **15**, 4266-4275.
- [2] M. Cui, S. K. Dutcher, P. V. Bayly and J. M. Meacham, *Proc. Natl. Acad. Sci. U.S.A.*, 2023, **120**, e2218951120.
- [3] M. Cui, M. Kim, P. B. Weisensee and J. M. Meacham, *Lab Chip*, 2021, **21**, 2534-2543.



Self-assembly and self-organization in acoustic Levitation

Mauricio Hoyos¹, Jean-Michel Peyrin² Nathan Jeger-Madiot¹ and Jean-Luc Aider¹

¹Laboratoire de physique et Mécanique des Milieux Hétérogènes, École Supérieure de Physique et Chimie Industrielles de la ville de Paris (ESPCI Paris – PSL), Centre National de la Recherche Scientifique (CNRS), 1 rue Jussieu 75005 Paris, France.

²Institut de Biologie Paris Seine, IBPS, Paris, France
E-mail: hoyos@pmmh.espci.fr,

Introduction

In acoustic levitation, particles, biological objects like blood cells, neurons or micro-algae, and more exotic objects like nanorods and nano-helices, exhibit interesting collective behaviors, that can be characterized and studied. In this presentation we'll show examples of various self-assembled and self-organized structures that can be witnessed in acoustic levitation. We will propose a way of quantifying those phenomena taking advantage of the many possibilities provided by the acoustic confinement of those micro-objects. By the comprehension of the dynamics of both processes we shall show how acoustic levitation can become a method of choice for controlling a possible transition from self-assembly to self-organized structures.

Self-assembly: The standard definition of self-assembly states that “*it is a process in which a disordered system of pre-existing components forms an organized structure or pattern as a consequence of specific, local interactions among the components themselves, without external direction*” [1]. Nevertheless, for our interest into the dynamics of self-assembly in acoustic levitation, it is necessary to delve deeper into the phenomenon. Actually, we are concerned with the triggering and with the final product of the process. If it is true that the “self-process” implies somehow, that it doesn't need any direction, it requires energy at the beginning, either generated by the system, or injected from outside of the system. At the end of the process, an equilibrium is established leading to a new state, that because it results from an out-of-equilibrium state.

We will consider various examples to try to understand how the whole process is controlled. For instance, is not our case, Fig 1 shows a **static self-assembly** of a sodium chloride crystal structure. The structure is fixed by the atomic nature of the components; the final structure (shape and size), depends on the elementary nature of the chemical species and the supersaturation of the solution-forming the crystal.

In Fig. 2, we show a dynamical self-assembly of polymeric TPM demulsion droplets using acoustic levitation. A suspension of disorganized emulsion droplets, is confined in a micro chamber. An acoustic energy undergoing by all the species in suspension push them to gather around a specific region pressure node, forming structured aggregates.

Self-organization: *Self-organizing systems are systems which can acquire macroscopic spatial, temporal; or spatio-temporal structures by means of internal processes, without specific interference from the outside.*

Fig. 3 shows the time-averaged velocity field of swarming e-coli bacteria confined in acoustic levitation. One can see clearly the formation of large-scale vortical structures that can be considered as a self-organization of the collective motion of the micro-organisms.

Figure 4 shows the self-organization of mesenchymal stem cells forming spheroids after 24 hours of being suspended in acoustic levitation.

By using much more examples we shall study the influence of acoustic radiation force in the dynamics of self-assembly and self-organization biological cells.

Conclusion: Using various examples we have shown that acoustic levitation can be used as an interesting tool to study various self-organization processes. Depending on the manipulated objects, either passive or active, living or not, it can lead to various large-scale organized micro-structures from layers of particles assembled in crystal-like structure to cells spheroids and organoids. We believe that the identification and the classification of the mechanisms that underpin self-organization and self-assembly can be very important and useful to synthesize several forms of biological constructs (tumors, organoids, spheroids) and even novel unknown structures. Leading to a better use of acoustic levitation in tissue engineering and more biological applications.

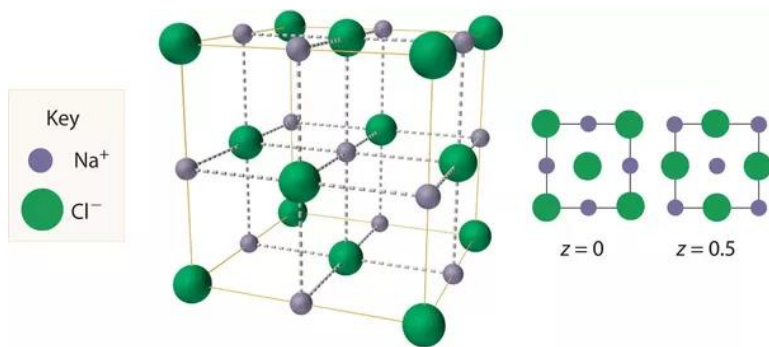


Figure 1: static-self assembly of NaCl Crystal fixed self-assembly structure of atoms using classical crystal growth techniques

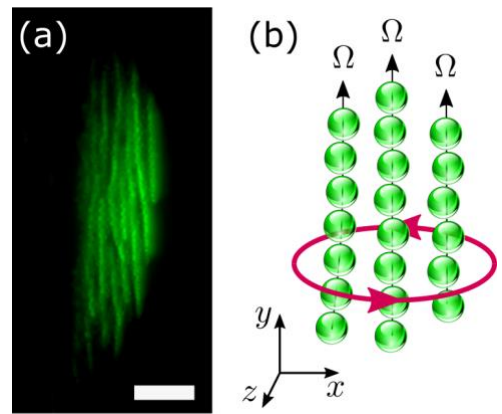


Figure 2: dynamical self-assembly of emulsion of polymeric TPM microscopic droplets in acoustic levitation obtained from a disorganized suspension. Droplet chains are assembled

Figure 3: Self-organization of bacteria in acoustic levitation. Structures self-organized leading probably to emergence of bio-turbulence

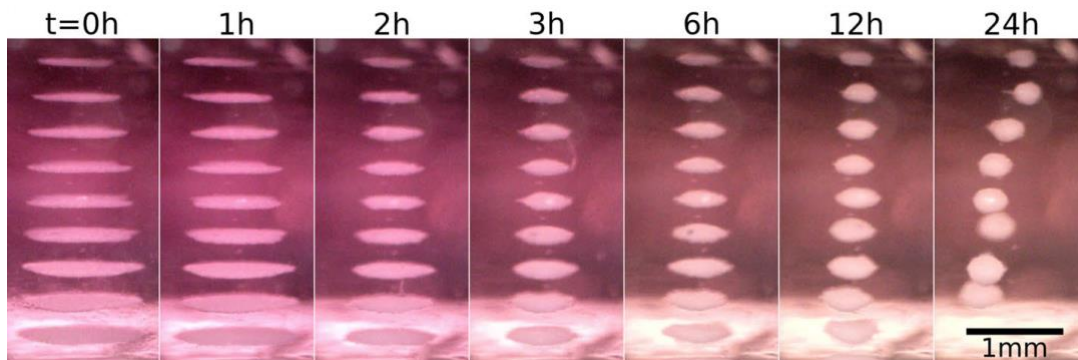
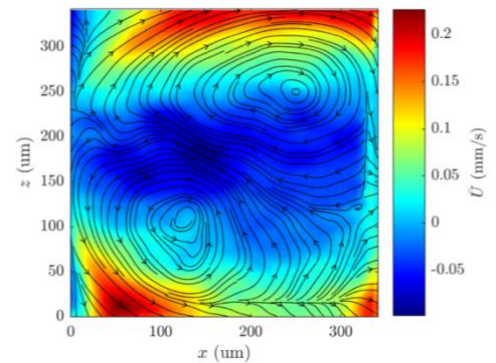


Figure 4: self-organization of mesenchymal stem cells in spheroids in acoustic levitation in a resonator provide with several nodes. Each node is occupied by one spheroid. Self-organization is reached in 24 hours.

References:

- 1- Self-organization and culture of Mesenchymal Stem Cell spheroids in acoustic levitation, Nathan Jeger-Madiot et al, scientific reports, (2011) 8355.
- 2- Ultrasonic chaining of emulsion droplets, M. Abdelaziz et al, Physical review Research, 3,043157(2021)
- 3- Induced clustering of Escherichia coli by acoustic fields, Gutierrez-ramos et al. scientific Reports, 8, 4668(2018)



Mapping the acoustic properties of two-phase systems for use in droplet acoustofluidics

Qian Shi, Zhenhua Liu, Anna Fornell, Gabriel Werr, Laurent Barbe and Maria Tenje

Dept. Materials Science and Engineering, Science for Life Laboratory, Uppsala University, Uppsala, Sweden
E-mail: maria.tenje@angstrom.uu.se

Introduction

The ability to manipulate particles or cells inside water-in-oil droplets is essential to various chemical, biological and biomedical assays performed using droplet microfluidics systems. Bulk acoustophoresis permits spatial localization of cells and particles in a label-free and non-contact manner by utilizing acoustic standing wave and is therefore a suitable particle manipulation method for integration with droplet microfluidics. Fluorinated oils, *e.g.*, Novec HFE-7500, are most commonly used as the continuous phase in typical droplet applications as they are permeable to gases and insoluble for most organic compounds [1]. Previous studies, however, have concluded that sufficient acoustic focusing capability cannot be achieved inside aqueous droplets generated in HFE-7500 due to a mismatch in the acoustic properties of the two phases used [2,3]. The critical acoustic properties that underlie this difference in acoustic focusing capability were however not identified. This work presents a study where the suitability of a selection of oils, from three categories commonly used in droplet microfluidics (hydrocarbon oil, fluorinated oil and silicone oil), was examined for acoustic particle manipulation in water-in-oil droplets. We hypothesized that when performing acoustic focusing inside aqueous droplets confined in a microfluidic channel (*i.e.*, plugs), due to the presence of a thin oil film [4] between the channel wall and the droplet, the acoustic impedance between the two fluid phases must match in order to increase acoustic coupling efficiency between the two liquid phases. Through this experimental work, we demonstrate that hydrocarbon oils are most compatible with acoustic focusing in a two-phase system that generates channel-confined water-in-oil droplets due to matching acoustic properties with water. We also conclude that acoustic impedance matching between the two fluid phases is not critical for optimal droplet-internal particle manipulation. Our results suggest that a match in the speed of sound of the two phases may be more relevant in practice.

Materials and methods

We measured the speed of sound and density of eight different non-polar fluids, including hydrocarbon oils (light mineral oil, heavy mineral oil, linseed oil, sunflower oil and olive oil), fluorinated oils (HFE-7500 and FC-40) and a silicone oil (PDMS oil). The speed of sound of all fluids was measured by recording the time of flight of the travelling soundwave through a defined distance at a temperature of 25 °C. The density of the fluids at the same temperature was measured with a pycnometer. The results were used to calculate the characteristic acoustic impedance, Z , based on,

$$Z = \rho c \quad (1)$$

where ρ is the density of the medium, and c is the speed of sound in that medium.

For acoustic focusing, the dispersed phase was deionized (DI) water with 10 μm polystyrene (PS) beads. Surfactants were added to the continuous phases to stabilize the droplets. 5% (% v/v) polyglycerol polyricinoleate (PGPR) was added to all hydrocarbon oils, 2% (% v/v) Krytox FSH-157 was added to fluorinated oils and 5% (% v/v) ABIL EM-90 was added to silicone oil. Acoustic focusing was performed inside a glass-silicon chip with a cross-flow design operating in the squeezing regime actuated at half-wavelength resonance. The dimension of the channel was 375 μm in width and 175 μm in depth. The percentage of focused particles was defined as the number of beads in a region of interest (ROI) in an area $\pm 10\%$ from the center line.

Results

The density of DI water was measured to be 997 kg/m^3 at 25 °C. The density of six hydrocarbon oils was between 845-925 kg/m^3 , while it was in the range of 1,618-1,866 kg/m^3 for two fluorinated oils and 960 kg/m^3 for silicone oil. The speed of sound of DI water was measured to be 1,496 m/s at 25 °C. The speed of sound in the hydrocarbon oils was in the range of 1,428-1,488 m/s, 687-710 m/s for the fluorinated oils and 1,046 m/s for the silicone oil. The characteristic acoustic impedance of DI water is 1.49 MRayl. The characteristic acoustic impedance was in the range of 1.16-1.31 MRayl for the hydrocarbon oils, 1.15-1.28 MRayl for the fluorinated oils and 1.00 MRayl for the silicone oil.

The percentage of particles focused in the droplets in all hydrocarbon oils approximates 100% already at a measured peak-to-peak voltage of 20 V_{pp} under different flow rate ratios (data not shown). Intra-droplet particle focusing performance in silicone oil was compared to that in HFE-7500 at voltages of 20, 25 and 30 V_{pp} under the same total flow rate of 7 μl/min. We ensured identical residence time inside the channel by using a constant total flow rate, however, the flow rate ratios were adjusted to be 4:3 (oil:water) for experiments with silicone oil and 5:2 (oil:water) with HFE-7500 in order to achieve as similar droplet sizes as possible. The mean percentages of particles focused in droplets generated in silicone oil were 62.1±7.4%, 42.8±13.5% and 83.2±5.1% at 20, 25 and 30 V_{pp}, respectively, Fig. 1. The values were 40.6±13.2%, 56.3±9.2% and 62.0±7.0% in droplets generated in HFE-7500. The focusing of 10 μm PS beads in droplets generated in silicone oil was consistently better compared to that in HFE-7500, at all voltages.

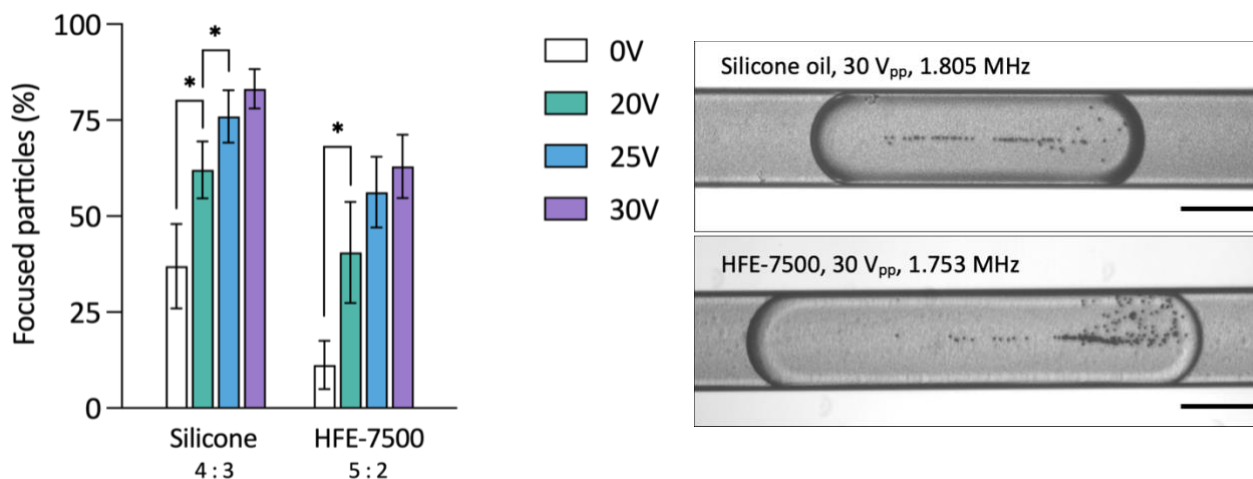


Figure 1: (Left) Acoustic intra-droplet 10 μm PS particle focusing quality in water droplets generated in silicone oil and HFE-7500 at 20, 25 and 30 V_{pp}, at resonance frequencies of 1.805 MHz and 1.753 MHz, respectively. The flow rates were set to 4 to 3 μL/min for silicon oil and DI water, respectively, and 5 to 2 μL/min for HFE-7500 and DI water, respectively. * indicates statistical difference between sample types ($p < 0.05$, Post-hoc Bonferroni test). $n = 20$. (Right) Brightfield images of acoustic focusing of 10 μm PS beads in water droplets generated in (top) silicone oil and (bottom) HFE-7500. The voltage was 30 V_{pp} in both cases. Direction of flow is to the left of the photograph. Scale bar = 300 μm.

Conclusion

We demonstrate through acoustic droplet-internal particle focusing that hydrocarbon oils have better acoustic performance. We demonstrate that the silicone oil we chose has better acoustic performance as compared to HFE-7500, a fluorinated oil, despite higher mismatch in acoustic impedance between the silicone oil (1.00 MRayl) and DI water (1.49 MRayl) as compared to that between HFE-7500 (1.15 MRayl) and DI water. This shows that acoustic impedance matching between the two fluid phases does not constitute the most important factor that affects intra-droplet particle focusing quality in droplet acoustofluidic systems. If we inspect other acoustically-relevant properties of the different oils, such as density and speed of sound, we find that although the density of silicone oil (960 kg/m³) matches the most to that of DI water (997 kg/m³), hydrocarbon oils (845-925 kg/m³) still had better acoustic performance. On the other hand, hydrocarbon oils (1,428-1,488 m/s) are most similar to water (1,496 m/s) in terms of speed of sound, followed by silicone oil (1,046 m/s) and then fluorinated oils (687-710 m/s), which corresponds to the order in their acoustic performance. This suggests that speed of sound is the most important parameter to match between the two fluid phases to achieve good focusing ability in future applications.

References

- [1] J-C. Baret. *Lab Chip* **12**, 422-433 (2012).
- [2] A. Fornell, F. Garofalo, J. Nilsson, H. Bruus and M. Tenje. *Microfluidics and Nanofluidics* **22**, 75 (2018).
- [3] M.S. Gerlt, D. Haidas, A. Ratschat, P. Suter, P.S. Dittrich and J. Dual. *Biomicrofluidics* **14**, 6 (2020).
- [4] C.N. Baroud, F. Gallaire and R. Dangla. *Lab Chip* **10**, 2032-2045 (2010).

Acoustofluidic droplet separation using traveling surface acoustic wave-induced acoustic radiation force

Mushtaq Ali¹, and Jinsoo Park¹

¹Department of Mechanical Engineering, Chonnam National University, Gwangju 61186, Republic of Korea
E-mail: alimushtaq012@jnu.ac.kr

Introduction

The separation of droplets with different characteristics is a crucial process in various applications such as cell sorting, single-cell analysis, and high throughput screening within droplet-based microfluidic platforms. While there have been several methods proposed for sorting droplets of the same kind, the development of techniques to separate multiple kinds of droplets, especially when they have the same volume, has received less attention. Most existing methods for droplet sorting or separation require labeling with fluorescent, magnetic, or electrical markers, and typically involve detecting the droplets upstream and applying external forces as needed. The demand for a label-free, detection-free, and continuous microfluidic separation method that relies on the inherent properties of droplets remains unmet. In this study, we present an acoustofluidic approach that utilizes ultrasonic surface acoustic waves (SAWs) to induce an acoustic radiation force (ARF) and separate microscale droplets of different types. To thoroughly investigate the effects of ARF on both cylindrical and spherical droplets, we conducted a series of droplet sorting experiments, adjusting the acoustic impedance of the fluid surrounding the droplets, droplet velocity, and SAW amplitude.

Furthermore, to gain a deeper understanding of the underlying mechanism, a new dimensionless number of AR_D was shown, which is defined as the ratio of the acoustic force to the drag force experienced by the droplets in acoustofluidic microchannel. The results were analyzed with theoretical estimation using ray acoustics. The experimental results were compared with theoretical estimations using a ray acoustics model, and a good agreement was observed. Based on these findings, we demonstrated that microscale droplets with the same volume, but different acoustic impedance can be continuously separated by applying an acoustic field, without the need for labels or detection. This work is also extended to achieve droplet sample-encapsulated droplet separation by encapsulating polymer particles of several sizes. Droplets containing particles were noticed to be deflected significantly larger distance compared to empty droplets, as the particle-encapsulated droplet experiences an enhanced magnitude of ARF. Considering the critical importance of precise on-chip separation of multiple droplet types in various microfluidic applications, the proposed acoustofluidic method opens up new possibilities for separation of microscale droplets.

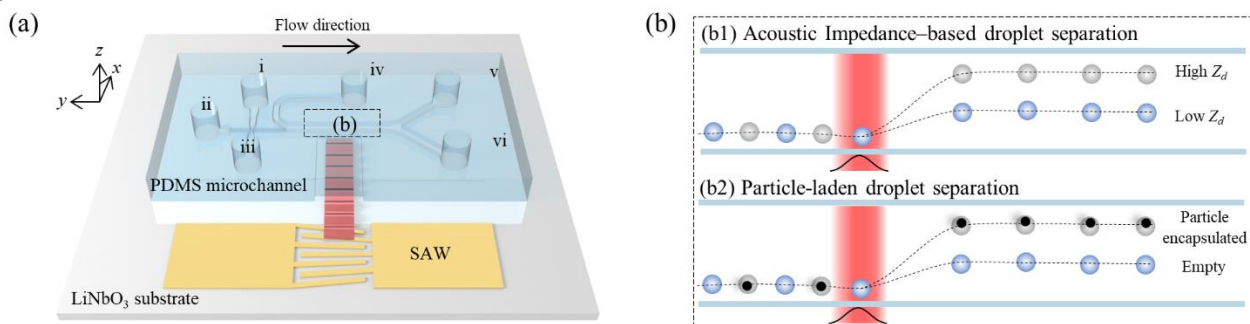


Figure 1: (a) A schematic of an acoustofluidic chip for separation of microscale droplets by surface acoustic wave (SAW)-induced acoustic radiation force (ARF). (b) Acoustic impedance-based and particle laden droplet separation.

Methodology

The proposed device is comprised of three inlets: two dispersed phases and a continuous phase, one sheath fluid flow, and two outlets as shown in Figure 1(a). To optimize the effects of ARF on various droplets of varied acoustic impedances and size, we produced a single kind of droplet utilizing one dispersed phase. In addition, at a double T-junction, alternatively generated two droplets possessing different acoustic impedance as shown in Figure 1(b1). The droplet moving in the oil and exposed to ARF when USAWs produced by the transducer are converted into longitudinal waves (LWs). SAW-induced ARF was modeled by the ray acoustic approach in geometric scattering regime in which droplet sizes are much larger than the acoustic wavelength.

Furthermore, the LWs were assumed to be coaxial and loosely focused in this model, where beam width was significantly higher than the wavelength. Furthermore, when particles are encapsulated in the droplet and subjected to the ARF, they are supposed to experience enhanced magnitude of ARF as compared to empty droplets as shown in Figure 1(b2).

Acoustic impedance-based droplet separation

When sound travels through a medium with a density of ρ and the speed of sound c , acoustic impedance is defined as $Z = \rho \times c$. We hypothesized that droplets possessing different acoustic impedance values would be subjected to a distinct acoustic force modeled by the ray-acoustic approach. For this purpose, we used DI water and OptiPrep™ having acoustic impedance values of 1.50 MRayl and 2.0 MRayl, respectively. Furthermore, the calculated amount of iodixanol is mixed with DI water to make a solution having acoustic impedance values from 1.60 MRayl to 1.90 MRayl.

Utilizing a simple T-junction, we first produced identical-sized droplets ($D_d \sim 105 \mu\text{m}$) possessing different acoustic impedance values ranging from 1.5 MRayl – 2.0 MRayl and performed droplet sorting experiments at various input powers. Second, we produced two same-sized droplets alternately possessing different Z_d values and achieved Z_d -based separation of droplets as shown in Figure 2(a). Two equal sized droplets (droplet A and droplet B) were generated, whose acoustic impedance values are $Z_{d,A} = 2.0$ MRayl and $Z_{d,B} = 1.5$ MRayl, and exposed them to ARF. Without SAW, both droplets travel hydrodynamically to waste outlet. When an acoustic power of $P_e = 1.66$ W was applied, droplet A was literally deflected more along the axial direction of ARF than droplet B; accordingly, their deflection distances were 290.13 and 221.05 μm , respectively.

Particle-laden droplet separation

We then extended our scope of this work to obtain a particle-laden droplet separation mechanism. Figure 2(b) shows the microscopic images of particle-laden droplet separation. In this work we first performed particle sorting experiments utilizing particles with diameters ranging from 6 – 31 μm and checked their behavior as a response of ARF. We noticed that the migration distance of the particles increased as we changed their diameter while maintaining a fixed acoustic power. Subsequently, we introduced these particles into droplets with a D_d of 65 μm and exposed them to SAW-induced ARF. We compared the migration distances of these droplets with those of empty droplets to evaluate the effect of particle encapsulation. Upon applying an acoustic power (P_e) of 2.01 W to the terminals of transducer, a noticeable difference in the literal migration (Δd_R) was observed between the droplets containing particles and the empty droplets, resulting in their distinct separation. The separation of the droplets is a result of the influence of ARF, which is generated by TSAW.

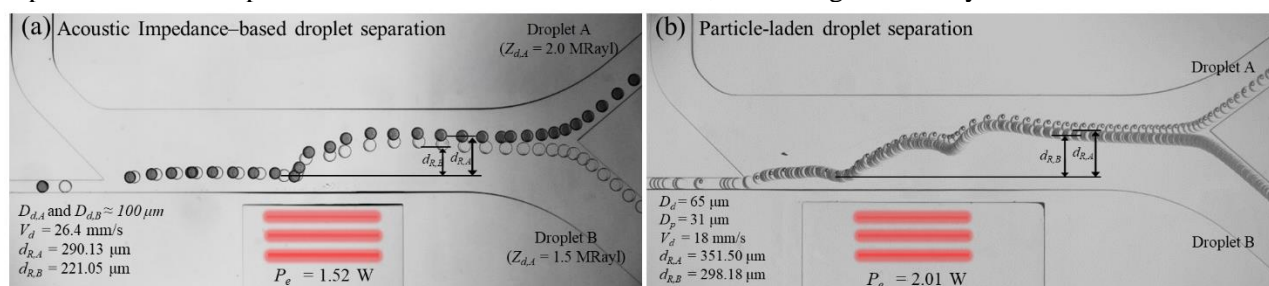


Figure 2: (a) Experimental images of acoustic impedance-based droplet separation. (b) Experimental images of particle encapsulated droplet separation.

Conclusion

We developed an ultrasonic surface acoustic wave (SAW) method for efficiently separating droplets based on their acoustic impedance. This label-free and detection-free technique enables high-throughput droplet separation. We investigated the underlying physics using ray acoustics analysis and introduced a dimensionless number, AR_D , to understand the relationship between ARF and drag force. This acoustofluidic technique is valuable for continuous separation of droplets with different chemical compositions in various microfluidic applications.

Acknowledgments

This work was supported by the National Research Foundation of Korea (NRF) grants funded by the Korea government (MSIT) (Nos. 2020R1A5A8018367 and RS-2023-00210891).

References

Ali M, Park J. Ultrasonic surface acoustic wave-assisted separation of microscale droplets with varying acoustic impedance. *Ultrasonics Sonochemistry*. 2023 Jan 18:106305.

Measurement of acoustic contrast of hematopoietic stem cells by trajectory analysis

Ryan Dubay¹, Jennifer L. Walker¹, Jayanth Dabbi¹, John Manis², and Jason Fiering¹

¹Draper, Cambridge MA, USA

E-mail: jfiering@draper.com URL: <http://www.draper.com>

²Harvard Medical School and Boston Children's Hospital, Boston MA, USA

Introduction

Continuous acoustic separation of peripheral blood cells has potential to improve processing methods for stem cell transplants, cell and gene therapies, and cell collection by apheresis.[1] While acoustofluidic purification of various mature white blood cells from blood products has been well documented, purification of progenitor cells is less studied and detailed quantitative results are lacking. Hematopoietic stem cells (HSCs) are an important target for treating sickle cell disease and for many other therapies in development. In order to predict the potential for label-free acoustic separation of HSCs from other blood cells, we measured the acoustic contrast of pre-purified HSCs by imaging their trajectories as they flowed through a calibrated resonating microchannel (Fig. 1). We compare the results with previously published measurements of lymphocytes, which are expected to be most similar to the HSCs in acoustic manipulations, whereas red blood cells and granulocytes can be largely discriminated by density and monocytes by size.

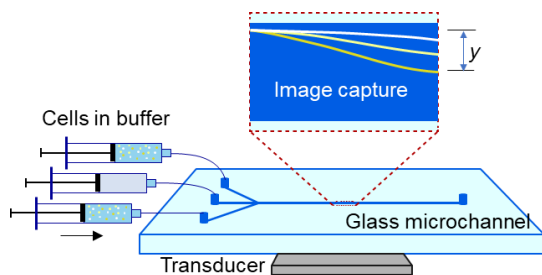


Figure 1: Simplified illustration of apparatus and approach to measuring acoustophoretic displacement of cell in the resonating microchannel with a pressure node along the channel center axis. Dilute cell suspension flows into oscillating microchannel near edges and cells are displaced according to their size and acoustic contrast. The single-cell displacement (y) within a calibrated region is recorded and quantified by comparison with manufactured particles.

Methods

A commercially manufactured glass microchannel (Translume) with three parallel inlets was mounted to a piezoelectric transducer on a temperature controlled stage according to established methods previously described. The channel was $300\mu\text{m}$ wide \times $100\mu\text{m}$ high in cross section and has wide sidewalls not optimized for acoustic efficiency. A repeatable odd mode resonance was empirically located at a driving frequency of 2.34MHz by observing washed red blood cells focusing to the center stream of the channel. Three syringe pumps were set to pump sample in the side inlets at a rate of $6\mu\text{L}/\text{min}$ each while identical buffer flowed at $48\mu\text{L}/\text{min}$. The co-flow consistently positions the inflowing cells at a starting transverse position near the channel sidewall. An upright epifluorescence microscope captured exposures long enough to image flowing cells as discrete streaks across a field of view spanning 1mm of channel length, located at an intermediate position downstream of the inlets but before cells reached terminal transverse position in the center stream.

The captured images supplied a measurement of the transverse displacement of the cells due to acoustophoresis as they traverse the imaged segment of the channel. As has been previously shown, by assuming the one-dimensional approximation for a rectangular microchannel in half-wave resonance, it is possible to extract each cell's acoustic contrast, provided other parameters of the system are known.[2]

We quantified the necessary parameters as follows: 1) The acoustic energy applied to the channel at the given voltage and temperature was determined by similarly measuring the trajectories of fluorescent polystyrene beads, where the particle size, compressibility, and density had been previously recorded. 2) The residence time in the field of view was calculated from the known volumetric flow rate converted to a two-dimensional approximation of the velocity field in the channel. 3) The size distribution of the HSCs from each lot was directly measured by Coulter counter (Beckman), using an aliquot ($\sim 10,000$ cells) from the input sample. Full description of these methods has been recently published for characterization of other cells.[3]

Human HSCs from normal healthy donors were purchased de-identified and cryopreserved (StemExpress). The vendor had isolated the cells by magnetic purification from apheresis collections from donors mobilized with plerixafor and G-CSF to boost HSC abundance in peripheral blood. We measured samples from three donors under identical conditions. The samples were certified $\geq 90\%$ CD34+ by the vendor. On the day of measurement, the cells were thawed and immediately stained with $5\mu\text{M}$ carboxyfluorescein succinimidyl ester fluorescent dye and resuspended in 1X phosphate-buffered saline with 2 mM EDTA to a concentration of $\sim 100,000$ cells/ml. We confirmed viability was $>78\%$. The cell suspensions were pumped through the device in co-flow and at least 100 individual trajectories were captured and analyzed by an automated image processing routine in Python to determine their transverse displacement and hence their acoustophoretic mobility (radius squared \times acoustic contrast factor).

Results

The results of the measurements of the HSC size by Coulter counter and of the HSC acoustophoretic displacement in the imaged field of view are shown in Figure 2 as probability distributions.

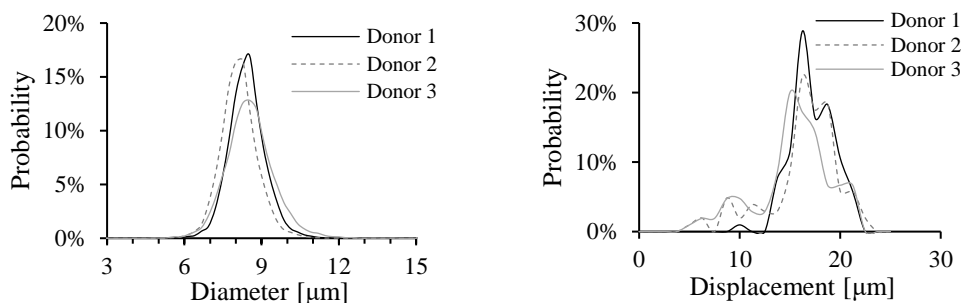


Figure 2: Size distribution (left) measured by Coulter counter and transverse displacement (right) measured in the acoustically actuated microchannel from each of the three donor samples of purified HSCs.

Because the transverse displacement (and acoustophoretic mobility) incorporates both the size of the cells and their acoustic contrast factor, we can scale the displacements by the mean size to obtain an estimate of the latter. This is useful for comparing the response of HSCs to other peripheral blood cells. In particular, lymphocytes are known to have a typical diameter of $7.5\mu\text{m}$ and assumed to have density similar to HSCs, and hence need to be considered in attempting to isolate HSCs by label-free acoustophoresis. Figure 3 compares the acoustophoretic mobility of the HSCs with a measurement of lymphocytes previously obtained.[3] Figure 3 also shows that scaling these results by the measured cell diameters results in an estimate of mean acoustic contrast of HSCs in buffer of 0.043 ± 0.01 , while that of lymphocytes was found to be 0.040 ± 0.01 .

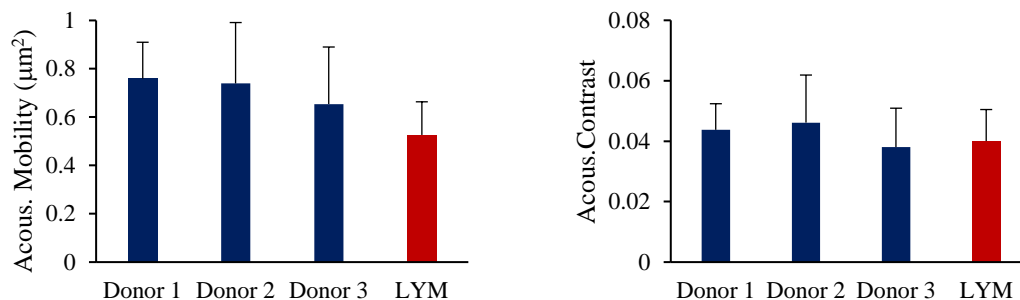


Figure 3: Comparison of acoustophoretic mobility (left) and the derived acoustic contrast factor (right) of the HSCs with that of lymphocytes (LYM) previously published. Both types of cells were suspended in similar buffer.

Conclusion

Estimates of the acoustic contrast of pre-purified HSCs suspended in a conventional buffer were obtained by imaging their trajectories in a glass microchannel excited in approximate half-wave resonance and separately measuring their size. The measurements suggest that mean HSC contrast is close to that of lymphocytes, and therefore purifying them from other cells in blood products will require antibody selection and/or advanced separation techniques. This study did not investigate the contributions of density and compressibility to the acoustic contrast, so measuring these parameters in the future would aid the development of HSC separation.

Acknowledgments This research was supported by NIH NHLBI award 1R21HL145636-01

References

- [1] J. Walker, J. Dabbi, K. Ching, et al., *Cytherapy* **24** (5), S27 (2022).
- [2] R. Barnkob, P Augustsson, T. Laurell, et al., *Lab Chip* **10** (5) 563-570 (2010).
- [3] R. Dubay, E.M. Darling, J. Fiering, *Microsystems Nanoengineering*, accepted for publication (2023).

Capillarity-viscosity-driven travelling waves in superhydrophobicity-supported shallow gas.

Maxime Fauconnier¹, Bhuvaneshwari Karunakaran², Alex Drago Gonzalez¹, William Wong², Robin H. Ras² and Heikki J. Nieminen¹

¹Medical Ultrasonics Laboratory (MEDUSA), Department of Neuroscience and Biomedical Engineering, Aalto University, Espoo, Finland

E-mail: maxime.fauconnier@aalto.fi, [my portfolio](#)

²Soft Matter and Wetting group, Department of Applied Physics, Aalto University, Espoo, Finland

Introduction

Interfacial waves (IW) travelling in deep and shallow water are commonplace, that each and everyone gazing at ocean waves washing ashore could witness. This does not hold for the complementary third configuration, *i.e.*, IW propagating on 'shallow gas', yet can be experimentally approached thanks to soft matter science. The chemical modification of the microstructure of a water-immersed surface allows the trapping within its roughness of a thin gas layer (*i.e.*, air plastron) [1]. This is allowed by the important capillary forces occurring at the three-phase boundaries. Profiting from this superhydrophobic (SHP) feature and using the plastron as a propagation medium for IW generated by nonlinear ultrasound (US), we feature in this work what we believe to be a new type of capillary-like waves with unprecedented features.

Methodology

The surface of a $5 \times 5 \text{ mm}^2$ sample made of polydimethylsiloxane is microstructured (square lattice arrangement of cylindrical micropillars, radius $10 \mu\text{m}$, varying spacing and height in range $15\text{-}65 \mu\text{m}$ and $15\text{-}71 \mu\text{m}$, respectively) by soft- and photo-lithography, then fluorocoated, so that low surface energy and stable SHP are achieved [2]. Immersed in pure (Milli-Q) water, this SHP surface and its plastron are then exposed to an US burst ($f_{ac} = 2.5 \text{ MHz}$, 50 cycles) generated by a focused transducer (focus 0.51 mm by 3.28 mm , acoustic field depicted in figure 1) disposing at its center of an opening allowing light transmission. Thanks to ultra-fast imaging (frame rate = $159 \text{ kHz} \ll f_{ac}$), we report here on the fluidic timescale response of the plastron interface, assessed from the top-view patterns of optical refraction.

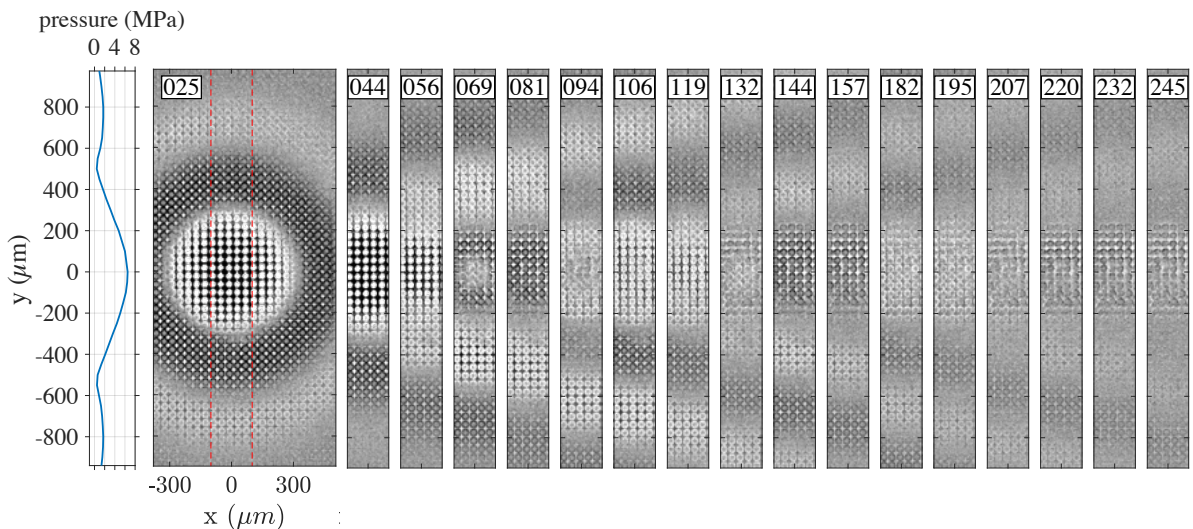


Figure 1: Typical top-view pattern of optical refraction revealing the presence of a radially travelling wave, triggered by the displayed axisymmetric field of acoustic pressure (left). It propagates on the plastron of one of our manufactured superhydrophobic surfaces (pillars height = $25 \mu\text{m}$ and spacing = $25 \mu\text{m}$), immersed in water. The time indices given on the snapshots are in μs unit.

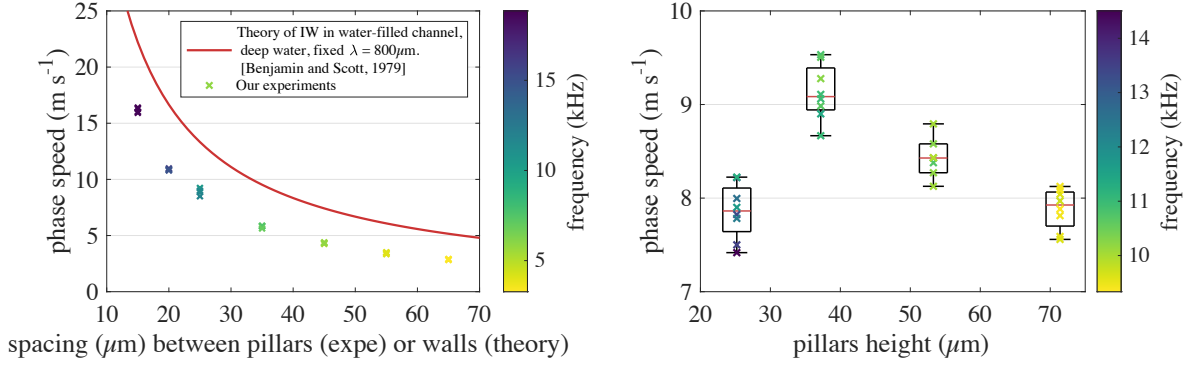


Figure 2: Wave frequency as a function of the phase speed and (a) the pillars spacing ($n=4$, with fixed height = $53 \mu\text{m}$) and (b) the pillars height ($n=8$, with fixed spacing = $25 \mu\text{m}$).

Nonlinear capillary-like waves

An exemplary case of optical refraction pattern resulting from the presence of a wave travelling on a superhydrophobic plastron, or *plastronic wave*, is given in figure 1 on which the time information is in μs unit. Waves are radially propagating away from the location of acoustic focus and important acoustic radiation force (ARF). On snapshots of figure 1, light and dark sections of the light intensity pattern respectively transcribe concave and convex excursions of the plastron interface. Once the US burst is over, the interface undergoes an elastic swing back to its equilibrium state followed by oscillations, under the dictatorship of capillary forces. The tracking of these waves allows to recover their properties (frequency and phase speed), which are then associated to the plastron parameters (i.e., microstructures geometry). In this exemplary of figure 1, the measured phase speed, frequency and wavelength are about $8 \text{ m} \cdot \text{s}^{-1}$, 11.4 kHz and $700 \mu\text{m}$, respectively. According to capillary-gravity waves theory [3], this is approximately 10 times greater than the phase speed of a conventional capillary wave of comparable wavelength.

The tracking of similar waves in a wide range of topography of superhydrophobic surface (defined in Methodology) allowed the mapping of these waves' properties, as shown in figure 2, as a function of the micropillars spacing (a) or height (b). As the pillars spacing (respectively, pillars height) increases and the plastronic air layer becomes less-constrained (respectively, thicker), the phase speed converges towards values that could belong to conventional waves, i.e., in a configuration of constrain-free deep water. Our results from figure 2(a) follow a similar trend as the semi-empirical model developed by Benjamin and Scott [3]. Although the global trend can be described as such, what happens in the case of the $25.2 \mu\text{m}$ high pillars needs further explanation. A significant decrease of the phase speed is observed, as shown in figure 2(b). Just like bottom friction can alter the orbital motion of water particles and slow down a shallow water wave, it is reasonable to hypothesise that similar behaviour would occur for shallow gas waves. Of course, because air is about 50 times less viscous than water (kinematic viscosity $\nu = 1.48 \times 10^{-5} \text{ m}^2 \cdot \text{s}^{-1}$), this bathymetry effect will only happen for waves activity of which the troughs enter the viscous boundary layer $\delta = \sqrt{\nu/\pi f}$ [4] approx. equalling $21 \mu\text{m}$, where the frequency $f = 11.4 \text{ kHz}$. This is very likely to occur for IW travelling on a $25.2 \mu\text{m}$ high plastron, possibly explaining that drop in phase speed.

Conclusion

The meeting of surface engineering and nonlinear acoustics allowed us to experimentally bring to light what we believe to be a new type of interfacial waves travelling on the air-filled plastron of a superhydrophobic surface. Thanks to ultrafast microscopy, their extraordinary fast phase speed and nonlinear dependency on the gas layer thickness and viscous boundary layer could be measured and explained based on the literature on capillary-gravity waves propagating on constrained interfaces and viscosity-driven oscillatory flow.

References

- [1] A. B. D. Cassie, and S. Baxter. Transactions of the Faraday Society **40**, 546-551 (1944).
- [2] W. S. Y. Wong et al.. Langmuir **38**, 6224-6230 (2022).
- [3] G. D. Crapper. Journal of Fluid Mechanics **2**, 532-540 (1957).
- [4] J. S. Bach and H. Bruus. The Journal of the Acoustical Society of America **144**, 766-784 (2018).

Sponsored by

